INVESTIGATION OF METOCEAN INTERACTION BEHAVIOUR MODEL WITH OFFSHORE STRUCTURES NEAR THE FREE SURFACE

MUSHTAQ AHMED

MASTER OF ENGINEERING SCIENCE

FACULTY OF ENGINEERING AND GREEN TECHNOLOGY
UNIVERSITI TUNKU ABDUL RAHMAN
AUGUST 2022

INVESTIGATION OF METOCEAN INTERACTION BEHAVIOUR MODEL WITH OFFSHORE STRUCTURES NEAR FREE SURFACE

By

MUSHTAQ AHMED

A thesis submitted to the Department of Environmental Engineering,
Faculty of Engineering and Green Technology,
Universiti Tunku Abdul Rahman,
in partial fulfilment of the requirements for the degree of
Master of Engineering Science
August 2022

ABSTRACT

INVESTIGATION OF METOCEAN INTERACTION BEHAVIOUR MODEL WITH OFFSHORE STRUCTURES NEAR FREE SURFACE

MUSHTAQ AHMED

The study of metocean interaction around free surface is critical for determining the safety of offshore buildings. Previously, this assessment was done using experimental and analytical techniques, but due to technological advancements, numerical methods are now the most extensively used for assessing the impact of metocean characteristics such as offshore wave and current on fixed and floating offshore installations. In the numerical tank, the numerical models may quickly generate geometries of physical models with realistic offshore settings. Validation and verification of numerical model is frequently required before performing actual model testing. For model testing and fluid-structure interaction modelling, ANSYS Fluent is used to create a two-dimensional rectangular numerical tank. The continuity and Reynolds-Averaged Naiver-Stokes (RANS) equations are governing equations for numerical modelling. In the wave tank, Stokes waves are created. To examine the behaviour of a metocean interaction model near the free surface with offshore structures, three objectives were specified. The first objective of the study was to generate the ocean environments in the numerical tank. The second objective of the study dealt with Fluid-Structure Interaction at two different Reynolds numbers. The last objective involved Wave Structure Interaction (WSI) near the free surface of a fixed offshore platform deck. The

study's first objective is met by building two numerical models having a smooth and curved bottom boundary, respectively. The simulation results of the smooth bottom boundary tank are compared with the theory and the curved bottom boundary tank are compared with the experiment. All the wave equations are Stokes second order waves because they satisfy the Ursell parameter. All of the simulated outcomes' free surface heights closely match the ideal wave altitudes, indicating that the study's initial goal has been met. To achieve the second objective, for two reference values Reynolds number (Re) 3900 and 10000, two turbulence models are utilised. When compared to the experiment, the realisable k epsilon (RKE) turbulence model produced more accurate lift and drag coefficient values. It had a good agreement with the experimental data available, with a discrepancy of less than 10%. To achieve the last objective, the rectangular deck is inserted into the tank after successful model testing to determine the wave-in-deck loads. The results show that when water comes into contact with the deck, the velocity towards the upstream edge becomes negative and changes direction. A constant velocity of 0.3 ms^{-1} is experienced in the tank which increases near the free surface when water moves near the edges of the deck. Lifting forces generated from wave-in-deck loads of current simulations are compared with the experimental results. An error of less than 3% is observed during the maximum lifting force while an error of 15% is observed during the minimum lifting force during this comparison. It is concluded from the study that CFD results agree well with analytical and experimental results.

ACKNOWLEDGEMENT

First of all, I acknowledge my supervisor, Dr. Zafarullah Nizamani, for his persistent encouragement, kind guidance and careful monitoring. He has always been there for my moral, financial and psychological support. I appreciate my co-supervisors, Prof Dr. Nakayama A. and Dr. Montasir Osman, for guiding me in this research. I can never forget Dean of FEGT, Prof. Dr. Yap Vooi Voon whose smiling face has always been keeping my morale high throughout this research. I extend my deepest gratitude to UTAR where I have been provided with an excellent working environment, without any bureaucratic or financial obstacles.

The authors acknowledge the financial support through MOHE/FRGS /1/2018/TK01/UTAR/02/4 provided by Universiti Tunku Abdul Rahman (UTAR), Perak, Malaysia.

APPROVAL SHEET

This thesis entitled **"INVESTIGATION OF METOCEAN INTERACTION BEHAVIOUR MODEL WITH OFFSHORE STRUCTURES NEAR FREE SURFACE"** was prepared by MUSHTAQ AHMED and submitted as partial fulfilment of the requirements for the degree of Master of Engineering Science at Universiti Tunku Abdul Rahman.

Approved by:

_____
(Dr. Zafarullah Nizamani) Date:10/01/2022
Assistant Professor/Supervisor
Department of Environmental Engineering
Faculty of Engineering and Green Technology
Universiti Tunku Abdul Rahman

_____
(Prof. Dr. Nakayama A.) Date:10/01/22
Professor/Co-supervisor
Department of Environmental Engineering
Faculty of Engineering and Green Technology
Universiti Tunku Abdul Rahman

_____
(Dr. Montasir O.) Date:…10/01/2022.
Lecturer
Department of Civil Engineering
Faculty of Engineering
Universiti Technologi Petronas

FACULTY OF ENGINEERING AND GREEN TECHNOLOGY

UNIVERSITI TUNKU ABDUL RAHMAN

Date: 06th January 2022

SUBMISSION OF FINAL YEAR PROJECT /DISSERTATION/THESIS

It is hereby certified that **MUSHTAQ AHMED** (ID No: 19AGM07060) has completed this thesis entitled **"INVESTIGATION OF METOCEAN INTERACTION BEHAVIOUR MODEL WITH OFFSHORE STRUCTURES NEAR FREE SURFACE"** under the supervision of **Dr. Zafarullah Nizamani** (Supervisor), & **Prof. Dr. Akihiko Nakayama** (Co-Supervisor) from the department of Environmental Engineering, Faculty of Engineering and Green Technology at Universiti Tunku Abdul Rahman and **Dr. Montasir Osman** (External Co-Supervisor) from department of Civil and Environmental Engineering, Universiti Tecchnologi Petronas.

I understand that University will upload softcopy of my final year project / dissertation/ thesis* in pdf format into UTAR Institutional Repository, which may be made accessible to UTAR community and public.

Yours truly,

_____

(*Mushtaq Ahmed)*

DECLARATION

I, Mushtaq Ahmed, hereby declare that this dissertation is based on my original work except for citations and quotations which have been duly acknowledged. I also declare that it has not been previously and concurrently submitted for any other degree or award at UTAR or other institutions.

Signature:

Name: Mushtaq Ahmed

Registration No: 19AGM07060

Date: 06.01.2022

DEDICATION

I dedicate this thesis to my family, and friends from UTAR, Malaysia and SAU, Pakistan. Without their intellectual, kind and sincere support, I would never be able to complete this work.

PUBLICATIONS

1. **Mushtaq Ahmed**, Zafarullah Nizamani, Akihiko Nakayama, and Montasir Osman. 2019. "Review of Fluid-structure Interaction Model in a Numerical Wave Tank with Offshore Structures Near the Free Surface". **IS-FMTS** https://doi.org/10.20944/preprints202007.0723.v1 (**Published in Scopus** Indexed Conference)
2. **Mushtaq Ahmed**, Zafarullah Nizamani, Akihiko Nakayama, and Montasir Osman. 2020. "Some Recent Fluid-Structure Interaction Approaches for the Wave Current Behaviour With Offshore Structures". **CFD Letters** 12 (9):15-26. https://doi.org/10.37934/cfdl.12.9.1526 (**Published in Scopus** Indexed Journal)
3. **Mushtaq Ahmed**, Zafarullah Nizamani, Akihiko Nakayama, and Montasir Osman. 2021. "Analysis of loads caused by waves on the deck near the free surface of the offshore platform using Computational Fluid Dynamics". **Ships and Offshore Structures** https://doi.org/10.1080/17445302.2021.1954329 (**Published in WOS SCIE** Indexed Journal, IF=1.977, **Q2**)
4. Zafarullah Nizamani, Lee Li Na, Akihiko Nakayama, Montasir Osman, and **Mushtaq Ahmed.** "Renewable Wave Energy Potential for the Sustainable Offshore Oil Platforms in South China Sea". **IEEE ACCESS** https://doi.org/10.1109/ACCESS.2021.3104729 (**Published in WOS SCIE** Indexed Journal, IF=3.67, **Q1**)
5. **Mushtaq Ahmed**, Akihiko Nakayama, and Montasir Osman. "Generation of Offshore Environments in the Numerical Wave Tank to Model Metocean Conditions Interaction with Offshore Structure Near the Free Surface". **IOP Conference series: Earth & Environmental Science** https://doi.org/10.1088/1755-1315/945/1/012018 (**Published** in **Scopus** indexed conference)
6. **Mushtaq Ahmed**, Akihiko Nakayama, and Montasir Osman. (**Under Review**). "Fluid structure interaction (FSI) analysis around cylindrical structure using computational fluid dynamics (CFD)". **Ocean Modelling** (Submitted **WOS SCIE** Indexed Journal, IF=3.68, **Q1**)
7. Akihiko Nakayama, Zafarullah Nizamani, Yusuke Uchiyama, Montasir Osman and **Mushtaq Ahmed**. (**Under Review**). "Large Eddy Simulation of flow past a realistic offshore structure fixed on seabed" **Fluids and Structures** (Submitted **WOS SCIE** Indexed Journal, IF=2.917, **Q2**)

TABLE OF CONTENTS

ABSTRACT ii
ACKNOWLEDGEMENT v
DECLARATION viii
DEDICATION ix
PUBLICATIONS x
TABLE OF CONTENTS xii
LIST OF TABLES xv
LIST OF FIGURES xvii
DEFINITIONS xxiii
LIST OF SYMBOLS xxiv
LIST OF ABBREVIATIONS xxvi
LIST OF APPENDICES xxvii

1 INTRODUCTION 1
1.1 Overview 1
1.2 Problem Background 2
1.3 Previous work and limitation of existing studies 3
1.4 Problem Motivation 5
1.5 Problem Statement 6
1.6 Problem Description 7
1.7 Aims and Research Objectives 8
1.8 Research Scope 8
1.9 Limitation of Study 9
1.10 Significance of the work 9
1.11 Research Methodology 10
1.12 Assumptions 12
1.13 Summary 13
1.14 Organization of Thesis 13

2 LITERATURE REVIEW 16
2.1 Computational Fluid Dynamics (CFD) 16
2.1.1 Computing Power for CFD 17
2.1.2 Components of CFD 18
2.1.3 Tools for CFD 23
2.2 ANSYS WORKBENCH 24
2.2.1 ANSYS SpaceClaim 25
2.2.2 ANSYS Meshing 26

2.2.3 ANSYS FLUENT 27
2.2.4 ANSYS CFD-Post 29
2.3 Governing Equations 30
2.3.1 Continuity Equation 31
2.3.2 Momentum Equation 32
2.4 Water wave theories 33
2.4.1 Stokes wave theory 35
2.5 Numerical Wave Tank (NWT) 36
2.5.1 Turbulence Modelling 37
2.5.2 Reynold's Averaged Navier Stokes (RANS) Equations: 38
2.5.3 Equation discretisation 45
2.5.4 Spatial discretisation 47
2.5.5 Temporal discretisation 48
2.5.6 Pressure-velocity coupling 49
2.5.7 Boundary Setup 49
2.5.8 Solution Criteria 50
2.5.9 The volume of the Fluid Method (VOF) 50
2.6 Verification and validation of Numerical Wave Tank (NWT) 51
2.7 Fluid-Structure Interaction 54
2.7.1 Flow around a circular cylinder 54
2.7.2 Regime of Flow 56
2.7.3 Vortex Shedding 58
2.7.4 Drag, Lift and Pressure Coefficient 59
2.7.5 Vortex Pattern 61
2.8 Summary 62

3 METHODOLOGY 64
3.1 Operational Framework 64
3.2 Scenario 1: Flow in a rectangular tank 66
3.2.1 Stokes second-order wave 66
3.2.2 Velocity of the Particle 67
3.2.3 Confirmation of the validity of stokes second-order wave 68
3.2.4 Surface elevation of the waves 68
3.2.5 Grid dependency test 69
3.2.6 Wave parameters for simulation 70
3.2.7 Model setup 71
3.3 Scenario 2: Flow over a submerged bar 74
3.3.1 Mesh Generation 74
3.3.2 Production of Boundary Conditions 75
3.3.3 Wave Generation at the inlet Boundary 76
3.3.4 Wave Reflection Prevention at the outlet 77
3.3.5 Other Boundary Conditions 77
3.3.6 Solver Settings 77
3.3.7 Physical Properties 78
3.3.8 Control Properties 79
3.4 Scenario 3: Flow in a tank with circular structure 79
3.4.1 Computational domain and boundary conditions 80
3.4.2 Meshing 81
3.4.3 Simulation settings 82

3.4.4 Grid and time convergence study 83
3.5 Scenario 4: Flow in a tank with rectangular structure 83
3.5.1 Experimental setup 84
3.5.2 Mesh 85
3.5.3 Initial and Boundary Conditions 86
3.5.4 Solver Settings 89
3.6 Summary 91

4 RESULTS AND DISCUSSION 92
4.1 Flow over a rectangular tank 92
4.1.1 Meshing convergence 93
4.1.2 Comparison of ideal wave profile with simulation 95
4.2 Flow over a submerged bar 99
4.2.1 Meshing results 99
4.2.2 Comparison of experimental wave profile with simulations 106
4.3 Flow in a tank with a cylindrical structure 113
4.3.1 Grid convergence results 114
4.3.2 Timestep convergence results 116
4.3.3 Coefficient of drag and lift under turbulence flow 118
4.3.4 Pressure distribution 121
4.4 Flow in a Tank with Deck Structure 123
4.5 Summary 129

5 CONCLUSION AND RECOMMENDATIONS 132
5.1 Conclusion 133
5.2 Recommendations 136

6 REFERENCES 137

7 APPENDICES 147

LIST OF TABLES

Table		Page
2.1	Characteristics of metocean parameters with active regions	34
2.2	Classification of sea water-based on the depth	34
2.3	Most important dimensionless numbers in Fluid Dynamics	54
3.1	Size of mesh elements used in meshing test for a simple flat bottom rectangular wave	69
3.2	Parameters of the wave utilised for validation (scenario 1) and verification (scenario 2) **tank**	70
3.3	Location of wave gauges in the flat bottom rectangular tank used for the validation	71
3.4	Size of mesh elements used in meshing test for submerged bar wave tank	75
3.5	Location of wave gauges in the submerged bar wave tank used for the verification	76
3.6	Physical properties of model	79
3.7	Parameters used in scenario 3	81
3.8	Simulation set-up for flow around circular cylinder recommended by ANSYS Fluent (2013)	82
3.9	Size of mesh elements used in the grid convergence test for flow in a tank with a circular structure	83
3.10	Wave parameters used in the experimental study of Rolf Jarle (2001)	88
4.1	Mesh convergence criteria at two Reynolds number using the RKE model.	115
4.2	Courant number convergence criteria at two Reynolds number using RKE model	115

4.3	Comparison of simulations results for the drag coefficient with available data of experimental study for Re = 3900 & 10000	118
4.4	Comparison of simulations results for lift coefficient with available data of experimental study for Re = 3900 & 10000	119

LIST OF FIGURES

Figure		Page
2.1	Model Pre-Processing (geometry, meshing, and boundary conditions), Processing (computation) and post-processing (visualization of result) are essential components of CFD (Cummings et al., 2015)	19
2.2	Building numerical model is known as geometry with CAD-based Tools: (a) An individual component of the structure (b) Simple tripod structure (c) Complex multi-component jacket structure (Song et al., 2012)	20
2.3	Geometry of the numerical model is divided into smaller segments called cells or control volume where flow equations are solved during the meshing process (Tran and Kim, 2016)	21
2.4	Post-processing generates data in various forms including vector plots, contour plots etc (Cummings et al., 2015)	23
2.5	Different mesh types used in domain discretization (Balendra and Li, 2008)	27
2.6	Working principle of ANSYS FLUENT (A. D. Canonsburg, 2017)	28
2.7	Free surface elevation of stokes first order and second-order wave	36
2.8	Sketch of numerical model with boundaries to generate numerical waves (Lambert, 2012)	37
2.9	The decomposition of turbulent flow with Reynold's decomposition. The velocity decomposed into steady mean ū and fluctuating ύ components (Nagata et al., 2020).	38
2.10	Different flow regimes around the circular cylinder (Nagata et al., 2020)	58

2.11	Relation of Re and St around circular cylindrical structure (Nagata et al., 2020)	59
2.12	Direction of lift and drag force around the circular structure (Yang et al., 2015)	60
2.13	(a) A layout of vortex activity pattern, (b) Vortex wake patterns feature (Anderson et al., 2020)	62
3.1	The geometry of the numerical wave tank to model the flow over a rectangular tank for the comparison of free-surface elevation with ideal wave profiles obtained using Stokes second-order wave	66
3.2	Geometry of simulation setup to model the flow over a tank with submerged bar for the comparison of free-surface elevation with ideal wave profiles obtained by Dingemans, (1994) in his experiments	74
3.3	A partial view of four different grid resolution of mesh generated for the numerical wave tank to model the flow over a tank with submerged bar	75
3.4	Simulation model geometry containing cylindrical structure to model the fluid-structure interaction (FSI) near the free surface for comparison of simulations with experiment	80
3.5	The structure mesh generated around the circular cylinder for modelling fluid-structure interaction	81
3.6	The geometry of the numerical wave tank with the rectangular structure acting as deck for offshore platform to study wave in deck loads near the free surface	84
4.1	Simulation waves generation in a rectangular wave tank using stokes second-order wave theory	93
4.2	Grid dependency test results of gauge 1 located at 2 m on the horizontal x-axis for a rectangular wave tank.	93

4.3	Grid dependency test results of the gauge 2 located at 4 m on the horizontal x-axis for a rectangular wave tank.	94
4.4	Grid dependency test results of the gauge 3 located at 6 m on the horizontal x-axis for a rectangular wave tank.	94
4.5	Grid dependency test results of the gauge 4 located at 8 m on the horizontal x-axis for a rectangular wave tank.	95
4.6	Comparison of simulation results with ideal wave profile for a flow time of 35 seconds.	96
4.7	Comparison of simulation results with ideal wave profile for a flow time of 40 seconds.	97
4.8	Comparison of simulation results with ideal wave profile for a flow time of 45 seconds.	97
4.9	Comparison of simulation results with ideal wave profile for a flow time of 50 seconds.	97
4.10	Comparison of simulation results with ideal wave profile for a flow time of 55 seconds.	98
4.11	Full-scale view of numerical wave tank with submerged bar for comparison of CFD wave profile with the experimental study of Dingemans (1994) .	99
4.12	Grid dependency test results of the gauge 1 located at 2 m on the horizontal x-axis for wave tank with submerged bar.	100
4.13	Grid dependency test results of the gauge 2 located at 4 m on the horizontal x-axis for wave tank with submerged bar.	101
4.14	Grid dependency test results of the gauge 3 located at 5.7 m on the horizontal x-axis for wave tank with submerged bar.	101
4.15	Grid dependency test results of the gauge 4 located at 10.5 m on the horizontal x-axis for wave tank with submerged bar.	102
4.16	Grid dependency test results of the gauge 5 located at 12.5 m on the horizontal x-axis for wave tank with submerged bar.	102
4.17	Grid dependency test results of the gauge 6 located at 13.5 m on the horizontal x-axis for wave tank with submerged bar.	103

4.18	Grid dependency test results of the gauge 7 located at 14.5 m on the horizontal x-axis for wave tank with submerged bar.	103
4.19	Grid dependency test results of the gauge 8 located at 15.7 m on the horizontal x-axis for wave tank with submerged bar.**Error! Reference source not found.**	104
4.20	Grid dependency test results of the gauge 9 located at 17.3 m on the horizontal x-axis for wave tank with submerged bar.	104
4.21	Grid dependency test results of the gauge 10 located at 19 m on the horizontal x-axis for wave tank with submerged bar.	105
4.22	Grid dependency test results of the gauge 11 located at 21 m on the horizontal x-axis for wave tank with submerged bar.	105
4.23	Simulation and experimental data comparison for elevation of the waves at gauge 1.	106
4.24	Simulation and experimental data comparison for elevation of the waves at gauge 2.	106
4.25	Simulation and experimental data comparison for elevation of the waves at gauge 3.	107
4.26	Simulation and experimental data comparison for elevation of the waves at gauge 4.	107
4.27	Simulation and experimental data comparison for elevation of the waves at gauge 5.	108
4.28	Simulation and experimental data comparison for elevation of the waves at gauge 6.	108
4.29	Simulation and experimental data comparison for elevation of the waves at gauge 7.	109
4.30	Simulation and experimental data comparison for elevation of the waves at gauge 8.	109

4.31	Simulation and experimental data comparison for elevation of the waves at gauge 9.	110
4.32	Simulation and experimental data comparison for elevation of the waves at gauge 10.	110
4.33	Simulation and experimental data comparison for elevation of the waves at gauge 11.	111
4.34	Flow around a circular structure in a numerical tank.	114
4.35	Grid convergence test results for value of Drag and lift coefficients at (a) Re= 3900 (b) Re=10000 using RKE model.	115
4.36	Coefficient of Pressure (*Cp*) for different grid resolution at Re=3900 using the RKE model.	116
4.37	Drag and lift coefficients for different courant numbers at (a) Re= 3900 (b) Re=10000 using RKE model.	117
4.38	Comparison of Drag coefficient obtained by two different turbulence models with experiment for Re = 3900 & 10000	119
4.39	Comparison of Lift coefficient obtained by two different turbulence models with experiment for Re = 3900 & 10000	120
4.40	Downstream vortex shedding of the smooth circular structure using RKE turbulence model (a) velocity vector at Re=3900, (b) velocity vector at Re=10000, (c) velocity contour at Re=3900, (d) velocity contour at Re=10000	121
4.41	Comparison of pressure coefficient around a circular cylinder with experiment for RKE turbulence model at Re = 3900	122
4.42	Comparison of pressure coefficient around a circular cylinder with experiment for RKE turbulence model at Re = 10000	122
4.43	The Grid dependency test result for the FSI Tank with four different mesh resolutions.	123

4.44	Offshore wave environments generation in FSI tank using stokes waves.	124
4.45	Four different sketches of the wave profiles below the deck of offshore structure at different time instants observed by (Rolf Jarle, 2001).	125
4.46	Four different sketches of the volume of fluid (VOF) profiles for waves below the deck of offshore structure at different time instants observed in current CFD simulations.	126
4.47	The velocity profile in the FSI tank for a flow time of 42.30 s.	127
4.48	Comparison of Lift forces generated in the FSI tank with the experimental results of (Rolf Jarle, 2001).	128

DEFINITIONS

Governing equations	Equations which describe how the values of unknown variables change when one or more of the known variable changes.
Time step	Incremental change in time for which the governing equations are being solved.
Convergence	An idea that different sequences of transformations come to a conclusion in a finite amount of time and the conclusion reached is independent of the path taken to get it.
Relaxation method	An iterative method for solving a system of equations including non-linear equations.

LIST OF SYMBOLS

λ	Wavelength, m
η	Free surface elevation, m
H	Wave height, m
h	Water depth, m
Hs	Significant wave height, m
H_0	Deep water wave height, m
K	Wave number, radian m^{-1}
L_0	Deep water wavelength, m
t	Time, s
T	Wave period, s
U	Velocity field, (u,v,w)
u	Velocity component of x-axis, ms^{-1}
v	Velocity component of y-axis, ms^{-1}
w	Velocity component of z-axis, ms^{-1}
x	Distance along x-axis, m
y	Vertical distance, m
D	Diameter, m
ρ	Density, kg/m^3
g	Acceleration due to gravity, m/s^2
v	Kinematic viscosity, $kgm^{-1}s^{-1}$
v_t	Eddy viscosity, $kgm^{-1}s^{-1}$
p	Pressure, Pa
ϕ	Level set function

C	Courant number
Cd	Drag coefficient
Cl	Lift coefficient
Cp	Pressure coefficient
Re	Reynolds number

LIST OF ABBREVIATIONS

2D	Two Dimensional
3D	Three Dimensional
CFD	Computational Fluid Dynamics
NWT	Numerical Wave Tank
CPU	Central Processing Unit
DNS	Direct Numerical Simulation
LES	Large Eddy Simulation
RANS	Reynolds Averaged Naiver-Stokes
UDF	User Defined Function
CAD	Computer-Aided Design
PISO	Pressure Implicit Split Operator
SIMPLE	Semi Implicit Method for Pressure linked Equations
SIMPLEC	Semi Implicit Method for Pressure linked Equations-Consistent
SWL	Still Water Level
VOF	Volume of Fluid

LIST OF APPENDICES

Appendix		Page
A	URSELL PARAMETER CALCULATION FOR CASE A	147
B	URSELL PARAMETER CALCULATION FOR CASE B	148
C	URSELL PARAMETER CALCULATION FOR CASE C	149
D	REYNOLDS NUMBER CALCULATION (RE=3900)	150
E	REYNOLDS NUMBER CALCULATION (RE=10000)	151

CHAPTER 1

INTRODUCTION

1.1 Overview

Humans have been searching for fossil fuels on land and in the oceans due to the world's enormous demand for energy. With the advancement of technology, it is now easy to investigate different sustainable energy sources rather than relying on non-renewable ones. The interaction of numerous ocean factors such as wind, waves, and currents in ocean environments complicates flow calculations (Schloen et al., 2017). When structures are added to the water, the flow becomes even more complicated. Different mathematical techniques, observations, and experiments are required for the analysis of such interactions.

Proper modelling of water waves is critical from the engineering perspective of coastal and ocean engineering because they are responsible for more than 70% of all environmental stresses on structures (Abdel Raheem, 2016). Technological advancement has enabled computers to model ocean waves in a numerical wave tank (NWT). Any complicated geometry depicting various ocean features can be accommodated in these numerical wave tanks which are created by developing a numerical code in computers.

Computational fluid dynamics (CFD) is used to overcome this obstacle. It workout flow complications by combining numerical techniques with data algorithms. Numerical modelling on computers is used to simulate fluid interactions with established boundary conditions. For the analysis, the simulation includes preprocessing and data visualisation (Karimirad et al., 2018). Finally, visualisations are aided by post-processing. Flow simulations are performed using a variety of commercial and open-source tools. This research used the commercial ANSYS FLUENT software to model a numerical wave tank.

1.2 Problem Background

All environmental loads exist in offshore environments when structures are erected. The proper design of these structures relies heavily on the estimation of such loads. In such circumstances, the simultaneous occurrence of waves and currents has been recorded, however, the current's loads on the structure are minimal in comparison to the loads caused by ocean waves. Ocean waves are created by wind, while currents are created by a variety of factors such as wave action, tides, density fluctuations, and so on. Waves transfer silt near the beach and cause significant damage to coastal structures and vessels in coastal regions. It causes significant damage to numerous fixed and floating offshore infrastructures in offshore environments.

The advancement of Computational Fluid Dynamics (CFD) has enabled the modelling of the flow's hydrodynamic details. These Navier-Stokes equations-based CFD models may be used to evaluate wave, current,

and their combined flows, which are difficult to analyse under laboratory circumstances. Many researchers ~~looked at using~~ have used CFD to analyse ~~analyses~~ fluid flow (Kim et al., 2016; Zhang, Simons and Buldakov, 2016; Windt et al., 2019; Silva et al., 2016; Singh & Debnath, 2016). The majority of these investigations ~~researches~~ are carried out using numerical wave tank simulations and various CFD solver approaches. Flow dynamics simulation can be done using a variety of open-source and commercial codes. The correctness of such simulations is determined by comparing simulation results with existing experimental results ~~(Zhang et al., 2014)~~ (Zhang et al., 2014).

1.3 Previous work and limitation of existing studies

The precise modelling of water wave behaviour is a crucial topic in offshore engineering. Lower parts of ~~Offshore~~ offshore platforms known as sub-structure ~~superstructures~~ which remain close to water surface are more vulnerable to damages caused by water. A safe distance from the lower part of the deck to the predicted water level known as air-gap is chosen during the design of superstructure of offshore platforms. The forces and loads caused by water may damage the overall deck structure and affect the stability of the platform. The safety margin can be increased by providing a wider airgap. Deck height is the most important factor to determine the stability of platform and keep wider airgap. Water wave modelling by experimental wave tank is a time-consuming process with a limited information of flow phenomenon. Computational modelling can now forecast complicated flow phenomena including ocean waves and structures because of advances in computer processing capacity. Karimirad et al. (2018) conducted a small- scale model

test by using different water conditions to determine the wave forces on vertical walls of slab which are frequently used structures for port protection. The researchers found that forces were sensitive to varying water depth and wave height with limited effect of changing wave period. Schloen et al. (2017) investigated the impact of wave forces by extreme waves on bridges by using a similar scaled model testing study. The impacts of forces caused by extreme water waves can be predicted by model testing, but it is very expensive and time-consuming method. Castellini et al. (2020) conducted similar studies using numerical methods and suggested that CFD is the most ideal method to determine such forces and loads caused by extreme sea states because it is least expensive and less time-consuming tool. He further added that ~~Model~~ model geometries are easier to modify, and environmental conditions can be altered very quickly. The computational method provides detailed information about flow phenomenon because detail of forces and flow can be acquired from any location in the computational domain.

To simulate the hydrodynamics of waves, numerical models commonly use one of two types of equations: Boussinesq type equations or Stokes theory. The inability to replicate wave breaking is one of the most prominent shortcomings of computer models based on Boussinesq equation ~~theory~~. Tatlock et al. (2018) modelled Boussinesq waves by altering only the wave height to account energy dissipation phenomenon, whereas ~~(Vasarmidis et al., 2021)~~ Vasarmidis et al. (2021) made some changes to geometry of computational model to simulate the wave breaking. Some researchers have tried to broaden the applicability of numerical wave tanks based on

Boussinesq theory by establishing hybrid simulation models. Zhang, Zhu & Zou, (2019) designed a Boussinesq equations based model for flow analysis. Using several sets of equations, this model was able to mimic a variety of waves, but it become most complex model for flow analysis. A two-layer method was adopted by both de Ridder et al. (2021) and Liu & Fang (2019) to reduce little bit complexity by solving the Boussinesq model for only two layers of fluid. Numerical models based on stokes wave theory are easier to construct as compared to Boussinesq-type numerical models (Elhanafi et al., 2017; Marques, Gameiro & Ferreira, 2018; Feng & Wu, 2019). Elhanafi et al. (2017) attempted to calculate the inaccuracy created in the tank by the Stokes fifth order wave theory. Cui et al. (2020) and Uddin, Atkinson & Opoku (2020) have successfully implemented Stokes 2nd order wave theory in their numerical simulations and suggested to use it for modelling of wave forces on offshore structures.

1.4 Problem Motivation

Currently, CFD is the most reliable and efficient tool for the proper modelling of ocean environments. This field of ~~Fluid~~ fluid mechanics has grown to its bloom recently after the development of advancement in computational technologies. The commercial CFD solvers are most widely used for describing the most complex turbulent flows perfectly. So many researchers have used commercial ~~Commercial~~ CFD solver FLUENT in their studies (Kim et al., 2016; Zhang, Simons and Buldakov, 2016; Windt et al., 2019; Silva et al., 2016; Singh & Debnath, 2016). The motivation of current study comes from ease of the use of computational techniques in flow modeling. ~~The~~

~~motivation for the present study comes from the exigency need to design a computational model for the generation of ocean waves.~~ The most reliable method for CFD investigations of ocean waves is the use of commercial codes based on RANS equations. These equations are in use for the past 30 years and they are widely accepted in the CFD industry involving fluid flow analysis. ~~RANS equations are most widely used to study flow behaviour for the last 30 years.~~ They involve less computational costs and perfect flow results to predict its nature.

1.5 Problem Statement

Before the invention of computers, studies involving complex waves and offshore structures were performed mainly in the physical wave tanks. After the advancement of technology, these physical wave tanks are being replaced by numerical wave tanks which involve the use of computers. Physical model testing of ocean structures for structural responses is time-consuming and costly. Prediction of loads and forces caused by fluid flow around the structures under ocean environments can be made using (CFD) with the help of numerical techniques. The numerical models are capable of quickly generating geometries of physical models with metocean environments in the numerical tank. To perform the actual model testing, it is often required to validate and verify the numerical wave tank. The fluid analysis involving structures can be performed by using different CFD codes. These CFD programs simulate ocean dynamics and help in solving flow equations. The accuracy of CFD results generated from the simulations mostly rely on the

input parameters used to run these simulations and comparison of CFD results with reference experimental model results.

1.6 Problem Description

The world oceans are now recognized to play a better economical role. The metocean parameters particularly ocean waves play a vital role in the design of ocean structures. For the proper consideration of forces generated from ocean waves, their evaluation is so crucial. There exist studies on the hydrodynamic wave forces but focus on the behaviour of waves near the free surface still seeks attention.

The precise modelling of water wave behaviour is a crucial topic in offshore engineering. Computational modelling can now forecast complicated flow phenomena including ocean waves and structures because of advances in computer processing capacity. CFD solvers are used to model various flow conditions with or without offshore structures in a numerical wave tank. ~~In a numerical wave tank (NWT), this computational modelling is done by computational fluid dynamics (CFD) solvers.~~ These wave tanks can generate surface gravity waves along with complex model geometries.

The quality of simulation results is largely determined by the CFD flow analysis problem's pre-processing component. This first phase determines all of the parameters required for flow analysis. Geometry is a flow analysis domain with well-defined bounds that is generated during pre-processing. When it comes to establishing the limitations of numerical analysis, the model's geometry is crucial. Once the physics of the problem has been

described, a two-dimensional or three-dimensional model can be developed for problem analysis. Meshing should be done with extreme caution and attention to perform an error-free analysis.

1.7 Aims and Research Objectives

The primary aim of this study is to investigate the feasibility of commercial CFD solver for wave generation and fluid-structure interaction near the free surface. Three objectives are set to achieve the research aim:

- To generate regular waves by verifying and validating the numerical model results against the analytical results.

- To determine the lift and drag coefficients around a circular cylinder for fluid-structure interaction.

- To determine wave in deck forces near the free surface of an offshore structure.

1.8 Research Scope

The scope of this project involves the development of a fluid-structure interaction model near the free surface. A commercial CFD code ANSYS FLUENT is used to simulate the possible behaviour of fluid-structure interaction. The work is performed in three stages. The first stage involves the development of a two-dimensional rectangular wave tank for the validation of a numerical model where CFD waves are compared with ideal waves obtained

using stokes second-order wave theory. In the second stage, a submerged bar is introduced in the tank and generated surface elevation of the numerical waves are compared with experiments for the verification purpose. The third and final stage involves fluid-structure interaction where a two-dimensional structure is introduced in the tank.

1.9 Limitation of Study

Following are the limitations of this study.

1. ~~This study is carried out in commercial CFD software.~~
2. ~~Only the study of wave is the main point of focus.~~
3. The simulation is performed for intermediate water depths only so shallow and ultra-deep-water regions are excluded.
4. The fully developed regular wave is considered.
5. Due to limited computing power, the main focus of the study is a simple non-breaking wave case scenario.
6. Validation and verification of CFD result is carried out from experimental data already available.
7. The fluids are treated as incompressible (air is excluded).
8. The elastic responses of the structure (Hydro-elasticity) are ignored

1.10 Significance of the work

The offshore engineering experienced rapid development due to the large benefits associated with the offshore petroleum industry. More than 10,000 units of offshore platforms are installed throughout the oceans of the world.

Initially, most of the units were installed in the shallow water. The fossil fuel resources are declining day by day in shallow water due to their exceeding rates of extraction. ~~The offshore platforms associated with petroleum products were designed conservatively.~~

Malaysia has oil reserves of more than 4 billion barrels most of which lie in the offshore regions. The continental shelf of Malaysia is Sabah, Sarawak and Peninsular Malaysia. Due to advancements in technology and oil reserves depletion, the country is exploring the deep ocean.

The modelling of ocean waves loads for the most efficient design of offshore structures is one of the most challenging hurdles for engineers working in Malaysia. Many local studies exist on effective load determinations of waves on the offshore structures, but they are based on experimental work. The wave flume based on a laboratory scale is too difficult to manage because of some common limitations like cost, space and measurements. The best solution to this problem is the use of computational techniques for fluid hydrodynamics. ~~The CFD studies involving waves have been done extensively in the other parts of the world but for this country, the studies are very rare.~~

1.11 Research Methodology

The research work can be divided into the following six phases:

Phase I: Design four different numerical tanks with a CAD-based tool (Design modeller). Geometry file is within the ANSYS Fluent main file. The ANSYS Files can be accessed on the following link: https://drive.google.com/drive/folders/1r_pEZdkHoNm9xec8lpjIGkgT5b5nykht?usp=sharing

Phase II: Construct mesh of the numerical tanks with ANSYS Meshing Tools (ANSYS Mesh). Mesh file is within the ANSYS Fluent main file. The ANSYS Files can be accessed on the following link: https://drive.google.com/drive/folders/1r_pEZdkHoNm9xec8lpjIGkgT5b5nykht?usp=sharing

Phase III: Run simulations for the flat bottom and submerged bar rectangular numerical tank to validate and verify the model. The ANSYS Files can be accessed on the following link: https://drive.google.com/drive/folders/1r_pEZdkHoNm9xec8lpjIGkgT5b5nykht?usp=sharing

Phase IV: Run Simulations for flow around a circular structure to study the fluid-structure interaction. The ANSYS Files can be accessed on the following link: https://drive.google.com/drive/folders/1r_pEZdkHoNm9xec8lpjIGkgT5b5nykht?usp=sharing

Phase V: Run Simulations for wave in deck forces on fixed offshore deck platform to study wave structure interaction. The ANSYS Files can be accessed on the following link: https://drive.google.com/drive/folders/1r_pEZdkHoNm9xec8lpjIGkgT5b5nykht?usp=sharing

Phase VI: Compare the simulation results with the reference experimental work available in the literature. The Excel files can be accessed on the following link https://1drv.ms/u/s!AhtVpyrOO7Y6jwb6CxIJMhqfsHEP?e=n7CJPi

1.12 Assumptions

Fluid flow analysis is carried out in computational fluid dynamics (CFD) instead of using physical wave tank because it utilizes calculations ranging from simple to complex physics. CFD provide more detail of fluid flow analysis and give results in greater detail which causes a resource-intensive environment by using additional computer power with slow processing time. Due to limited available computational resources, a simplified two-dimensional numerical modelling is adopted in this research. As dimensions of the numerical model do not affect the results so this model is assumed to be a numerical wave tank (NWT) instead of a numerical wave channel (Kyte, 2014). The magnitude of the units have no impact on the simulation results and because of this, the model dimension is kept as the actual one (Ong, 2017). All the scenarios utilizes regular unidirectional and non-breaking ocean waves only. A simple cylindrical structure is used to study the impacts of ocean waves in numerical modelling. All the numerical scenarios modelled in this study are validated and verified from authorized reference experimental work available in the literature.

1.13 Summary

In this chapter, numerical analysis of fluid flow around offshore structures near the free surface to model metocean interaction behaviour is discussed. The importance of generating actual offshore conditions in the numerical wave tank to properly determine the impacts of loads generated by metocean parameters is highlighted. Load analyses play a vital role in the sound and safe design of offshore structures. Section 4.3 and 4.4 involve analysis of loads and forces on structures. Furthermore, the use of computers in the field of fluid dynamics has enabled researchers to carry out cost-free and effective flow analysis by using computational fluid dynamics (CFD). Problem Statement identified the importance of this current study. Aims and objectives elaborate the focus of the study and acknowledge the significance of the current research. All the assumptions used in thesis are correctly mentioned in brief account.

1.14 Organization of Thesis

The whole thesis is distributed into 5 chapters. The title of the first chapter is "Introduction". The second chapter is the "Literature Review". The third chapter involves the "Methodology" of the research work. The fourth chapter accounts "Result and Discussion" of the research. The last chapter of the thesis is chapter number five with the title "Conclusion and Recommendations". Each chapter starts with a brief introductory note to discuss the systematic topics of the chapter and ends with a precise summary

of the whole chapter indicating the overall importance and conclusion of the chapter.

The first chapter introduces the research background for the current topic. It also contains the statement of the problem, the aim of research and the goals of the study to solve such problems. This chapter also deals with the scope of the research and its limitations observed during the course of the research.

The second chapter gives a review of computational fluid dynamics (CFD), its history, components and system requirements. The concept of numerical wave tank (NWT) with the generation of offshore environments are also discussed. Most common wave theories along with fluid-structure interaction (FSI) are reviewed in great detail. The phenomenon of the interaction of breaking and non-breaking waves with offshore structures near the free surface along with simulations of these waves with the help of CFD are also highlighted. Lastly, load predictions, the concept of fluid loadings, load calculations, load trends and CFD result validations are reported concisely.

Chapter 3 highlights a computational fluid dynamic tool named ANSYS FLUENT used in the study for the simulation of a metocean interaction behaviour model with offshore structure near the free surface. Moreover, the geometry of the numerical model with fixed offshore structure is also outlined and discussed. Additionally, the structured mesh is constructed

for the model with mesh refinement for the most important portions of the geometry. Later, multiphase modelling is used to model the offshore environments in the numerical wave tank. Finally, validation of the simulation model is discussed for the offshore environments developed in the CFD wave basin.

Chapter 4 comprises the discussion on results accompanied by critical discussion. All the proposed objectives of the study including development of a numerical model for the generation of waves in a numerical basin, validation of the wave tank by comparing free surface profiles of the waves with ideal waves, verification of the free surface elevation of the CFD waves with referenced experimental work and fluid-structure interaction evaluation are achieved in this chapter. The generated CFD results are ideal when compared with theory and experiments which reveal the fact that CFD can be used for more complex cases like offshore Jacket platforms with individual elements.

Chapter 5 provides a summary of the conclusion from this research and gives a list of recommendations to improve future studies based on this current work.

CHAPTER 2

LITERATURE REVIEW

This chapter provides a review of the generation of waves in oceans and numerical wave tanks along with fluid-structure interaction. Initially, Computational fluid dynamics (CFD), its history, components, and system requirements along with the concept of numerical wave tank (NWT) with the generation of metocean conditions are discussed. The generation and classification of random waves in natural environments are also discussed. The representation of waves based on wave theories is presented. Finally, the flow around structures for fluid-structure interaction (FSI) is mentioned.

2.1 Computational Fluid Dynamics (CFD)

Computational fluid dynamics (CFD) is the study of fluid flow utilising applied mathematics, physics, and computer software. It is a branch of fluid mechanics that analyses and solves fluid flow issues using data structures and numerical methods (Castellini et al., 2020). The central processing units (CPU) of computers solve all flow equation calculations with the help of CFD applications known as CFD solvers. Depending on the type of CFD solver and computing capability, these flow equations might be two-dimensional or three-dimensional (Olabarrieta et al., 2010). High power computers (HPC) can handle complex flow issues in a relatively short amount of time.

The Navier-Stokes equations for fluid flow modelling underpin the entire notion of Computational Fluid Dynamics (CFD). These flow modelling

equations have been in use since the 1930s, long before computers were invented (Tu et al., 2018). Due to a shortage of computing power over 30 years, engineers and scientists simplified the equations for two-dimensional instances. In 1957, a team at Los Alamos National Lab created the first computer based CFD simulation model (Anderson et al., 2020). By 1967, engineers had created a three-dimensional CFD model. Engineers were able to add transonic Euler equations into CFD codes by 1981. This quick growth of CFD is linked to NASA and Boing's interest in flow analysis (Silva, 2018). The low-cost analysis of fluid flow prompted other businesses, such as General Motors and Ford, to adopt CFD for their model analysis. Computing power has become increasingly affordable as technology has advanced. By the 2000s, CFD had become a widely used tool for everyone, including students. On personal computers, there is a wide range of commercial and open-source CFD software that can model complex flow dynamics (Cummings et al., 2015).

2.1.1 Computing Power for CFD

The power of computers is used in computational fluid dynamics. Due to their tremendous computational capability, high-performance computers are more expensive yet take less time to execute calculations (Mader et al., 2020). Reynolds Averaged Navier-Stokes equations widely known as RANS method utilizes less computer power as compared to Large Eddy Simulation (LES) method which is most widely used for Turbulent Flow conditions. The RANS method can be used for laminar as well as for turbulent flow conditions. ~~Less computer power is required for simple flow phenomena such as laminar flow~~

~~with Reynolds Averaged Navier-Stokes (RANS) equations.~~ For steady flow or the RANS approach with more than 1 million cells, a workstation may be necessary (A. D. Canonsburg, 2017). Multiple workstations with a huge amount of storage will be required in cases of high complexity, such as Large Eddy Simulation (LES). For detailed flow analysis of very complex flow problems using Direct Numerical Simulation (DNS), a supercomputer may be needed to run the CFD simulation (T. D. Canonsburg, 2017).

2.1.2 **Components of CFD**

Pre-processing, processing, and post-processing are all steps in the CFD analysis of fluid flow. The geometry, meshing, and boundary conditions of the model are all crucial parts of pre-processing, as shown in Figure 2.1. The pre- and post-processing parts of flow analysis are computationally light, but fluid flow processing is the most computationally demanding aspect of CFD simulations (Cummings et al., 2015). Flow equations are computed on every tiny volume/cell of the computational domain during this processing time, which consumes memory and necessitates the use of powerful computer hardware.

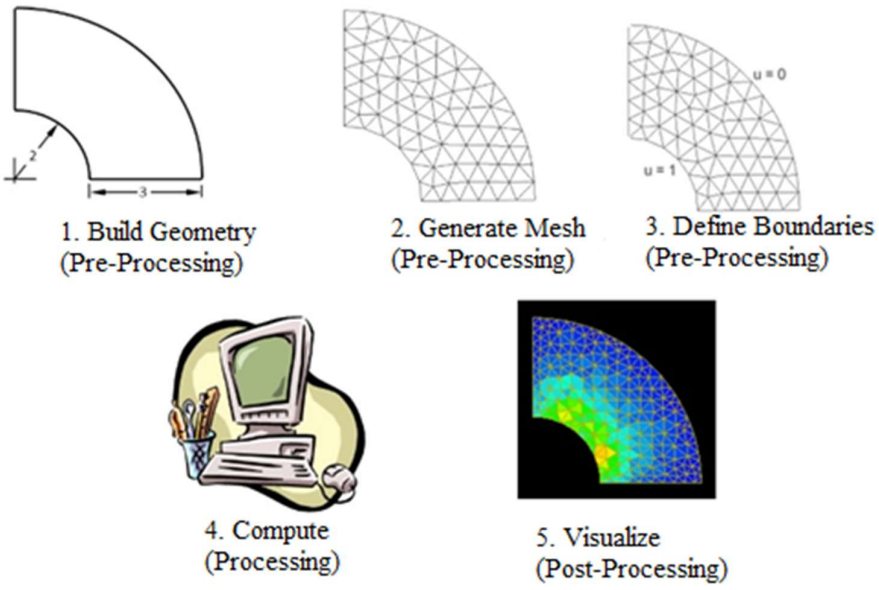

Figure 2.1: Model Pre-Processing (geometry, meshing, and boundary conditions), Processing (computation) and post-processing (visualization of result) are essential components of CFD (Cummings et al., 2015)

2.1.2.1 **Pre-processing**

The quality of simulation results is largely determined by the CFD flow analysis problem's pre-processing component. This first phase determines all of the parameters required for flow analysis. Geometry is a flow analysis domain with well-defined bounds that is generated during pre-processing. This flow domain or geometry is then subdivided into tiny cells called meshes, which is where flow computation takes place. The solver is built up to solve flow equations specific to the problem once the domain is partitioned into discrete segments (Tunlid and Olsson, 2015).

2.1.2.1.1 Geometry

When it comes to establishing the limitations of numerical analysis, the model's geometry is crucial. Once the physics of the problem has been described, a two-dimensional or three-dimensional model can be developed for problem analysis, as shown in Figure 2.2. For three-dimensional geometry models, CAD-based software such as AutoCAD, Solidworks, CATIA, or SpaceClaim is optimal, however, Design Modeler and GAMBIT are the best options for two-dimensional models in case of less processing capability (Tu et al., 2018).

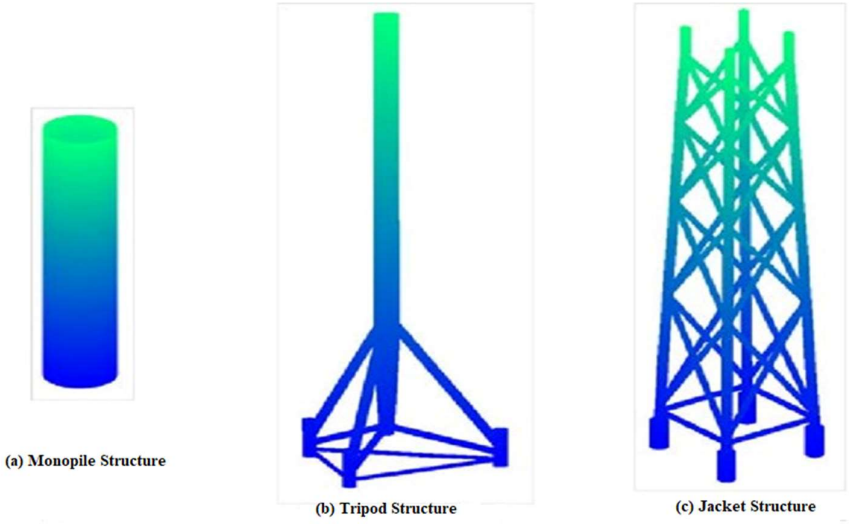

Figure 2.2: Building numerical model is known as geometry with CAD-based Tools: (a) An individual component of the structure (b) Simple tripod structure (c) Complex multi-component jacket structure (Song et al., 2012)

2.1.2.1.2 Meshing

The division of geometry into smaller segments for the solution of flow equations is called meshing as shown in Figure 2.3. Meshing is the most care

requiring step during whole CFD simulation because 90% accuracy of result rely on it (Lintermann, 2021). Meshing should be done with extreme caution and attention to perform an error-free analysis. Sharma et al. (2021) suggest smaller segments, also known as cells or control volumes of geometry, should be refined to the point where all flow analysis information is easily accessible. These cells should be kept as small as feasible to ensure accuracy.

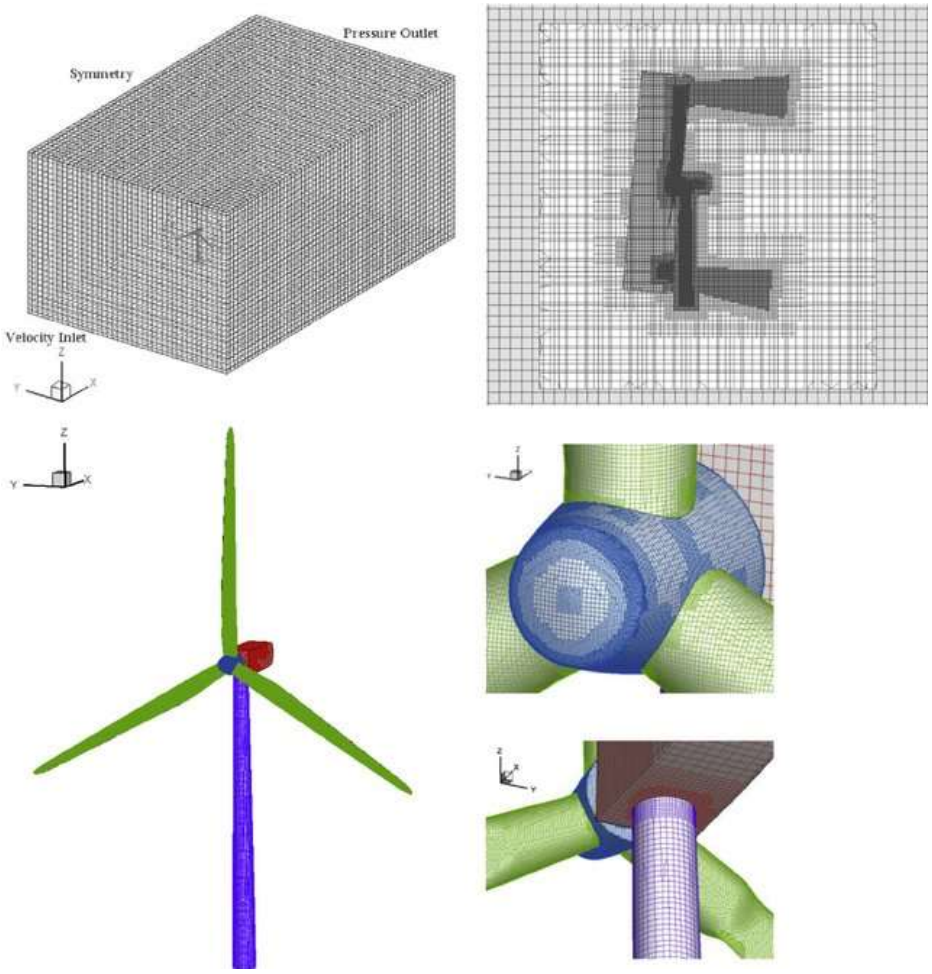

Figure 2.3: Geometry of the numerical model is divided into smaller segments called cells or control volume where flow equations are solved during the meshing process (Tran and Kim, 2016)

2.1.2.1.3 Solver setup

The conditions of the flow analysis issue are defined specifically to the requirements such as transient, one phase, or multiphase in the solver configuration. During this stage of flow analysis, boundary conditions and the fluid type turbulence model are also set. To obtain solution convergence, the user must be familiar with solvers and methodologies. CFD solvers are used to transform the laws of fluid flow in equations where they are solved by numerical methodologies.

2.1.2.2 **Processing**

~~Processing is the one aspect of CFD over which the user has no control.~~ ~~This simulation procedure is similar to a well-defined set of software developers' instructions.~~ Calculations of flow equations are performed on each cell at this stage. This is the step in flow problem analysis that uses the most memory and processing power.

2.1.2.3 **Post-processing**

Post-processing is the analysis of obtained results in terms of available methods like vector plots, contour plots, data curves, streamlines and many more as shown in Figure 2.4. ~~This is similar to a graphical illustration of a flow issue~~. Tecplot 360, FieldView, ANSYS CFD-POST, paraview, and insight are some of the most well-known post-processing applications (Tu et al., 2018). These tools come in handy for calculating derived values and parameters. They display the results based on the user's preferences. They can

perform systematic data analysis and provide extra functionality such as simulation debugging, verification, and validation.

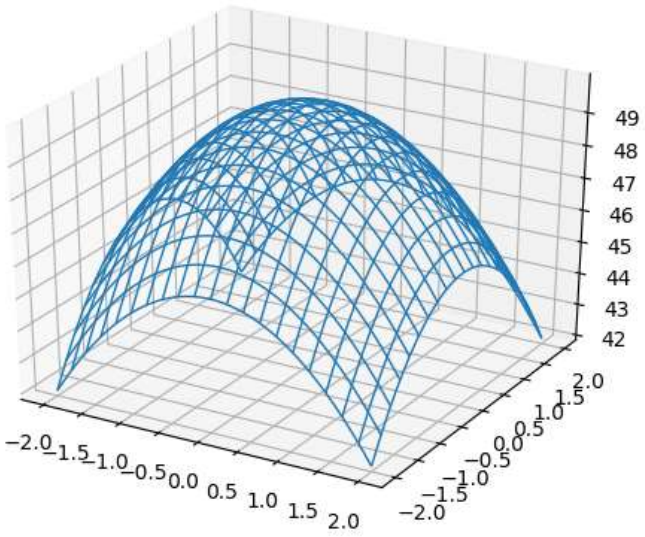

Figure 2.4: Post-processing generates data in various forms including vector plots, contour plots etc (Cummings et al., 2015)

2.1.3 **Tools for CFD**

The following two approaches are practised

1. Writing own CFD codes in a programming language like MATLAB, FORTRAN etc.
2. Using commercial CFD software like ANSYS FLUENT, CFX, OpenFOAM, COMSOL etc.

There are a variety of commercial scripts available that combine all of the capabilities into a single graphical user interface. The workbench by ANSYS integration is the most accurate and widely used tool (T. D. Canonsburg, 2017). Workbench is a graphical user interface offering all the software from a single computer window. ANSYS WORKBENCH provides access to the

preprocessor, solver, and postprocessor tools. ~~The commercial code of ANSYS Inc. was used in this study.~~

2.2 ANSYS WORKBENCH

ANSYS Workbench is a new and innovative product developed by the ANSYS Community. It functions as a user-friendly toolbox that improves simulation productivity by centralising all of the features. It also improves computing speed and reduces the time spent switching between tools, such as geometry management, meshing, and post-processing. The simulation processes are bound together by the workbench environment, which also incorporates numerous application components. For multi-physics simulations, this flawless integration among the components of multiple applications delivers the greatest results. Instead of displaying a list of applications, the schematic window displays an interactive, clear flow chart that depicts all of the project's procedures. This application uses a drag-and-drop user interface, which is the most user-friendly interface available. Each step's progress is shown in the project window, with error-free stages indicated with a green checkmark and uncompleted steps marked with a red cross. The framework, which is capable of the most complicated analysis by integrating different systems, passes files and data from one application to the next. When a user drags and drops a new system into an existing one, all the connections are made immediately with data transfer. The application can track data change patterns, so if the value of the upstream cell changes, the system automatically updates the downstream cell values. This update mechanism saves users the time and effort of manually updating cell values. The ANSYS Workbench is a

new project concept developed by the ANSYS Team, and it is the most user-friendly simulation framework available. It not only facilitates the professional analyst's work but also instils confidence in new users who would otherwise encounter greater challenges.

2.2.1 **ANSYS SpaceClaim**

SpaceClaim is a CAD-like 2D and 3D design tool that is used to generate the model's geometry. In ANSYS Workbench, this is the default geometry tool. In addition to SpaceClaim, a design modeller is employed to generate geometry. Feature simplification, spot weld, split surfaces, extraction of surface model and planner body, modelling of the beam, filling operation, object enclosure, and other operations are among the most typical operations done by this programme. The design in SpaceClaim can be switched between three modes: sketch, section, and 3D. Feature simplification, spot weld, split surfaces, extraction of surface model and planner body, modelling of the beam, filling operation, object enclosure, and other operations are among the most typical operations done by this programme. The pull tool may extrude, revolve, sweep, and draught the faces or round the edge, whereas the move tool moves the faces, surfaces, or components of the solids. The combined tool combines solids and surfaces. If necessary, it can also be split. Section mode is used to develop and edit the designs.

2.2.2 **ANSYS Meshing**

The purpose of meshing in the ANSYS workbench is to create a reliable, user-friendly meshing tool that will make the mesh creation process easier. The most essential stage in CFD simulations that affects the results is meshing. The mesh's goal is to partition the geometry into several elements/volumes so that calculations can be conducted on individual elements/volumes rather than the domain as a whole. Meshing is responsible for the most significant aspects of the solution, such as accuracy, convergence, and speed. The ANSYS community's meshing tool is simple to use and generates the mesh automatically. This application's mesh is simple to create and can be produced even on the first try. These meshes are quite adaptable, ranging from pure hex to elaborate hybrids. This meshing tool's default mesh is a tetrahedron in nature and is relatively simple to construct.

The ANSYS community's meshing tool is the most user-friendly, allowing the user to undertake advanced analysis with very little training. The created mesh primarily focuses on the region of interest, which the user can tweak and evenly space. Figure 2.5 depicts the most prevalent mesh types. Quad cells for 2D domains and hex cells for 3D domains are the suggested mesh types for free-surface flow. It should be tetra or hexahedron in the case of solid bodies. Because the best simulation results come from a consistent mesh, the user should change the default mesh settings in the ANSYS Meshing tool. The ANSYS community recommends the pressure interpolation scheme, often known as pressure discretization. Only quad and hex type cells

are compatible with this design. For Tri or Tetra cell types, the body force weighted technique is employed.

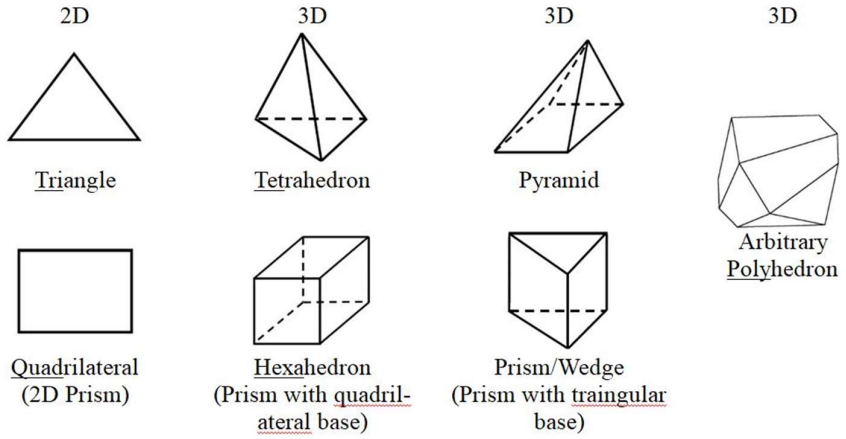

Figure 2.5: Different mesh types used in domain discretization (Balendra and Li, 2008)

2.2.3 **ANSYS FLUENT**

ANSYS Fluent from ANSYS Incorporation was used in this investigation as the CFD software. It's the industry's most popular general-purpose CFD solver. It also employs a computational technique known as the finite volume method to solve the governing equations for fluid flow. Turbulence, chemical reactions, non-Newtonian flows, and deforming barriers are only some of the physics that can be included in ANSYS Fluent. Figure 2.6 depicts the fluent software's functioning principle.

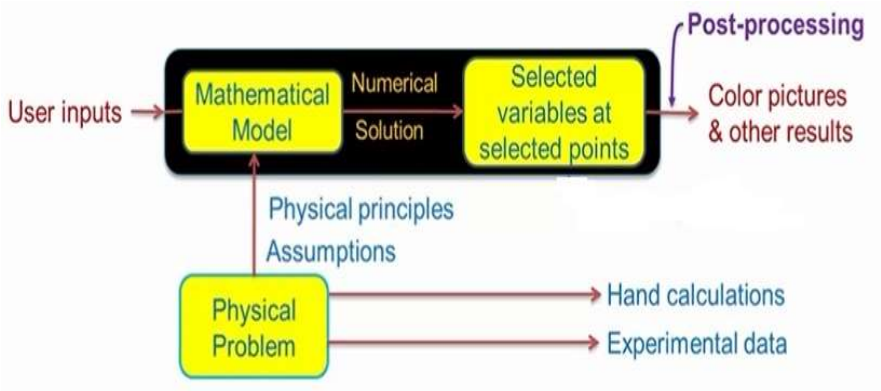

Figure 2.6: Working principle of ANSYS FLUENT (A. D. Canonsburg, 2017)

The governing equations and boundary conditions make up a mathematical model. Boundary value problems are characterised by governing equations and boundary conditions, with governing equations defining the domain and boundary conditions defining the domain's borders. Physical principles and assumptions are the most significant factors for the code in computational fluid dynamics (CFD) governing equations. Selected variables at certain points are calculated using the numerical solution. Verification and validation of the model are part of post-processing. The results of the model are compared to those of the experiments. Model verification gives a sense of whether a model solution is ~~was~~ done successfully or not. If that's the case, are the outcomes in line with the mathematical model? If all went well, the numerical results are ~~were~~ examined, and in the case of acceptance, the simulation results are ~~were~~ compared to the manual calculations and experimental data. Model validation is the last step in the process. The model validation determines whether or not the correct model has been solved.

2.2.4 **ANSYS CFD-Post**

CFD-Post is ANSYS Workbench's default post-processing tool for extensive study of simulation data. In terms of analysis and visualisation, the results supplied by this application are really useful. This programme can provide any desired detail of the flow analysis in the form of statistics, graphs, images, videos, and reports. Flow animations can be represented using a variety of vector plots and streamlines. The transmission of simulation results relies heavily on high-quality images. CFD-user-friendly Post's functionality allows users to acquire simulation data from their computations more quickly and efficiently. It provides statistics on fluid flow for forces, pressure, mass flow, weighted averages, and a variety of other factors. It makes charts, tables, pictures, and a variety of other functions automatically, with virtually no post-processing restrictions. Because it allows users to import numerous datasets of solutions at the same time, CFFD-Post allows users to compare qualitative and quantitative results between two or more data sets. The disparities between the outcome data sets are easily discernible.

CFD-Post includes a 3D picture viewer for 3D images written in high-quality image format, which can be difficult to see with 2D standard image readers in some instances. This application generates high-quality photos that are easy to incorporate in many apps such as MS Office, PowerPoint, and others. Every CFD-Post session can generate reports that users can personalise by adding their logos or adding user-defined content. This programme generates extremely dynamic reports. They can update themselves automatically if new data sets are added. Reports can be exported in a variety

of file formats, including PDF, HTML, and pictures. The animations created by this software can be saved in MPEG-4 format, which is a high-quality file. CFD-findings Post's leave a lasting impact thanks to its graphical features and rendering possibilities.

2.3 Governing Equations

The governing equations are crucial in CFD because, without them, the simulation would be incomplete. Continuity and Navier-Stokes equations are other names for the governing equations. Claude Navier, a French engineer, and George Stokes, an Irish mathematician, are credited with discovering these well-known equations. Except for a few examples like Poiseuille flow, Couette flow, and Stokes flow under particular assumptions, the exact solutions to these equations are still unknown, even though they are 150 years old. Various scientists and engineers have spent their entire lives trying to figure out how to solve these equations precisely for a specific set of geometry. These equations are based on the well-known assumption that fluid particle deformation is caused by shear stress. Laws of motion and conservation were used to create the equations.

The fundamental laws of fluid flow are used to create governing equations. The conservation of mass is the first fundamental law. The conservation of momentum is the second fundamental law. The conservation of energy is the third fundamental law. There is no need to analyse the equation of energy for incompressible fluids like water when density is set to be a fixed value (non-varying). Differential form and Integral form are two

distinct ways to write the governing equation. Both forms are interchangeable and complementing. Both forms are required for CFD users. The fundamental laws of mass and momentum conservation are applied to an infinitesimal fluid particle in differential form. In the integral form, on the other hand, we use a finite volume in the flow domain to apply the fundamental laws of mass and momentum conservation.

When the flow in any open channel is examined with inlet and output boundaries, a finite volume is defined. The ~~Net~~ net mass entering the channel from the inlet and accumulating inside the channel should be equal to the mass leaving the outlet for such a channel. We can apply any arbitrarily shaped control volume within the flow domain in integral form. The exact solution to the governing equation can satisfy the governing equation's differential and integral forms.

2.3.1 **Continuity Equation**

The continuity equation is the confirmation of the mass of any matter entering a system must be equal to the same amount of mass leaving the system in any steady-state process. It is the most basic concept of fluid dynamics where flow is assumed to be an infinitesimally small collection of fluid particles. The continuity equation can be written in the differential way as Eq. (2.1).

$$\frac{\partial \rho}{\partial t} + div\ (\rho \mathbf{V}) = 0 \tag{2.1}$$

Here, velocity vector is represented by **V** of the water particle in *u*, *v* and *w* direction, density is expressed by ρ and time is represented by *t*. Density is constant for incompressible fluids like water which means the change in density with respect to time is zero so the continuity equation can be rewritten as Eq. (2.2).

$$\frac{\partial u}{\partial x} + \frac{\partial v}{\partial y} + \frac{\partial w}{\partial z} = 0 \tag{2.2}$$

2.3.2 **Momentum Equation**

When a fluid moves, it exerts force in all directions which can be defined using Newton's second law of motion also called the momentum equation. According to this law, a moving fluid particle exerts a force that is equal to the product of its mass and its acceleration in the direction of its motion. The law of conservation of momentum in tensor form for incompressible fluids like water can be written as Eq. (2.3).

Momentum x:

$$\frac{\partial(\rho u)}{\partial t} + \nabla \cdot (\rho u \mathbf{V}) = -\frac{\partial p}{\partial x} + \frac{\partial \tau_{xx}}{\partial x} + \frac{\partial \tau_{yx}}{\partial y} + \frac{\partial \tau_{zx}}{\partial z} + \rho g_x \tag{2.3a}$$

Momentum y:

$$\frac{\partial(\rho v)}{\partial t} + \nabla \cdot (\rho u \mathbf{V}) = -\frac{\partial p}{\partial y} + \frac{\partial \tau_{xy}}{\partial x} + \frac{\partial \tau_{yy}}{\partial y} + \frac{\partial \tau_{zy}}{\partial z} + \rho g_y \tag{2.3b}$$

Momentum z:

$$\frac{\partial(\rho w)}{\partial t} + \nabla \cdot (\rho u \mathbf{V}) = -\frac{\partial p}{\partial z} + \frac{\partial \tau_{xz}}{\partial x} + \frac{\partial \tau_{yz}}{\partial y} + \frac{\partial \tau_{zz}}{\partial z} + \rho g_z \tag{2.3c}$$

In compact notion as Eq. (2.4),

$$\frac{\partial(\rho \mathbf{V})}{\partial t} + \nabla \cdot (\rho \boldsymbol{V}) = -\nabla p + \mu \Delta^2 \mathbf{V} + \rho \boldsymbol{g} \tag{2.4}$$

Where ρ is the fluid density, μ is dynamic viscosity, τ is stress and $\boldsymbol{g}$ is the gravitational acceleration. The momentum equation (2.3a), (2.3b) and (2.3c) in the tensor form are called Navier-Stokes equations in conservation form.

Continuity and momentum equations, as well as energy conservation equations are made up of non-linear and coupled equations. For engineering problems, these equations cannot be solved analytically, although they can yield approximations. Computational Fluid Dynamics relies on these equations to function.

2.4 Water wave theories

To evaluate the forces experienced by offshore structures, an accurate depiction of the wave field created in offshore environments is required. External variables such as earthquake, wind, gravitational forces, and others generate waves in offshore areas. They form on the sea surface and have different properties based on the factors that contribute to their production. Table 2.1 categorizes the production of these waves based on the nature of forces. The bed slope and depth of a wave are the most noticeable features. The most accurate way to identify these properties, which can be classified as linear or non-linear, is to use water wave theories.

Table 2.1: Characteristics of metocean parameters with active regions

Wave Type	Mechanism	Period	Active region
Sound	Compressibility	$10^{-2} – 10^{-5}$ s	Ocean interior
Capillary ripples	Surface tension	$< 10^{-1}$s	Air-water interface
Wind waves	Gravity	1 – 25s	-
Tsunami	Gravity	10 min- 2 h	-
Internal waves	Gravity and density	2 min – 10 h	A layer of sharp density change
Storm surges	Gravity and earth rotation	1 – 10 h	Near coastline
Tides	Gravity and earth rotation	12 – 24 h	Entire ocean layer
Planetary waves	Gravity, earth rotation and depth	100 days	-

The linear wave theory only applies to waves of smaller amplitude. This is known as a small amplitude approximation, and it occurs only when the wave's amplitude is smaller than the wavelength and depth of the water. Table 2.2 shows the classification of water depths where wave amplitude us represented by λ and wave height is represented by h. To find any unknown quantity in linearized wave theory, known values of velocity potential, surface elevation, and dispersion relation are sufficient.

Table 2.2: Classification of sea water-based on the depth

Depth	Range
Shallow	$h < \frac{1}{20}\lambda$
Intermediate	$\frac{1}{20}\lambda < h < \frac{1}{2}\lambda$
Deep	$\frac{1}{20}\lambda < h$

Nonlinear wave theories, also known as finite-amplitude wave theories, are more complicated than linear wave theories because they require

higher-order terms to satisfy boundary conditions. Infinite power series are used to represent these high-order terms. Another significant distinction between the two theories is that in linear wave theory, equations are solved at the mean water level, but in non-linear wave theory, equations are solved at the sea surface. Stokes wave theory is the most often utilised nonlinear wave theory for CFD simulations, hence only this theory is discussed here.

2.4.1 **Stokes wave theory**

Stokes published his study of the behaviour of water waves in intermediate and deep waters in 1847. On non-linear gravity waves, perturbation analysis was utilised to find approximate solutions. In a non-linear system, periodic wave trains were discovered to be conceivable (Stokes, 1880). It was also discovered that, unlike linear waves, the speed of a non-linear system is determined by the wave amplitude. Initially, this theory was employed to represent irregular waves, but it was quickly expanded to include ocean waves. This theory is applicable for deep and intermediate waters when the ratio of wave height to water depth is small. The difference between the free surface elevation of ~~stokes~~ Stokes first order and the second-order wave is visible in Figure 2.7. Free surface elevation in terms of ~~stokes~~ Stokes first and second-order can be written as Eq. (2.5-2.6).

$$\eta = A\cos(kx - \omega t + \psi) \tag{2.5}$$

$$\eta = A\cos(kx - \omega t + \psi) + \frac{H^2}{2L}\frac{\cosh(kh)(2+\cosh(2kh))}{\sinh^3(kh)}\cos(2(kx - \omega t + \psi)) \tag{2.6}$$

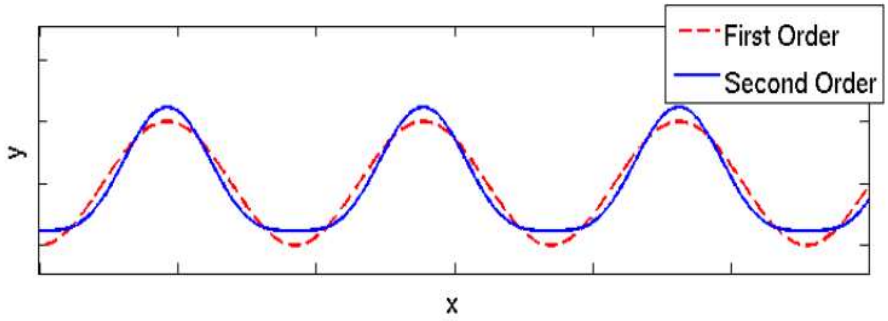

Figure 2.7: Free surface elevation of stokes first order and second-order wave (Young, 1999)

2.5 Numerical Wave Tank (NWT)

A numerical wave tank is a computer-based technique for simulating ocean conditions using CFD solvers. FLUENT, COSFLOW, CFX, REEF3D, OpenFOAM, and other CFD solvers can be used to create these wave tanks. The wave tank's dimensions are determined by the mesh size. Two-dimensional numerical wave tanks are the most commonly utilised to save processing power. The numerical wave tank's dimensions and time are usually set in metres (m) and seconds (s), respectively. The boundary conditions of numerical wave tanks are well defined to provide an offshore environment, as shown in Figure 2.8. The precise definition of boundary conditions is essential for error-free numerical wave tank simulations. The no-slip boundary conditions are typically used at the top and bottom of numerical wave tanks, although the Neuman condition can also be used. The no-slip condition is based on the assumption that the fluid at the boundary has zero velocity. A wavemaker is used to generate the wave at the numerical wave tank's intake. The wave can also be generated using User Defined Functions (UDF). The

outlet boundary condition acts as a numerical beach, with a dampening zone added to lessen the waves' reflecting effect.

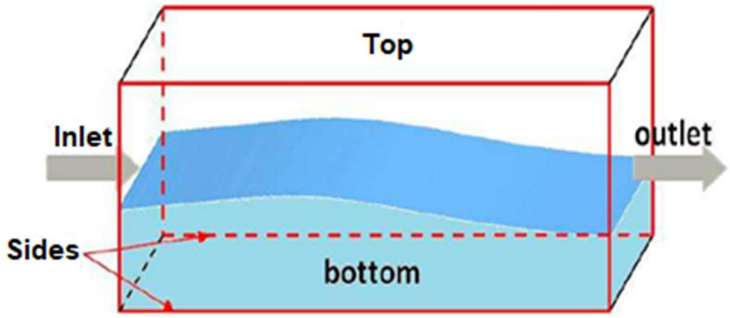

Figure 2.8: Sketch of numerical model with boundaries to generate numerical waves (Lambert, 2012)

2.5.1 **Turbulence Modelling**

At a low Reynold number, the flow is considered stable (laminar). Due to changes in velocity and pressure, the flow becomes unstable (turbulent) after a particular limit of Reynold number. Turbulence is a chaotic motion state in the flow field caused by these oscillations. Pressure gradient, wall roughness, and disturbances all have an impact on this condition.

RANS equations are the most preferred for turbulent flow computations because the fluid parameters based on averaged time are sufficient to resolve these chaotic motions. As demonstrated in Figure 2.9, the RANS equations are constructed by splitting fluid properties into steady mean and fluctuation components. Reynold's decomposition is a type of decomposition that is used to decompose fluid parameters such as velocity, pressure, and temperature. Eq. (2.7-2.8) is produced by decomposing the governing equation using Reynold's decomposition (x-direction).

$$\frac{\partial \overline{u_\iota}}{\partial x} = 0 \tag{2.7}$$

$$\rho \frac{D\overline{v_\iota}}{Dt} = -\frac{\partial \bar{p}}{\partial x_i} + \rho g_i + \mu \frac{\partial^2 \overline{v_\iota}}{\partial x_j \partial x_j} - \rho \frac{\partial\left(\overline{v'_\iota v'_j}\right)}{\partial x_j} \tag{2.8}$$

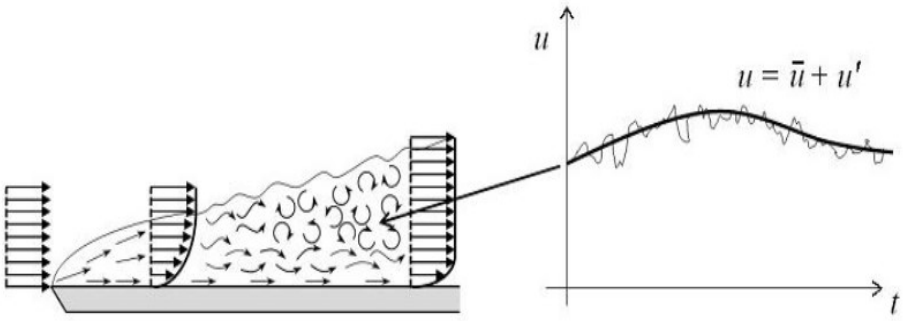

Figure 2.9: The decomposition of turbulent flow with Reynold's decomposition. The velocity decomposed into steady mean ū and fluctuating ύ components (Nagata et al., 2020)**.**

2.5.2 **Reynold's Averaged Navier Stokes (RANS) Equations:**

Reynold's Average Navier Stokes (RANS) equations are the time-dependent solution of the Navier Stokes (NS) equations. The RANS code is a well-known mathematical paradigm for resolving turbulent flows. This method consumes less computer power than Direct numerical simulation (DNS) method and solves complex fluid flow problems involving high Reynold number and complex model geometries. The RANS approach was originally developed for the prediction of rough flows where turbulence was defined by a single time scale regulated with huge motion scales. The assumption of time-indecency is false under unsteady turbulent flows which occur in the turbulent wake of the cylinder. To represent such a flow, time-dependent RANS formulations, such as unsteady RANS (URANS), are required. RANS results

show similar accuracies. RANS results, when compared to LES methods, reveal the same patterns with a reasonable degree of accuracy. Although LES simulation findings are more consistent with experimental outcomes than RANS, the differences between these two methods in terms of lift, drag, and Strouhal number make RANS a suitable candidate for modelling cylinder flow. RANS is frequently utilised in the motor and aerospace industries because it produces reasonably decent results at a lower computational cost. However, RANS still has a difficult time predicting transitions in the boundary layer. RANS utilises Reynold's decomposition for separating time-averaged and fluctuating components of an instantaneous quantity. However, RANS still has a difficult time predicting transitions in the border layer (Nagata et al., 2020). The equations are based on Reynold's decomposition, which decomposes an instantaneous variable into its time-averaged and fluctuating components. Almost all of the unsteadiness is modelled in the Reynolds averaged method to turbulence, and slow fluctuations in flow are especially solved. For water, which is an incompressible fluid by nature, Eq. (2.9) is the mathematical description of the RANS method.

$$\frac{\partial u_i}{\partial t} + u_j \frac{\partial u_i}{\partial x_j} = f_i - \frac{1}{\rho}\frac{\partial p}{\partial x_i} + v \frac{\partial^2 u_i}{\partial x_j \partial x_j} \tag{2.9}$$

where the decomposition quantities are given as Eq. (2.10).

$$u_i = \bar{u_i} + \acute{u_i}\,, p = \bar{p} + \acute{p} \tag{2.10}$$

The bar is the average quantity of parameters. When decomposition terms are also added in the RANS equation, a new form of RANS Eq. (2.11) is obtained.

$$\rho \frac{\partial u_i}{\partial t} + \rho \frac{\partial \overline{u_\iota}\, \overline{u_J}}{\partial x_j} = \rho f_i + \frac{\partial}{\partial x_j} \left[-\bar{p}\, \delta_{ij} + 2\, \mu \bar{S}_{ij} - \rho \overline{\acute{u}_\iota}\, \overline{\acute{u}_J} \right] \tag{2.11}$$

Where $\bar{S}_{ij}$ is the mean rate of strain tensor given as Eq. (2.12).

$$\bar{S}_{ij} = \frac{1}{2} \left(\frac{\partial \overline{u_\iota}}{\partial x_j} + \frac{\partial \overline{u_J}}{\partial x_i} \right) \tag{2.12}$$

Where u is the instantaneous component of velocity, $\bar{u}$ is the mean velocity, $\acute{u}$ is the fluctuating velocity, v is the kinematic viscosity and f_i external force.

Reynold's stress tensor is also used for solving the RANS equation when turbulent flow involves mean flow. This is a symmetric tensor of second order with six independent components. We have four unknown mean flow parameters for general three-dimensional flows, namely three velocity components and pressure. There are a total of ten unknowns where six unknowns are from Reynold's stress and four are from mean flow. All these ten unknowns can be determined by using the tensor form of the equation of mass and momentum conservations. To solve the problem, more equations or assumptions are required. The Boussinesq eddy viscosity assumption is the most extensively utilised assumption in RANS (Schmitt, 2007). The Reynolds stress tensor (τ_{ij}) is assumed to be proportional to the mean strain rate tensor (S_{ij}) given by Eq. (2.13).

$$\tau_{ij} = 2\,\mu_t S_{ij} - \frac{2}{3}\,\rho k \delta_{ij} \tag{2.13}$$

Where μ_t is eddy viscosity ~~term~~ and it is calculated from the transport equation ~~term~~. The last term in above Eq. (2.13) is used for the modelling of incompressible fluid like water. To make sure the turbulent kinetic energy is properly defined, Eq. (2.14) is derived.

$$k = \frac{\overline{u_i}\,\overline{u_j}}{2} \tag{2.14}$$

Boussinesq assumption of molecular viscosity affecting the laminar flow plays a vital role in turbulence model involving two equations. The two-equation turbulence model is the most simplified case of all the turbulence models because it considers the effect of mean flow on turbulence. This assumption introduces various scalar variables like turbulence energy and dissipation in the model and shows the correlation of these variables with other non-scalar variables such as intensity of turbulence and length scale.

2.5.2.1 ***k*-ε Model**

In this two-equation model, kinematic energy (k) and dissipation rate (ε) is used to solve the transport equations. In k - ε model, the eddy viscosity is obtained using Eq. (2.15).

$$\mu_t = C_\mu \rho \frac{k^2}{\varepsilon} \tag{2.15}$$

where C_μ is an empirical constant. By using a wall model near the circular cylinder's wall, the results can be enhanced. The turbulence viscosity ρ ~~(k)~~ and dissipation rate (ε) are fixed in this wall treatment model. Transport equations for k are Eq. (2.16) and ε is Eq. (2.17).

$$\frac{D}{Dt}(\rho k) = \frac{\partial}{\partial x_j}\left[\left(\mu + \frac{\mu_t}{\sigma_\varepsilon}\right)\frac{\partial k}{\partial x_j}\right] + G_k - \rho\varepsilon \tag{2.16}$$

$$\frac{D}{Dt}(\rho\varepsilon) = \frac{\partial}{\partial x_j}\left[\left(\mu + \frac{\mu_t}{\sigma_\varepsilon}\right)\frac{\partial \varepsilon}{\partial x_j}\right] + C_{\varepsilon 1}\frac{\varepsilon}{k}G_k - \rho\, C_{\varepsilon 2}\frac{\varepsilon^2}{k} \tag{2.17}$$

In which C_μ = 0.09, $C_{\varepsilon 1}$= 1.44, $C_{\varepsilon 2}$= 1.92, σ_k =1.0, σ_ε =1.3 and C_k represent the generation of kinetic energy caused by velocity differences due to position (A. D. Canonsburg, 2017).

Because of its resilience, computational economy, and reasonable accuracy, this model is widely utilised in industry. With the help of the (k- ε) model, Rodríguez et al. (2015) and Ye and Wan, (2017) found extremely high consistency in the values of lift and drag coefficients. This model makes effective use of the wall function to reduce PC power consumption. These wall functions, often known as empirical formulas, predict the flow accurately near the walls of the numerical model. However, while the wall function lowers the computing cost, it is insufficient to adequately describe a complex flow.

The k - ε model has three primary variations in Fluent (A. D. Canonsburg, 2017).

-Standard k-ε model (SKE): Despite its acknowledged drawbacks, it is commonly utilised due to its robustness. For complex flows with a high-pressure gradient, separation, and considerable streamline curvature, it performs badly. Early iterations, initial screening of alternate designs, and parametric research are all possible with it.

-Renormalization Group k - ε model (RNG): This model applies to any complex flow phenomenon involving vortices, medium to high spiral motion in a fluid, vertex shedding, small to the huge separation of fluid particles, flow involving separation of the boundary layer, transitional flow and many more.

-Realizable k - ε model (RKE): It has a lot of the same advantages and applications as RNG. The RNG may be more accurate and easier to converge.

2.5.2.2 k- ω Model

In RANS, k - ω has two equations and it utilises turbulent kinetic energy (k) and specific dissipation rate (ω) to solve the transport equations. The goal of this model was to get a decent prediction of force near a wall (M.Sundararaj, 2021).

The following transport Eq. (2.18-2.19) yields the turbulent kinetic energy, k, and the specific dissipation rate ω.

$$\frac{\partial}{\partial t}(\rho k) + \frac{\partial}{\partial x_i}(\rho k u_i) = \frac{\partial}{\partial x_j}\left(\tau_k \frac{\partial k}{\partial x_j}\right) + G_k - Y_k + S_k \tag{2.18}$$

$$\frac{\partial}{\partial t}(\rho \omega) + \frac{\partial}{\partial x_i}(\rho \omega u_i) = \frac{\partial}{\partial x_j}\left(\tau_\omega \frac{\partial \omega}{\partial x_j}\right) + G_\omega - Y_\omega + S_\omega \tag{2.19}$$

where G_k denotes the creation of turbulent kinetic energy caused by velocity differences due to position, G_ω denotes the generation of ω, S_k and S_ω denote user-defined source terms, Y_k and Y_ω denote dissipation, τ_k and τ_ω denote the effective diffusivity of turbulent kinetic energy and specific dissipation rate due to turbulence obtained by Eq (2.20-2.21).

$$\tau_k = \mu + \frac{\mu_t}{\sigma_k} \tag{2.20}$$

$$\tau_\omega = \mu + \frac{\mu_t}{\sigma_\omega} \tag{2.21}$$

where σ_k and σ_ω are turbulent constants known as Prandtl numbers, and μ_t is the viscosity due to turbulence. The more accurate treatment of flow near wall is provided by k - ω model. A tiny mesh is necessary near a wall because the nature of the flow impacts the boundary layer. This model, however, has a flaw: it is sensitive to free stream values.

2.5.2.3 **Wall Function**

The turbulent flows are greatly influenced by the walls due to high gradients near the wall. The modelling of a very thin viscosity layer produced near the wall necessitates a very fine mesh, whereas FLUENT allows a minimum of 10-20 cells for boundary coverage. When meshing up such a small region becomes impractical, the wall functions are utilised to connect the wall and the turbulent region. The ANSYS FLUENT community recommends an upgraded

wall function for the k-model. Wall functions are semi-empirical equations (A. D. Canonsburg, 2017).

2.5.3 **Equation discretisation**

The partial differential equations (PDEs) governing momentum conservation, mass conservation, turbulence transportation equations, and approximation equations must be solved in flow simulation. Equation discretisation is the process of converting differential forms of governing equations to discrete numerical counterparts to solve them using computers. These discrete numerical counterparts of differential equations don't produce any exact solutions, but they approximate the flow variables. The flow variables in computational fluid dynamics can be approximated using the ~~F~~ finite difference method, finite element method and finite volume method. The finite difference method (FDM) is very old ~~and simple to use the~~ method where Taylor expansion is used to solve the governing Partial differential equation (PDE). PDE derivates are distinct changeable entities obtained from mathematical equations solved at mesh nodes by computers. On fine meshes, this approach achieves more accuracy, but on rough meshes, it does not absorb momentum, energy, or mass.

The finite element method (FEM) is a quite young ~~and simple~~ method. It was created in the mid-to-late 1970s and courant was the first to apply this approach for fluid flow analysis (Lambert, 2012). In this method, a finite number of elements are partitioned into the computational domain. This method has successfully been used in the simulations of short waves

interacting with three-dimensional vertical cylinders. Contrary to FDM, FEM works best for coarse meshes and its performance is excellent for viscous flows involving free surface modelling. The simulation results match very well with the experimental work when comparison analysis is made. The only drawback of this method is that it is slow for turbulent flows involving complex and large model geometries.

In the finite volume method (FVM), the domain of computation is divided into very small cells or control volumes where PDE variables are converted to algebraic equations. The numerical solutions of the governing equations are explained using these algebraic equations. The algebraic equations in FVM are generated by integrating the governing equations within the cells/control volumes. Each control volume solves its neighbouring cells based on its own solution values. This way, the whole computational domain is solved for pressure, velocity, momentum and other variables involved in the model. FVM method is widely used in computational fluid dynamics because it applies to any complex turbulent and high-speed flow under structured and unstructured meshes. Most of the CFD solvers like ANSYS Fluent, Open Foam, and COSMOL are based on the Finite volume method (FVM). Fluent converts a general scalar transport problem into an algebraic equation that can be solved numerically using a control volume-based approach. Eq. (2.22) is a discretized equation for a given control volume. ~~can be represented as a discretized equation for a given control volume.~~

$$\frac{\partial \rho \varphi}{\partial t} V + \sum_{f}^{N_{face}} \rho_f \vec{v}_f \varphi_f \cdot \vec{A}_f = \sum_{f}^{N_{face}} \tau_f \nabla \varphi_f \cdot \vec{A}_f + S_\varphi V \tag{2.22}$$

Where $\vec{v}_f$ is the velocity factor, φ_f is coefficient of diffusion, N_{face} is the number of faces enclosed by the cells, $\rho_f \vec{v}_f \varphi_f \cdot \vec{A}_f$ is the vector product of mass flux to face area, V is control volume and S_φ is the source term of scalar φ.

2.5.4 **Spatial discretisation**

The computational domain is divided into smaller sub-domains with respect to time in spatial discretization. In CFD simulations, the upward spatial discretization scheme is most widely used because it derives the face value φ_f of each cell from the upstream cell are computed by using the multidimensional linear reconstruction method (Lintermann, 2021). The accuracy is achieved on each cell face using Taylor series expansion which expands cell centroid solution. The face value φ_f from Eq. (2.22) is calculated using the Eq. (2.23).

$$\varphi_f = \varphi + \nabla \varphi \cdot \vec{r} \tag{2.23}$$

where φ is cell-centred value, $\nabla\varphi$ cell-centred gradient and $\vec{r}$ is the displacement vector. This displacement vector direction is from the centroid of the upstream cell towards the centroid of the face. The spatial discretization

scheme is valid for all the RANS simulations involving various turbulence scalars like dissipation rate, kinetic energy and specific dissipation rate.

2.5.5 **Temporal discretisation**

Transient simulation is used in all of the current work's simulations, which means that the equation of continuity and momentum are discretized in time and space. For governing equations, a temporal discretization technique is required in addition to spatial discretization, where the differential form of the governing equation is integrated by time. This integration of the transient term is mathematically expressed as Eq. (2.4).

$$\frac{\partial \varphi}{\partial t} = F(\varphi) \tag{2.24}$$

where F considers any spatial discretization. Eq. (2.25) gives the first order correct temporal discretization when the time derivative is discretized using backward differences.

$$\frac{\varphi^{n+1} - \varphi^{n}}{\partial t} = F(\varphi) \tag{2.25}$$

and the second-order accurate form is Eq. (2.26).

$$\frac{3\varphi^{n+1} - 4\varphi^{n} + \varphi^{n-1}}{2\partial t} = F(\varphi) \tag{2.26}$$

where, n represents values in natural number and t is time step. This is temporal discretization.

In addition, the Courant number is kept around 1 to confirm the firmness of the numerical simulations and to produce reliable simulation outcomes. The Courant number is defined as Eq. (2.27).

$$CFL = \max\left(\frac{u\,\Delta t}{\Delta x}, \frac{v\,\Delta t}{\Delta y}, \frac{w\,\Delta t}{\Delta z}\right) \tag{2.27}$$

where, u, v, w present velocity in x, y, z directions.

2.5.6 **Pressure-velocity coupling**

The continuity and momentum equations both have velocity terms, while the momentum equation simply has pressure. To put it another way, the convective term and the continuity equations are intertwined. For incompressible fluid density is unrelated to pressure, determining the pressure of an incompressible fluid from its density is impossible.

In FLUENT, pressure and velocity coupling can be accomplished using either the segregated approach, which solves governing equations sequentially or the coupled method, which solves linked equations. The segregation algorithms SIMPLE, SIMPLEC, and PISO are used, whereas the coupling algorithm COUPLED is used. ANSYS recommends the PISO (A. D. Canonsburg, 2017).

2.5.7 **Boundary Setup**

The initial condition must be set for the variables involved in unstable flows. The initial condition for unstable flows is required to be set for the variables involved in the flow. For the analysis of incompressible fluid flows, the following four boundary conditions are most commonly used:

i. Solid wall
ii. Inlet and outlet
iii. Symmetry
iv. Free surface

2.5.8 **Solution Criteria**

CFD simulations are the result of a frequentative process that solves a set of linearized equations all at once. A repeating iterative approach achieves "convergence" for each conservation equation. The solution convergence is calculated by using the residual value obtained from the conservation equation because computer's have finite memory which causes inherent approximations. A double-precision solver is employed to reduce the influence of the round off error (A. D. Canonsburg, 2017). For all variables, such as velocities, turbulence parameters, and so on, the highest relative errors in this thesis were fewer than 10^{-5}.

2.5.9 **The volume of the Fluid Method (VOF)**

The air and water interface in the FLUENT is tracked by using the Volume of Fluid method. This method works on the volume fraction principle where each

fluid is determined in the form of a fraction from each mesh of the computational cell by using the volume fraction Eq. (2.28).

$$\frac{\partial \alpha}{\partial t} + \frac{\partial}{\partial x_j} \alpha \overline{v_j} = 0 \tag{2.28}$$

Where α is the volume fraction (phase fraction) of water and v is the velocity field. The value of α is dependent on the type of fluid and it is maximum in case of water and minimum in case of air so α=1 if the cell is filled up by water and α=0 if the cell is filled up by air. The volume fraction can also be used to determine the density of fluid inside the mesh cell because density will be required at a later stage to resolve the RANS equation. Mixture density can be expressed by using Eq. (2.29).

$$\rho = \alpha \rho_{\omega} + (1 - \alpha) \rho_{\alpha} \tag{2.29}$$

Where ρ_{ω} is water density and ρ_{α} is air density.

2.6 Verification and validation of Numerical Wave Tank (NWT)

In the discipline of ocean engineering, determining optimal ocean wave behaviour through modelling is critical. Numerical analysis is ideal for the study of oceans environments by using computer power. As processing power has developed, numerical models have become a more feasible option for modelling ocean waves. The building of a numerical model can be used to create numerical wave tanks.

Numerical models commonly use one of two types of equations: Stokes or Boussinesq theory for the simulation of hydrodynamics of the waves. Stokes theory applies to a wide variety of water depths, whereas Boussinesq theory only applies to shallower water depths (Kim et al., 2017). The Boussinesq theory is hard to use as compared to stokes wave theory since it is more complex. CFD simulations that involve Boussinesq theory have certain drawbacks, such as the inability to simulate the breaking of the water waves without losing wave energy. On the other hand, it is easy to adopt stokes theory for numerical modelling because it is simple to use. Stokes theory is applicable to various water depths and has been applied by many researchers in their numerical models by using ANSYS Fluent (A. D. Canonsburg, 2017).

It is critical to test and validate the results, regardless of the numerical wave tank's underlying equations. The validation is carried out by comparing the simulation results of the numerical model with the analytical or experimental results of the reference experiment (Prasad et al., 2017). This comparison gives a measure of how precise the simulations results are when it is compared with the experimental work.

2.6.1.1 **Numerical Wave Maker**

Wave generation in a numerical wave tank is a difficult undertaking since CFD simulations in a numerical wave tank may have to cope with complex flow phenomena. Physical wavemakers such as pistons and paddles can be

replicated in a wave tank, or numerical/mathematical techniques can be used. Because the former method has large computing costs and is difficult to apply in CFD, the latter method is utilised to generate the wave. Using the numerical methodology, the wave in a numerical wave tank can be generated in four different ways:

i. Relaxation method
ii. Boundary method
iii. Mass source method
iv. Impulse source method

The Boundary element method (BEM) is an example of the first method, which is based on the results of wave theory or another numerical model. The second method entails generating and absorbing waves on borders using direct boundary conditions. With the addition of the source term to the continuity equation, the third technique yields a wave. By adding a source term to the impulse equation, the final technique generates a wave. The simulation of a regular wave is used to assess the wave generation technique's correctness. The numerical wave developed at the inlet boundary has certain wave parameters like wavelength, wave period, wave height and wave steepness.

2.6.1.2 **Wave Beach**

A wave dampening zone is used to introduce the wave beach at the numerical wave tank's outlet. To eliminate the wave reflection phenomenon, the damping

domain of a numerical wave tank should be larger than the computational domain.

2.7 Fluid-Structure Interaction

Fluid-structure interaction (FSI) applications include offshore fixed and floating structures, as well as offshore pipelines. The calculation of loads operating on structures is the most important component of civil engineering from the aspect of safe, sound, and cost-effective design. These computations are based on a variety of factors, including load category (static or dynamic), wave type (breaking or non-breaking), structure dimension, and flow regime (separated or non-separated). The importance of Reynold's number in determining the flow regime cannot be overstated. Aside from that, the Keulegan-Carpenter (KC) number and the Froude (Fr) number are crucial in determining the relationship between flow and structure force. Table 2.3 explains the importance of all these dimensionless values.

Table 2.3: Most important dimensionless numbers in Fluid Dynamics

Number	Equation	Characteristics
Reynolds	$Re = \frac{UD}{v}$	Distinguish flow regime between laminar and turbulent
Froude	$Fr = \frac{U}{gL}$	Characterize the resistance of bodies passing through fluids
Keulegan-Carpenter	$KC = \frac{U_m T}{D}$	Make comparisons between inertial forces and drag coefficient

2.7.1 Flow around a circular cylinder

Numerical simulations work best at low Reynolds numbers under laminar flow conditions. The boundary layer becomes thick at low subcritical Reynolds number, so it is easier for reasonably coarse grids to solve this flow (Catalano et al., 2003). The boundary layer becomes thinner at a high Reynolds number causing the flow to be turbulent in nature. The higher the Reynolds number, the more computational power will be needed to solve the flow (Kang et al., 2015). As a result, the Reynolds number has an inverse relationship with the computer resources and simulation time required.

The Direct numerical simulation (DNS), Large Eddy Simulation (LES) and Reynolds-averaged Navier-Stoke (RANS) methods are commonly used to study the flow interacting with structure at high Reynolds number (Wornom et al., 2011). The simulation's accuracy is determined by the precision of the transition point and turbulent wake predictions. Dong and Karniadakis, (2005) studied the interaction of fluid with circular cylinder at high Reynolds number by using Direct numerical simulations. The CFD results of lift, drag and pressure coefficient were compared with the reference experimental results. The results showed a very good agreement, but author suggested to use other low computing CFD method like DNS and RANS for future studies. Abrahamsen Prsic et al. (2014) performed a similar study using LES method for a Reynold number of 20000 and pointed out some limitations of the method including high computational cost and large simulation time. RANS method is computationally less expensive, but it requires some turbulence model for the treatment of wall functions because performance of this method

is poor near boundary walls. The proper selection of input values determines the precision of the output values (Kulyakhtin, Shipilova & Muskulus 2014).

2.7.2 **Regime of Flow**

Reynold number (R_e) ~~(Re)~~ play a key role in fluid-structure interaction (FSI) studies involving circular cylindrical structures in the flow regime. This dimensionless number is very important for the determination of velocity or cylinder diameter during structural design process. In a constant subsonic flow, vortex shedding from a smooth, circular cylinder is a function of Reynolds number. Mathematically, Reynolds number (R_e) ~~(Re)~~ can be written as Eq. (2.30).

$$R_e = \frac{UD}{v} \tag{2.30}$$

Where U is velocity of the fluid, D is the diameter of the circular cylinder, and v is the kinematic viscosity of the fluid. Mathematically, kinematic viscosity can be expressed as Eq. (2.31).

$$v = \frac{\mu}{\rho} \tag{2.31}$$

Where ρ is density and μ is dynamic viscosity of the fluid.

With increasing Reynolds number, the properties of the flow around a smooth cylinder alter. Wake transition (TrW), shear layer transition (TrSL), and boundary layer transition (TrBL) are among the transitions from laminar to turbulence documented by Boiko et al. (2015) in diverse places. There is no separation at an extremely low Reynolds number ($R_e < 5$) ~~($Re < 5$).~~ Larger

Reynolds numbers cause separation and wakefulness, which are referred to as vortices. Initially, transition starts from the wake zone as R_e increases from 40, and turbulence generate at the end of the cylinder. When Reynolds number is in the range of 180 to 400, alternate vortices split on two opposite ends. The shear layer is where the next transition occurs. As R_e grows, the transition region draws closer to the separation point. The TrSL regime can be found in R_e ranges of 350 to $2x10^5$. The boundary layer is the next transitional zone, and it is receiving the most focus in current study. The effect of Reynolds number on the boundary layer in this regime is divided in three groups. The subcritical range is defined as the Reynolds number being less than 2×10^5. The associated boundary layer is laminar in this range of Reynolds numbers, where differential layer is under mode of change with totally turbulent wake. Reynolds number range between 2×10^5 and 3.5×10^6 is called critical range. The boundary layer begins as laminar in this range and eventually separates with turbulent reattachment, a separation bubble, and turbulent boundary layer separation. The supercritical region is defined by a Reynolds number larger than 3.5×10^6 (Nagata et al., 2020). Outer layer is laminar in nature before separation and becomes turbulent with increase in Reynolds number. The regime of fluid around cylindrical structure with transitional values of R_e are shown in Figure 2.10.

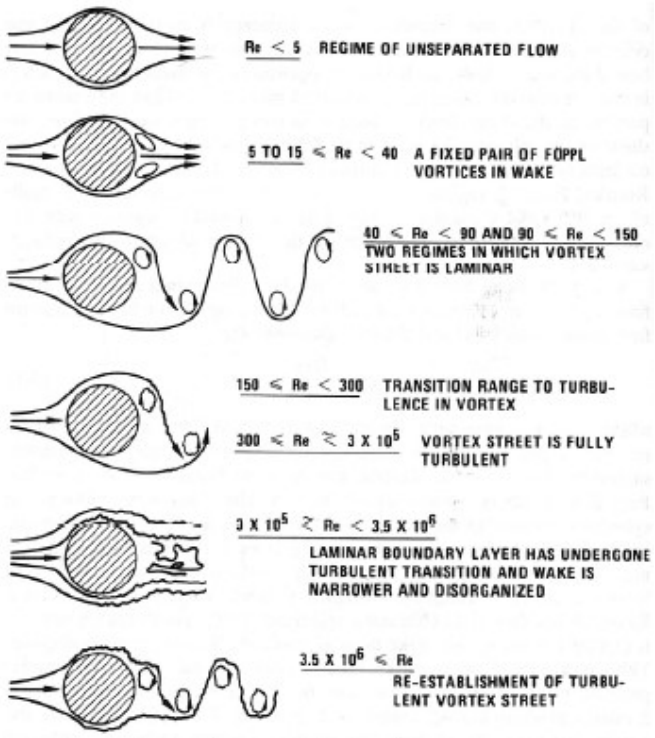

Figure 2.10: Different flow regimes around the circular cylinder (Nagata et al., 2020)

2.7.3 **Vortex Shedding**

It is a phenomenon which occurs when water or air passes through solid material at different speeds according to the shape and size of the body (Zhang et al., 2021). In this flow, vortices form downstream and separate from both sides of the body at regular intervals. The dimensionless *Strouhal number* (S_t), is a popular metric for determining the main shedding frequency, f_s ~~fs,~~ and is defined as Eq (2.32).

$$S_t = \frac{f_s D}{U} \tag{2.32}$$

where f_s is the frequency of vortex shedding, U is fluid velocity and D is the diameter of the cylinder. The value frequency relies on the magnitude of Reynolds number. It has little to no dependence on the roughness of the surface, except in the region of transition ($3x10^5 < R_e < 3x10^6$), as shown ~~seen~~ in Figure 2.11.

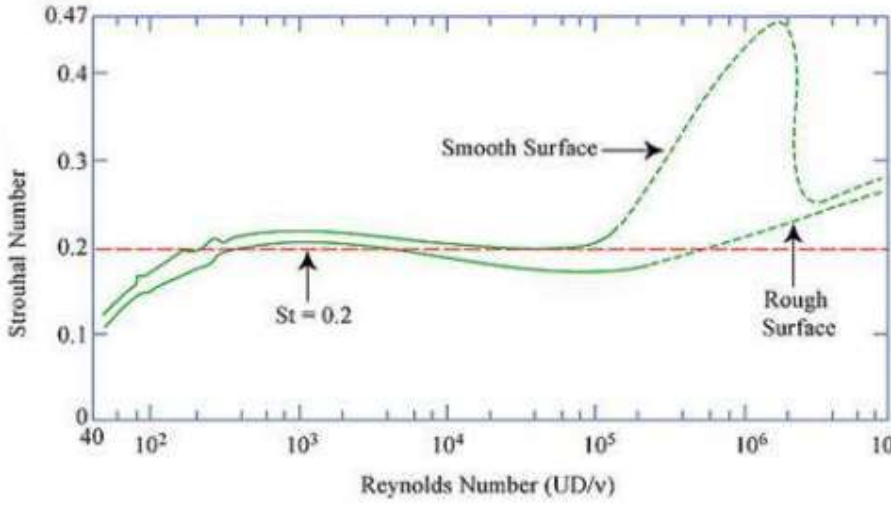

Figure 2.11: Relation of *Re* and *St* around circular cylindrical structure (Nagata et al., 2020)

2.7.4 Drag, Lift and Pressure Coefficient

Coefficient of force is important for the determination of coefficient of drag, lift and pressure around the circular cylinder. As illustrated in Figure 2.12, the drag force working on the cylinder is parallel to the direction of flow, but the lift force working on the cylinder is perpendicular to the flow. The coefficient of lift and coefficient of drag are influenced by Reynolds number, shape and orientation of the body. The coefficient of drag, *Cd*, is obtained by using Eq (2.33).

$$C_d = \frac{F_d}{0.5\,\rho U^2 A} \tag{2.33}$$

Lift coefficient, Cl is similarly defined as Eq. (2.34).

$$C_l = \frac{F_l}{0.5\,\rho U^2 A} \tag{2.34}$$

where A is area of projection towards flow, Fd is the force generated by drag in the body, Fl is the force generated by the lift in the body. These lift and drag forces are force per unit length.

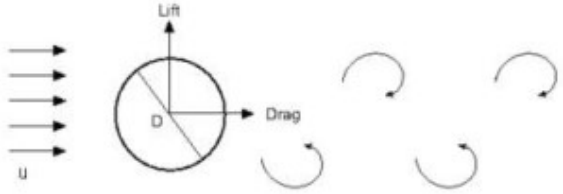

Figure 2.12: Direction of lift and drag force around the circular structure (Yang et al., 2015)

The drag force for flow past a circular cylinder oscillates at twice the frequency of the lift force in theory. When lift and drag forces are split into mean and oscillatory components, it can be observed that the mean drag coefficient, $C\overline{d}$, for flow with a laminar boundary layer (Re < 10^5), is about 1, whereas the mean lift coefficient is nil. The fluctuating lift coefficient, Cl', is, on the other hand, bigger than the oscillating drag coefficient. Turbulence models must appropriately calculate force coefficients when modelling flow via a cylinder.

Aside from forces, coefficient of pressure, Cp as defined by Eq. (2.35) is a crucial factor to consider.

$$C_p = \frac{p_c - p}{0.5\,\rho U^2} \tag{2.35}$$

Where pressure on cylinder surface is represented by p_c, static pressure is expressed as p, and stagnation point is $\rho U^2/2$. In the numerical modelling, exact determination of pressure coefficient (C_p), distribution of lift and drag forces near cylinder with separation of stagnation are very important for simulations under turbulence.

2.7.5 **Vortex Pattern**

Single vortices (S) and vortex pairs (P) make up the periodic vortex wake pattern for a cylinder, resulting in patterns like S, P, 2S, 2P, S+P, and 2P+2S. As shown in Figure 2.13 (a), the sorts of vortex patterns are determined by the dimensionless amplitude (A* = A/D) and wavelength ratio $\lambda* = \lambda$ (/D).

Each half-cycle, (Zhang et al., 2021) discovered a new triplet vortex, having a designation of 2T when dimensionless amplitude is bigger than 1.5. Different patterns of vortex shedding cause different effects on the structure, which contribute to the overall motion of the cylinder's amplitude. Figure 2.13 (b) depicts a more comprehensive illustration of each vortex-wake pattern. At the crucial curve, the switch from one kind of vortex production to another occurs.

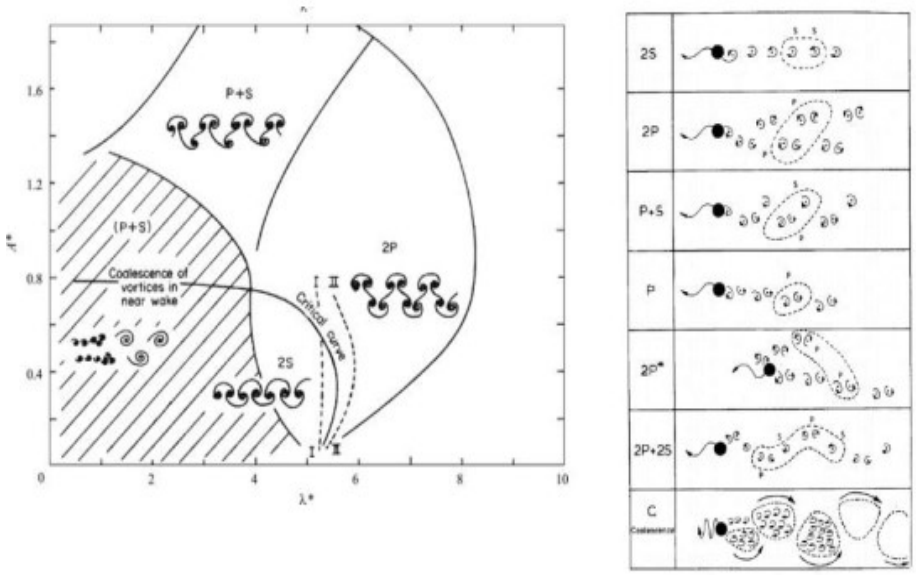

Figure 2.13: (a) A layout of vortex activity pattern, (b) Vortex wake patterns feature (Anderson et al., 2020)

2.8 Summary

Generation of waves in the numerical wave tank (NWT) by using computational fluid dynamics (CFD) is reviewed in this chapter. Water waves in a numerical wave tank can be generated either by replicating physical wavemakers like a piston, paddle etc. or by using numerical/mathematical techniques. The former technique requires high computational costs and is difficult to implement in CFD, so the latter technique is used for the generation of waves. The generated wave should have characteristics like wavelength (L), wave height (H) and wave steepness (H/L). These waves can be superimposed by other met ocean parameters like offshore currents by adding the velocity component of current to wave equations. For error-free simulations, a wave tank should be provided wave beach to avoid any wave reflection. Classification of offshore waters should be carried out by water

wave theories. Airy and stokes waves are most commonly used for shallow or intermediate waters because the offshore structure of fixed type is operational only in these regions.

CHAPTER 3

METHODOLOGY

This chapter contains research methods used in this study. To investigate the metocean interaction behaviour model with offshore structure near the free surface; four different modelling scenarios are used in this thesis. First two scenarios involve generation of offshore waves in a numerical wave tank while structure is introduced in last two scenarios. The CFD simulations are carried out in ANSYS FLUENT software.

3.1 Operational Framework

CFD is proving to be a practical field of complex fluid flow analysis for the industry, with quite accurate predictions. Experiments for complex fluid flow analysis have certain limitations like limitations of cost, space and measurements so mostly CFD users validate and verify simulation set-up from reference experiment available in the literature. Experimental work of (Chen and Ballengee, 1971; Dingemans, 1994; Rolf Jarle, 2001) are referred in this thesis for comparison of CFD results obtained using ANSYS FLUENT software for free surface flow modelling and fluid structure interaction analysis. These three works are referred because they are classical set of experiments which are most widely cited in CFD studies to validate and verify the basic numerical models.

Workbench by ANSYS incorporation is easy to use because it integrates all the modelling tools from geometry to post-processing at one place with drag and drop facility. DESIGN MODELER or SPACECLAIM are geometry building tools. They can create any type of two- or three-dimensional model geometry from simple to complex very easily. Once the model geometry is built, ANSYS meshing tool is used to convert the whole computational domain into tiny fragments called cells or control volumes. The control volumes are used to solve governing equations of fluid flow for flow problems. ANSYS FLUENT is used to solve these flow equations and it work as a CFD solver. Once the model processing is carried out, CFD-Post by ANSYS is used for model post processing to generate the results in various formats. ANSYS FLUENT CFD solver is used in this study because it is a well know CFD solver which has been most widely used in Chemical and Aerodynamics field involving compressible and incompressible fluids. The use of FLUENT software is generally established in vast majority of fields, and the results produced by software are considered as dependable. A good agreement is found when simulation results produced by this tool were compared with reference experimental works. The graphical user interface (GUI) of this software is very user friendly so it can be adopted for any complex flow analysis without years of experience in the field. Fluent's powerful solver technologies deliver rapid, accurate CFD results, as well as adjustable dynamic and distorting meshes, which are crucial for this study.

3.2 Scenario 1: Flow in a rectangular tank

In the beginning, a simple two-dimensional rectangular wave tank as shown in Figure 3.1 was developed to generate the waves in the wave tank. The length of this numerical wave tank is chosen 24 m whereas the height of the tank is kept 1 m. The accuracy of waves generated in the numerical model was determined by estimating the simulation outcomes with the analytical wave profiles generated by ~~stokes~~ Stokes second-order wave theory.

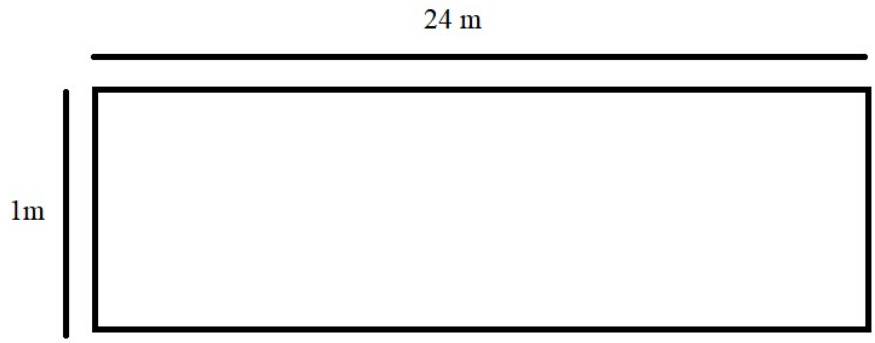

Figure 3.1: The geometry of the numerical wave tank to model the flow over a rectangular tank for the comparison of free-surface elevation with ideal wave profiles obtained using Stokes second-order wave

3.2.1 Stokes second-order wave

In metocean interaction modelling with offshore structures, reliable numerical wave generation in the numerical wave tank is critical. Many wave theories exists but in CFD simulations, Stokes second order wave theory is most widely used due to its simplicity. It is non-linear in nature and it can generate regular waves in numerical offshore environments. Higher order of Stokes wave like Stokes fifth order wave theory do exists but they are not adopted for intermediate/deep water modelling because of complex high order terms in the equations. Due to these reasons, second order wave is used in this scenario.

3.2.2 **Velocity of the Particle**

The velocity of the water particle under Stokes 2nd order wave theory is separated in two components (horizontal and vertical). The horizontal and vertical velocity components are represented by *u* and *w* respectively. Mathematically, they can be expressed as Eq. (3.1-3.2).

$$u = \frac{\partial \varphi}{\partial x} = \frac{H}{2}\frac{gk}{\sigma}\frac{\cosh k\,(h+z)}{\cosh kh}\cos(kx-\sigma t) + \frac{3}{16}\frac{H^2\sigma k\cosh 2k\,(h+z)}{\sin^4 kh}\cos 2\,(kx-\sigma t) \tag{3.1}$$

$$w = -\frac{\partial \varphi}{\partial z} = \frac{H}{2}\frac{gk}{\sigma}\frac{\sinh k\,(h+z)}{\cosh kh}\sin(kx-\sigma t) + \frac{3}{16}\frac{H^2\sigma k\sinh 2k\,(h+z)}{\sin^4 kh}\sin 2\,(kx-\sigma t) \tag{3.2}$$

Where *H* is wave height, *g* is acceleration due to gravity, *h* is depth of water, *x* is horizontal distance, *t* is time, *k* is wave number, σ is wave frequency and *z* is free surface elevation which is zero at still water level (SWL). Wave frequency σ and wave number *k* can be determined using Eq. (3.3-3.4). *L* in Eq. (3.4) is length of the wave commonly known as wavelength.

$$\sigma = \sqrt{gk\tanh kh} \tag{3.3}$$

$$k = \frac{2\pi}{L} \tag{3.4}$$

3.2.3 **Confirmation of the validity of stokes second-order wave**

Dean & Dalrymple (1991) found that stokes second order waves cannot be used in shallow water because of its higher wave height. They defined the shallow water where water depth is less than 1/20th wavelength and deep water as water depth equal to or more than half of wavelength. Ursell parameter is a very good technique to determine the suitability of stokes second order wave theory based on water classification. The Ursell parameter is utilised for checking the validity of this theory by measuring the nonlinearity of ocean waves in a fluid. Eq. (3.5) is a mathematical expression for the Ursell parameters.

$$\frac{L^2 H}{h^3} < \frac{8\pi^3}{3} \tag{3.5}$$

Stokes equation for the 2nd order waves is applicable once the Ursell parameter is satisfied. All the scenarios in this research involving waves satisfied this condition.

3.2.4 **Surface elevation of the waves**

The water surface displacement also called surface elevation (η) is the distance when surface of water body is moved from the level of stationary water. It has a unit of meter (m) and it can be expressed as Eq. (3.6) for stokes second order wave (Lambert, 2012).

$$\eta = \frac{H}{2}\cos(kx - \sigma t) + \frac{H^2 k}{16}\frac{\cosh kh}{\sinh^3 kh}(2 + \cosh 2kh)\cos 2(kx - \sigma t) \quad (3.6)$$

The numerical waves surface height was compared to the ideal wave height obtained using stokes equation for 2nd order waves. The Root Mean Square Error (RMSE) given by Eq. (3.7) is the determination of model's correctness.

$$RMSE = \sqrt{(f - o)^2} \quad (3.7)$$

Where *f* = forecasts (ideal/theoretical value), o = observed values (simulation results).

3.2.5 **Grid dependency test**

A mesh grid dependency test was done before producing the simulation results for comparison. Four different grid resolution of the mesh were generated to determine the most suitable mesh resolution. The details of the mesh grid resolution used in this scenario are given in Table 3.1.

Table 3.1: Size of mesh elements used in meshing test for a simple flat bottom rectangular wave tank.

Mesh	Elements
A (Coarse)	8325
B (Medium)	18991
C (Fine)	302196
D (Extra Fine)	601510

3.2.6 **Wave parameters for simulation**

The experiment by ~~(Dingemans, 1994)~~ (Dingemans, 1994) employs three different waves named as Case A, Case B and Case C with wave characteristics as shown in Table 3.2. The findings of simulations utilising Case A wave characteristics are compared to analytical and experimental results in this thesis. The first condition is used for the mesh test only. It is important to note that Case A and Case C waves are non-breaking in nature while Case B wave is spilling breaker. The validation is carried out with comparison of numerical wave elevations obtained from CFD simulations and theoretical wave elevations obtained from Eq. (3.6). The details of the wave parameters are given in Table 3.2. All the waves are confirmed to be stokes second-order waves because their Ursel parameter number is less than 82.55 as calculated in Appendix A, B and C.

Table 3.2: Parameters of the wave utilised for validation (scenario 1) and verification (scenario 2) tank

Condition	Wave Height (m)	Wavelength (m)	Wave Period (s)	Water Depth (m)	Ursell Paramter
Mesh Test	0.1	5	1.94	1	2.5
Case A	0.02	3.738	2.02	0.4	4.3664
Case B	0.029	4.791	2.525	0.4	10.4
Case C	0.041	1.488	1.01	0.4	1.41

The free surface elevation of the simulated waves for the grid convergence test is measured at a different location. The position of the gauges located in the tank is given in Table 3.3.

Table 3.3: Location of wave gauges in the flat bottom rectangular tank used for the validation

Gauge Number	Horizontal Position (m)
1	2
2	4
3	6
4	8
5	10
6	12
7	14
8	16

3.2.7 Model setup

Once the model geometry with mesh is developed, it is time to model setup in ANSYS Fluent. The model is set up by using Fluent 18.1 software, where a pressure-based solver is used with transient flow condition. Model precision is kept at double precision. The gravitational acceleration g is triggered in the negative y direction. The implicit body force formulation option is enabled, as well as interfacial anti-diffusion. The volume fraction is set to implicit by default for open channel flow problems since it allows for a greater time step size.

The air is chosen to be primary material and water as secondary material for the multiphase modelling. The default properties of these two materials are selected from Fluent Database. In operational conditions, the

density of the lightest phase is chosen as the working density. This reduces hydrostatic pressure build-up in the lighter phase, improving momentum balance round-off precision. The free surface modelling involves water and air in the tank where water is given a score of 1 when it is 100% filled and air is given a score of 0 when it is fully filled. The score of 0.5 is assigned to free surface containing 50% water and 50% air in the region. It's also critical to give a reference pressure position, which reaches to a point where fluid is remains in one of the phases at 100%. When this is not possible, locate a place where the pressure remains constant for a certain amount of time. This situation is necessary for a quick and even convergence, and it ensures that pressure computation round-off is kept to a minimum. Static pressure variations are more severe in denser fluid so velocity distribution position for the measurement should be in thinner phase. As a result, the reference pressure position is set to the left side of the computational area, which is totally occupied by air.

To generate the best ideal waves, the inlet boundary of the wave tank is designed to be a velocity inlet without considering the effect of ambient current, therefore the magnitude of flow velocity is taken as zero. For wave theory, Stokes second order wave is used. The downstream border is set to a pressure outlet, where the direction of backflow fluid is set to "Normal to Boundary" with method of density interpolation to "From Neighboring Cell." The volume fraction derived from the surrounding cell is then utilised to interpolate the density used in the hydrostatic profile. The values of volume fraction in ANSYS Fluent software are computed internally by using the

values of nearby cells, therefore it is done automatically. The free surface level must be indicated again at the outflow boundary. In open channel modelling, splitting is not allowed because the outlet can only be a single outflow border. Symmetry conditions is applied at the top of the numerical wave tank while bottom is chosen as a wall with no-slip boundary conditions.

ANSYS recommends using a second-order upwind technique to discretize the energy and momentum equations. It recommends the use of upwind scheme in first order to dissipation. The recommendations are followed for all flow equations in discretization scheme. The default gradient scheme method is least square cell based scheme so it is applied in flow analysis. The recommended method for pressure interpolation by ANSYS is PRESTO. This method is applied for pressure interpolation of Volume of fluid (VOF). The volume fraction in VOF multiphase modelling is applied as “compressive”. Because there were problems with convergence when the transient formulation was changed to second order, it is now set to "First Order Implicit." Despite the fact that ANSYS advises PISO with non-iterative time advancement (NITA), the 2D simulation in this project is done using the Coupled method. The reason for this decision is because PISO seems to produce more x-momentum divergence than the Coupled scheme. The simulation is started using the Hybrid initialization approach and "computing from Inlet boundary." The number of time steps is set to 60000 with size of each time step set to 0.001 second. The total simulation time is now 60 seconds.

3.3 Scenario 2: Flow over a submerged bar

A rectangular wave tank with submerged bar located in the middle of the tank is used for the verification as shown in Figure 3.2. The verification is carried out by comparing the simulation results with the experimental results obtained by Dingemans, (1994). The wave gauges located in the numerical wave tank are positioned in Figure 3.2. The exact location of each numerical wave gauge to record the free surface elevation is given in Table 3.5.

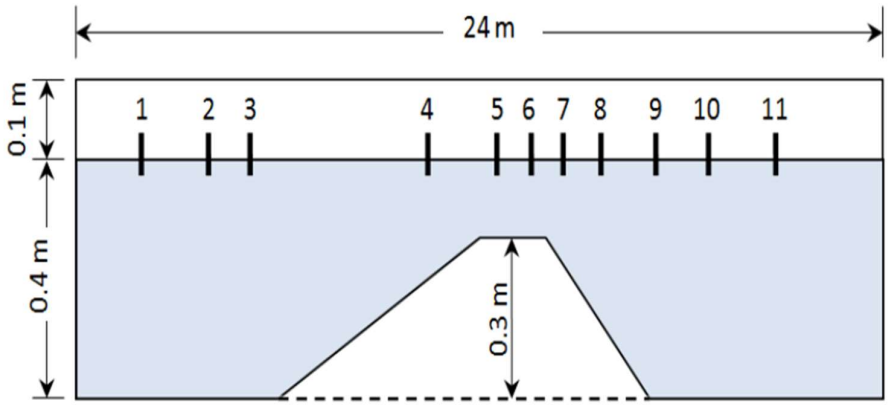

Figure 3.2: Geometry of simulation setup to model the flow over a tank with submerged bar for the comparison of free-surface elevation with ideal wave profiles obtained by Dingemans, (1994) **in his experiments**

3.3.1 Mesh Generation

A mesh grid dependency test was done before producing the simulation results for comparison. Four different grid resolution of the mesh was generated to determine the most suitable mesh resolution as show in Figure 3.3. The details of the mesh grid resolution used in this scenario are given in Table 3.4.

Table 3.4: Size of mesh elements used in meshing test for submerged bar wave tank

Mesh	Elements
A (Coarse)	60319
B (Medium)	120340
C (Fine)	413219
D (Extra Fine)	832103

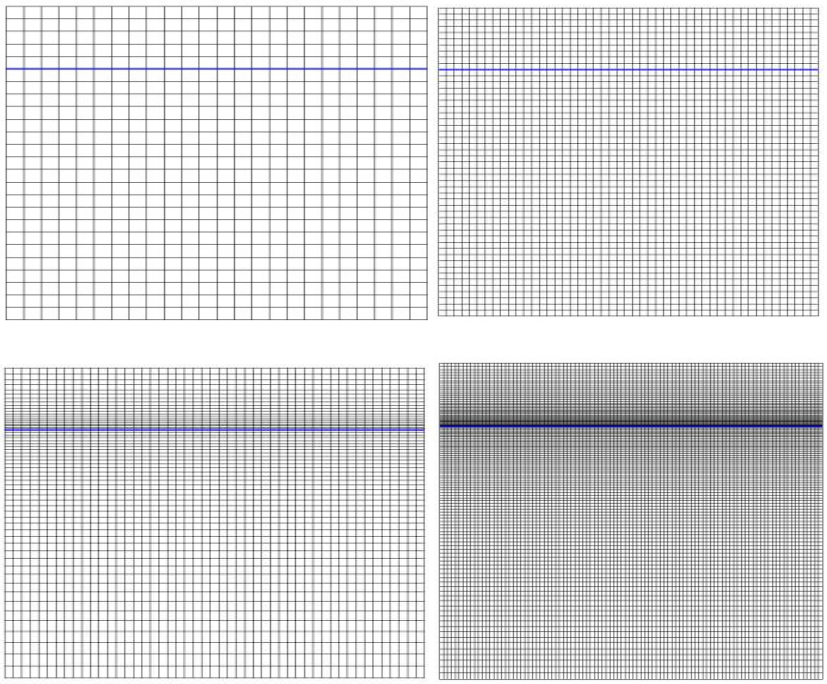

Figure 3.3: A partial view of four different grid resolution of mesh generated for the numerical wave tank to model the flow over a tank with submerged bar

3.3.2 Production of Boundary Conditions

The input parameters and boundaries of the simulation model should be chosen to mimic physical behaviour so that the simulation results generate same output when compared with the physical model. There are four

boundaries in this numerical wave tank: inlet, outflow, atmosphere, and bottom.

3.3.3 **Wave Generation at the inlet Boundary**

The inlet boundary of numerical model is set to be a velocity inlet without considering the effect of current to generate best ideal waves, so the magnitude of turbulences is kept zero. Stokes second order wave is applied for wave theory.

The free surface elevation of the simulated waves for grid convergence test and experimental comparison is measured at the same location. It is important to note that the position of wave gauges for meshing test and experimental comparison is the same. For both simulations, the wave with Case A parameters of Table 3.2 is used. The same wave was used by (Dingemans, 1994) in his experimental work. The position of the gauges located in the tank is given in Table 3.5.

Table 3.5: Location of wave gauges in the submerged bar wave tank used for the verification

Gauge Number	Horizontal Position (m)
1	2
2	4
3	5.7
4	10.5
5	12.5
6	13.5
7	14.5
8	15.7
9	17.3

10	19
11	21

3.3.4 **Wave Reflection Prevention at the outlet**

The waves generated in the tank are prevented for wave reflection by specifying the outlet of the tank as pressure outlet. The backflow direction of downstream boundary is taken as normal to boundary. The volume fraction derived from the surrounding cell is then utilised to interpolate the density used in the hydrostatic profile. Fluent computes the data of volume fraction internally from surrounding cell values, therefore it is done automatically.

3.3.5 **Other Boundary Conditions**

The bottom of tank is chosen a no-slip wall boundary condition. The top boundary is chosen as a symmetry with pressure outlet.

3.3.6 **Solver Settings**

The momentum and turbulent kinetic energy are discretized using the second-order upwind method, while the dissipation rate is discretized using the first-order upwind strategy. The default gradient scheme in Fluent is the cell based. In VOF multiphase simulations, ANSYS suggests using "PRESTO!" for pressure interpolation and "Compressive" for the volume fraction. Because there were problems with convergence when the transient formulation was changed to second order, it is now set to "First Order Implicit." Despite the

fact that ANSYS advises PISO with non-iterative time advancement (NITA), the 2D simulation in this project is done using the Coupled method. The reason for this decision is because PISO seems to produce more x-momentum divergence than the Coupled scheme.

3.3.7 **Physical Properties**

For multiphase modelling, air is chosen as the major material and water as the secondary material. As shown in Table 3.6, the default attributes of these two materials were chosen from the Fluent Database. Working density in operating conditions is chosen as the density of the lightest phase. This improves momentum balance round-off precision by reducing hydrostatic pressure build-up in the lighter phase. The free surface modelling uses water and air in the tank, with water receiving a score of 1 when completely filled and air receiving a score of 0 when completely empty. A free surface in the region with 50 percent water and 50 percent air is given a score of 0.5. It's also crucial to provide a reference pressure position that reaches a point where the fluid is completely contained in one of the phases. If this isn't possible, find a location where the pressure stays constant for a period of time. This situation is necessary for a quick and even convergence, and it ensures that pressure computation round-off is kept to a minimum. Static pressure variations are more severe in denser fluid so velocity distribution position for the measurement should be in thinner phase. As a result, the reference pressure position is set to the left side of the computational area, which is totally occupied by air.

Table 3.6: Physical properties of model

Parameter	Value
Gravity	9.81 ms^{-2}
Density of water	1000 kg m^{-3}
Kinematic viscosity of water	1.0 x 10^{-6} m^2 s^{-1}
Density of air	1.2 kg m^{-3}
Kinematic viscosity of air	1.48 x 10^{-5} m^2 s^{-1}
Surface tension	0.07 Nm^{-1}

3.3.8 **Control Properties**

The simulation is started using the Hybrid initialization approach and "computing from Inlet boundary." The number of time steps is set to 60000 and the size of time fraction is chosen to be 0.001 s. The total simulation time is now 60 seconds.

3.4 Scenario 3: Flow in a tank with circular structure

To study the interaction of the fluid with structure, a numerical tank with a circular cylinder is used in this scenario of study as shown in Figure 3.4. The generated results are compared with available experimental and numerical work.

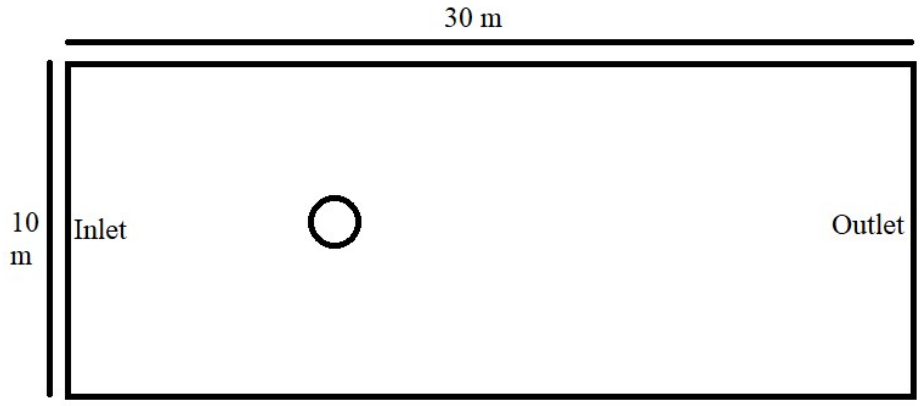

Figure 3.4: Simulation model geometry containing cylindrical structure to model the fluid-structure interaction (FSI) near the free surface for comparison of simulations with experiment

3.4.1 Computational domain and boundary conditions

The diameter of the cylindrical structure in the simulation model is represented by D. Numerical tank has a length of 10 D upstream, a length of 30 D downstream, and a width of 10 D. The simulation's wall boundary conditions, which include the body, are impregnability and no-slip, having a constant circulation in the horizontal direction determining the initial velocity. The required *Re* is attained by varying the flow velocity. The pressure outlet is handled as the flow exit. The simulations are done for two Reynold number Re=3900 and Re=10000. Input parameters to achieve these two Reynolds numbers are given in Table 3.7. The calculations for Both Reynolds number (*Re*) are given in Appendix D and E.

Table 3.7: Parameters used in scenario 3

Diameter (m)	Density (Kg/m^3)	Viscosity (Kg/ms)	Reynolds Number	Velocity (m/s)
1	998	0.001	3900	0.003908
1	998	0.001	10000	0.01

3.4.2 **Meshing**

In the simulations, a structured quadrilateral mesh is used. The structured mesh was generated by using ANSYS Mesh generator. ANSYS Fluent is used to import the mesh. Around the cylinder, there are 400 elements, and along the side of the neighbouring square space, there are 80 elements. The mesh in the computational domain is shown in Figure 3.5.

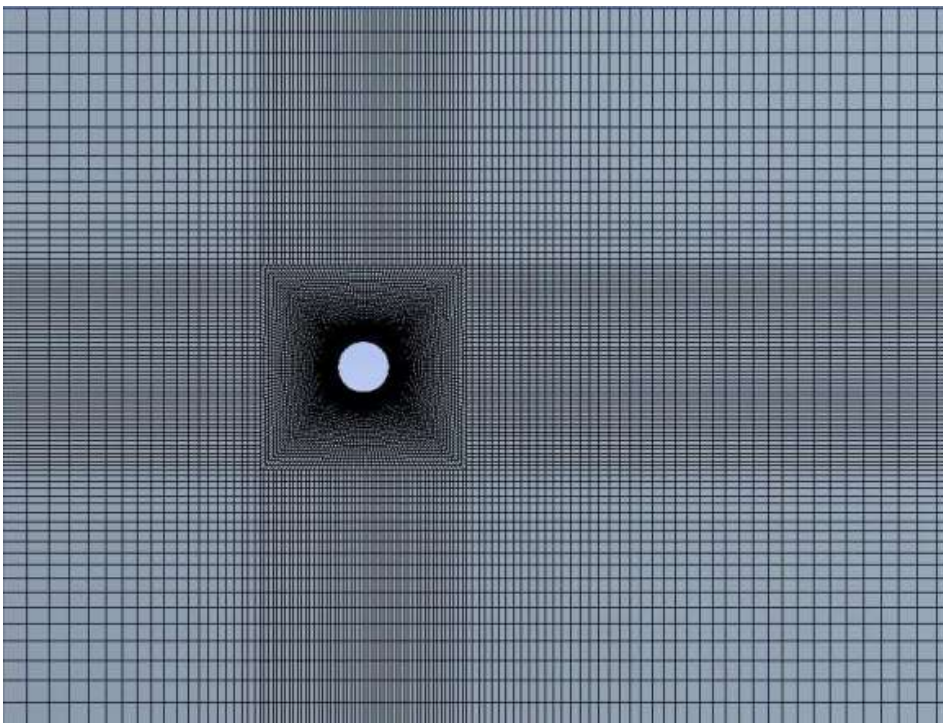

Figure 3.5: The structure mesh generated around the circular cylinder for modelling fluid-structure interaction

3.4.3 **Simulation settings**

The numerical solution for this flow was found using the ANSYS Fluent 18.1 commercial CFD tool. The finite volume method is used to discretize the problem. The solution settings as suggested by ANSYS Fluent (2013) for flow problems related to circular cylinder are summarized in Table 3.8.

Table 3.8: Simulation set-up for flow around circular cylinder recommended by ANSYS Fluent (2013)

Model Set-up	***Reynolds number less than 50***	***Reynolds number 50-1000***	***Reynolds number 1000-20000***
Flow Condition	Steady	Unsteady	Unsteady
Solver	Double precision	Double precision	Double precision
Turbulence Model	Laminar	Laminar, k-ε	k-ε, k-ω and SST
Pressure	Standard	Standard	Standard
Pressure-velocity coupling	SIMPLE	SIMPLE	SIMPLE
Momentum	Second order	Second order	Second order
Upstream	Velocity inlet	Velocity inlet	Velocity inlet
Downstream	Pressure outlet	Pressure outlet	Pressure outlet
Top boundary	Symmetry	Symmetry	Symmetry
Bottom boundary	Symmetry	Symmetry	Symmetry
Cylinder	No slip	No slip	No slip

There are several options for meshing the solution domain, including a gradient scheme based on cell or node and least square scheme based on cell or node. The least-square approach based on node or cell is more accurate than gradient scheme based on cell or node. It consumes less processing time as compared to gradient scheme so least square scheme based on cell is default scheme. Convergence happens in this simulation when the cumulative residual of all of the preceding equations is less than 10^{-5}.

3.4.4 Grid and time convergence study

The first two simulations were carried out for grid and time step convergence to check dependency of numerical results on grid and time step size. For grid convergence study, four different grid resolution of the mesh was generated to determine the most suitable mesh resolution. The details of the mesh grid resolution used in this scenario are given in Table 3.9.

Table 3.9: Size of mesh elements used in the grid convergence test for flow in a tank with a circular structure

Mesh	Elements
A (Coarse)	60319
B (Medium)	120340
C (Fine)	413219
D (Extra Fine)	832103

3.5 Scenario 4: Flow in a tank with rectangular structure

Rolf Jarle (2001) conducted a physical model testing in the laboratory Norwegian university of science and technology (NTNU). The geometry of the numerical model is kept same dimensions as used in the physical model. A numerical block in rectangle shape with 0.63 m length and 0.30 m width is used to represent the platform deck. The water tank is 2m high where water level is kept at 1 m to keep larger air domain for holding the waves and the block without requiring the generation of too many cells. A mesh dependency test was performed prior to the final simulations. The fluid domain's wave flume length is kept at 13.5 m, where deck is placed in the mid of the tank to

reduce the wave disturbance. The essential dimensions of the 2D geometry are shown in Figure 3.6.

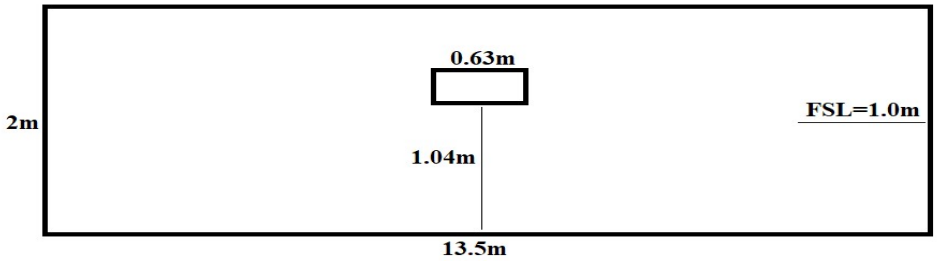

Figure 3.6: The geometry of the numerical wave tank with the rectangular structure acting as deck for offshore platform to study wave in deck loads near the free surface

3.5.1 Experimental setup

A 13.5 m long narrow wave basin in the NTNU laboratory is used for the experiment by Rolf Jarle (2001). It is 1.5 m deep and 0.6 m wide whereas the depth of water is kept as 1.0 m. During the trial stage, the height and period of the wave along with the distance between deck and water (deck clearance) is varied. At one end of the flume, an electrically driven wave maker is installed while wave beach is placed on the other end of the tank. The wave maker is controlled by computer to generate the desirable waves in the wave basin. The height of the flap to generate ocean waves in the wave tank is kept 0.1 m above the surface of wave basin. The purpose of the beach in the wave basin is to eliminate the damping effect caused by wave reflection in the tank. With a parabolic arc profile, this is a traditional form of beach. The model had to encompass the entire width of the basin because of the two-dimensional flow. A small membrane made of rubber is installed between walls of the basin and model to prevent water from entering through the deck. The walls were

supposed to be unaffected by this membrane's vertical force. The impact event is quantified by using vertical force transducers in the deck. The deck is built as a rigid body to eliminate the structural responses.

A wave with wave periods of 1.11, 1.25 and 1.43 seconds is used in the experiments. The wave parameters were selected to replicate full scale ocean conditions in the experimental tank. These waves also reduced the probability of generating undesired waves in the tank. The force transducers were positioned on the bottom side of the deck model, which is 0.63 meter long and 0.56 meter wide. The model is scaled to 1:150 so the total length of the platform is 94.5 meter in full scale. The regular incident waves were used in the experiment because they were easier to generate, and the physics related to the impact of these waves to offshore structures is not much complex in nature. Once the regular waves are validated, the idea could be implemented to more complex ocean scenarios involving any sea state. The height of the waves generated in the wave basin ranged from 0.10 meter to 0.14 meter which represented the full-scale wave heights of 15-22.5 meter. When the steepness of the wave becomes too great, it becomes difficult to generate a time series of regular waves because breaking may occur.

3.5.2 **Mesh**

A mesh must be generated onto the appropriate geometry before any computations can be performed. It is the first phase in this scenario when the CFD engineer can impact the quality and accuracy of solution. The automatic ANSYS Mesh generator tool is used to discretise the computational domain.

This tool can generate any kind of mesh from quadrilateral to hexahedral mesh. A quadrilateral mesh is generated by using facial meshing technique. A quadrilateral mesh provides a simple geometric framework for precisely describing the position and slope of the water surface. On unstructured meshes, smearing the surface to characterise the free surface position is frequently required. It causes a spongy surface which reduces the total pressure acting on that surface for impact period during the simulation. The unrefined mesh can be refined using the "adopt-region" command in ANSYS. The mesh refinement is often needed for crucial regions of computational domain like free surface area where waves are generated or spots closer to model geometry. This mesh refinement feature divides an element of selected mesh into 4 further elements. These four new elements are known as hanging nodes which are not in connection with the nearby nodes. The node values of newly constructed elements are interpolated. Simulations were run on four distinct meshes as part of a mesh dependency investigation.

3.5.3 **Initial and Boundary Conditions**

Fluent comes includes a transient and pressure-based solver out of the box. It is possible to enable double precision, which is recommended for multi-phase flow. With implicit body force formulation and interfacial anti-diffusion option enabled, volume fraction parameters are configured to be implicit. For open channel flow problems, the default value is implicit, allowing for greater time step sizes. In the negative y-direction, gravity is triggered. The turbulence is described using a viscous model. For this objective, the realisable k-model and Enhanced Wall Treatment were used.

For multiphase fluid modelling, air and water are utilised as primary and secondary materials. Both materials' attributes are chosen from a fluent database. The operational density is determined by the density of the lighter phase material. It improves momentum balance and eliminates the possibility of lighter phase material hydrostatic pressure build-up. During multiphase modelling of fluid phases, a reference pressure location of fluid containing 100 percent of any material (water or air) is always selected. If no location contains 100 percent of any of fluid material, then a location is chosen for multiphase modelling where pressure does not vary with time. A stable pressure location helps in converging the solution and speed up the simulation processing. It also causes minimum round off errors in processing of pressure equations. A bigger change in static pressure is observed in denser fluid as compared to lighter fluid under constant velocity distribution. Due to this, position should be chosen in a light phase fluid. It is convenient to choose position of reference pressure in the upper left corner of completely filled air.

The inlet border is configured to be a velocity inlet with zero average velocity to exclude the effect of natural turbulences like current or wind affecting the deck. If the turbulence model is enabled, Fluent requires turbulence quantities to be assigned at the inlet of the tank before fluid entry. It further requires the values of turbulence constants like intensity of turbulence, ratio of viscosity, value of k and ε and many more quantities by assuming their values if value of any of the constant term is missing. Because

the flow in this project was assumed to be laminar, the turbulence intensity was fixed at velocity inlet.

Fifth order Stokes waves with a wave height of 0.1 m and a wavelength of 1.92 m, as employed in one of the related cases from the reference experiment, were chosen as the wave theory for this simulation. Stokes waves are nonlinear in nature unlike airy waves. They occur in intermediate to deep water due to their finite wave amplitude. On the other hand, the linear airy waves are small amplitude waves, so they are shallow water waves. It is very important to determine the breaking limit of wave and water depth of water before choosing a proper wave theory. Water depth also helps to assess the steepness of wave and relative depth. The steepness of a wave is defined as the ration of 86 height of the wave, H, to the wavelength, λ. Relative depth is defined as the ratio between depth of water, d and height of the wave, H.

Table 3.10: Wave parameters used in the experimental study of Rolf Jarle (2001)

Case	**T (s)**	**H (m)**	**λ (m)**	**d (m)**	**H/d**	**H/ λ**	**d/ λ**
1	1.11	0.1	1.92	1.0	0.1	0.052	0.52
2	1.25	0.10	2.41	1.0	0.1	0.041	0.41
3	1.25	0.12	2.41	1.0	0.12	0.050	0.41
Deep Water requirement		H/d <0.55		H/λ <0.1		d/λ > 0.5	

Table 3.10 displays a few guideline values and ratios from Rolf Jarle (2001) experimental investigation, concluding that only the wave parameters of Case 1 are in the deep-water range. In this instance, the parameters from

Case 1 are employed. This limit in water depth had no effect on the waves, according to the measurements. The level of air-gap in full-scale is 6 meter which is set 0.04 meter in the numerical model. The height of the wave in full scale ranges from 15 to 18 meter with wavelengths between 287 and 362 meter.

The downstream border is set to pressure outlet, where backward flow direction is normal to boundary. The neighbouring cell technique is applied for interpolation of density. The volume fraction derived from the surrounding cell is then utilised to interpolate the density used in the hydrostatic profile. The values of nearby cells are used in Fluent software for calculating volume fraction automatically. Turbulence parameters and free surface level must be supplied again at the outlet border. The outlets of the numerical models must have single outer boundary so splitting mode is prohibited in the open channel modelling.

The platform and the domain's bottom are simulated as wall having no-slip condition, whereas the top border of the domain is designated as a symmetry. The reason for this is to keep the air from forming an unwanted boundary layer.

3.5.4 **Solver Settings**

The momentum and turbulent kinetic energy are discretized using the second-order upwind method, while the dissipation rate is discretized using the first-

order upwind strategy. The default gradient scheme in ANSYS is least square scheme based on cell which is used in this simulation. In VOF multiphase simulations, ANSYS suggests using "PRESTO!" for pressure interpolation and "Compressive" for the volume fraction. Because there were problems with convergence when the transient formulation was changed to second order, it is now set to "First Order Implicit." Despite the fact that ANSYS advises PISO with non-iterative time advancement (NITA), the 2D simulation in this project is done using the Coupled method. The basis for this decision is because PISO appeared to have higher x-momentum divergence than the Coupled scheme.

The simulation is started using the Hybrid initialization approach and "computing from Inlet boundary." A wavy surface is used as starting condition, because it results matured waves in the wave basin. The size of block is kept small so only two wave crests cover the wave basin. This method of modelling saves a significant amount of computer time while also ensuring that no border reflections occur near the deck by disturbed waves.

The size and number of time step is determined before starting the simulation. It is also important to select iterations per time step. The number of time steps is set to 50000 and the size of each time step is chosen as 0.001 seconds. To capture the complete wave event hitting the deck, the time of simulation is kept as 50 seconds. During these 50 seconds, the waves are generated in the tank and impact event are counted from initial wave to final wave.

3.6 Summary

This chapter begins with a short introduction and reasoning why CFD software ANSYS Fluent was used in this study. The methodology of four modelling scenarios to model the metocean interaction behaviour model around offshore structures to achieve the selected objective of the study is described in detail. The first two modelling scenarios are utilised for developing a simulation model to generate the metocean parameters. The last two modelling scenarios involve the introduction of offshore structure in a numerical wave tank to study the metocean interaction behaviour around offshore structure near the free surface.

CHAPTER 4

RESULTS AND DISCUSSION

Main achievements of this research have been presented and discussed in this chapter. Initially, the section focuses on the grid test results obtained from numerical wave tanks including the flat bottom numerical tank (verification tank), submerged bar bottom numerical tank (validation tank), tank with the cylindrical structure for fluid-structure interaction (FSI tank) and tank with rectangular structure for wave-structure interaction (WSI tank). Finally, the numerical results obtained using the best grid resolution are used for further analysis where free surface elevation wave profiles of the verification tank are compared with the ideal wave parameters obtained using stokes second-order wave. The numerical results of the validation, FSI and WSI tank are compared with the reference experiments.

4.1 Flow over a rectangular tank

Flow in a rectangular tank is studied to generate the regular waves in a wave tank for the verification of the numerical model. An overview of stokes second-order waves developed im the 2-D rectangular wave basin is given in Figure 4.1 where red colour indicates the water and blue colour indicates air. The distance of the wave tank is given in meter where x is the horizontal distance and z is the height of the tank.

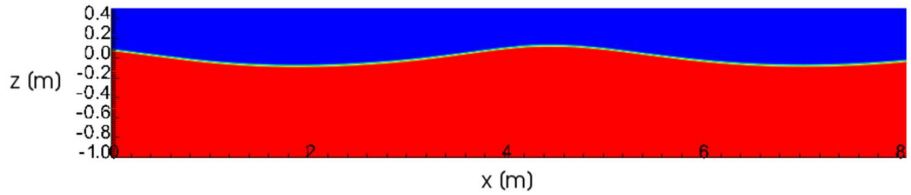

Figure 4.1: Simulation waves generation in a rectangular wave tank using stokes second-order wave theory

4.1.1 Meshing convergence

Simulations uses mesh of four different grid resolutions to determine the convergence criteria of mesh. Stokes second-order wave with wave height of 0.1 meter and wavelength of 5 meter is used for the grid convergence test of the rectangular numerical wave tank. The depth of water is kept 1 meter. Meshing results of first four gauges are given from Figure 4.2 to Figure 4.5. The details of the wave parameters used in the flat-bottom numerical wave tank are given in section 3.2.6.

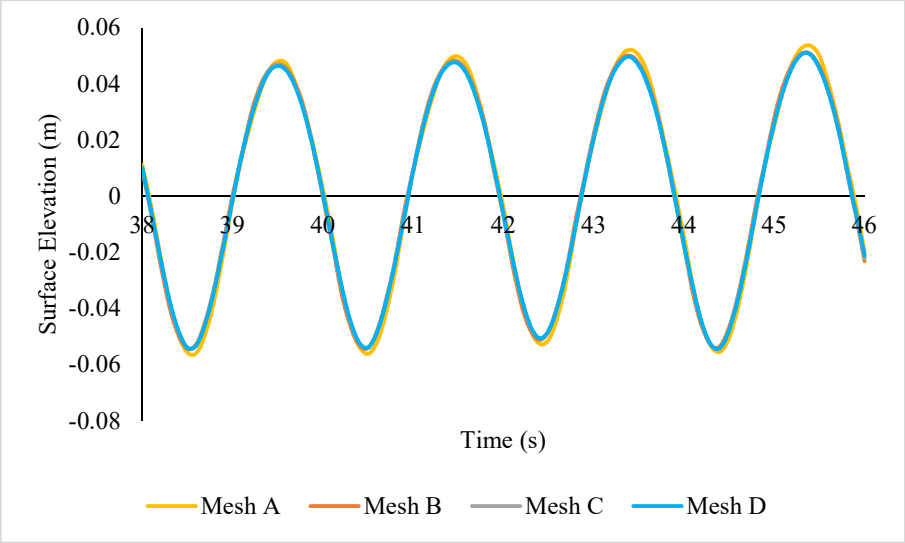

Figure 4.2: Grid dependency test results of gauge 1 located at 2 m on the horizontal x-axis for a rectangular wave tank.

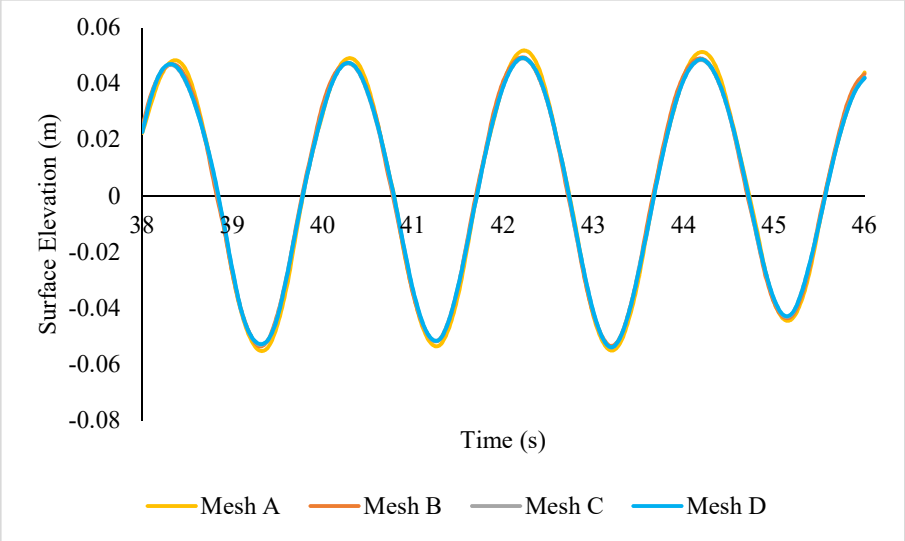

Figure 4.3: Grid dependency test results of the gauge 2 located at 4 m on the horizontal x-axis for a rectangular wave tank.

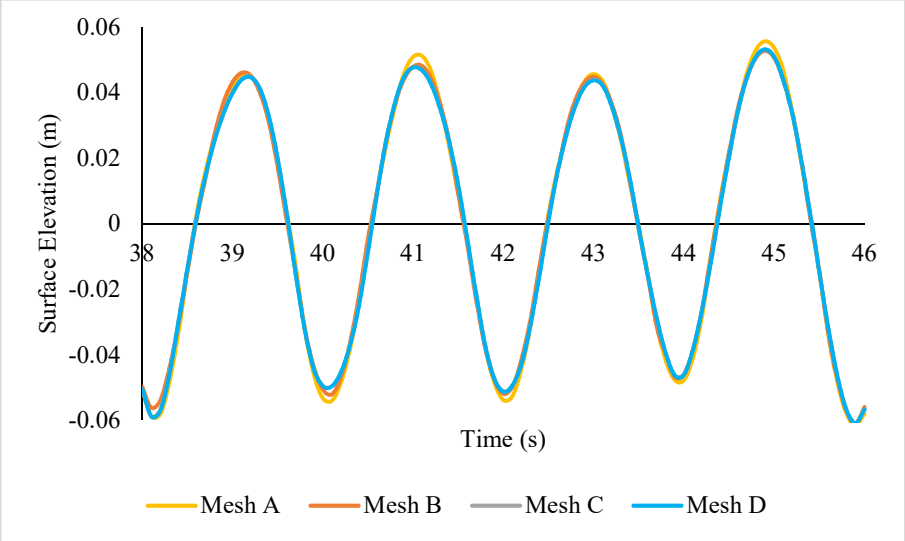

Figure 4.4: Grid dependency test results of the gauge 3 located at 6 m on the horizontal x-axis for a rectangular wave tank.

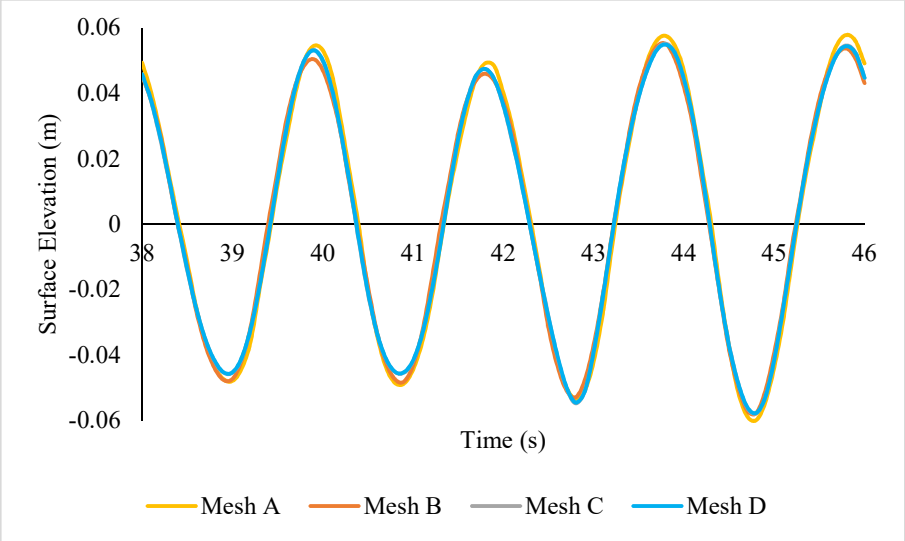

Figure 4.5: Grid dependency test results of the gauge 4 located at 8 m on the horizontal x-axis for a rectangular wave tank.

Simulation results show a very minor changes for mesh C and mesh D while the difference is visible for results of mesh A and mesh B. The performance of mesh A is so weak because of its low mesh resolution which contains only 8325 elements. Mesh performance increases with the increase of grid elements. Free surface profiles of the waves generated in the wave tank becomes stable when mesh elements reach to 300000. Differences in the wave profile are not much distinct after this mesh resolution. Due to this reason, mesh C is chosen for further simulations. It is important to note that the Courant ~~courant~~ number was controlled below 2 to achieve the converged result.

4.1.2 Comparison of ideal wave profile with simulation

The free surface elevation simulation result was compared with Stokes second order wave theory using Eq. (3.7) as given in section 3.2.4. The comparison

was done after 30 seconds of wave generation to confirm that the wave generation had fully matured. Figures 4.6 through 4.10 illustrate the results of the comparison at four distinct times. The free surface profiles results indicate that there is no change in phase between simulation and theoretical results.

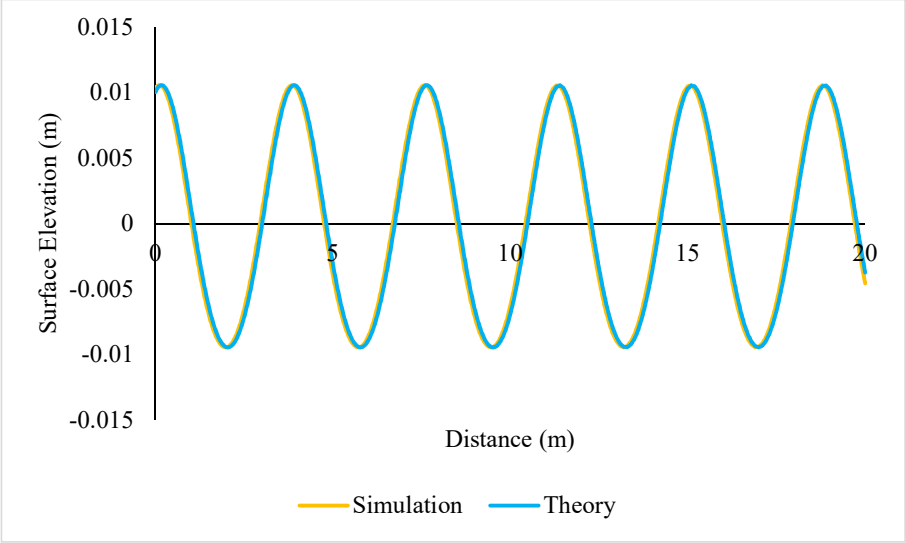

Figure 4.6: Comparison of simulation results with ideal wave profile for a flow time of 35 seconds.

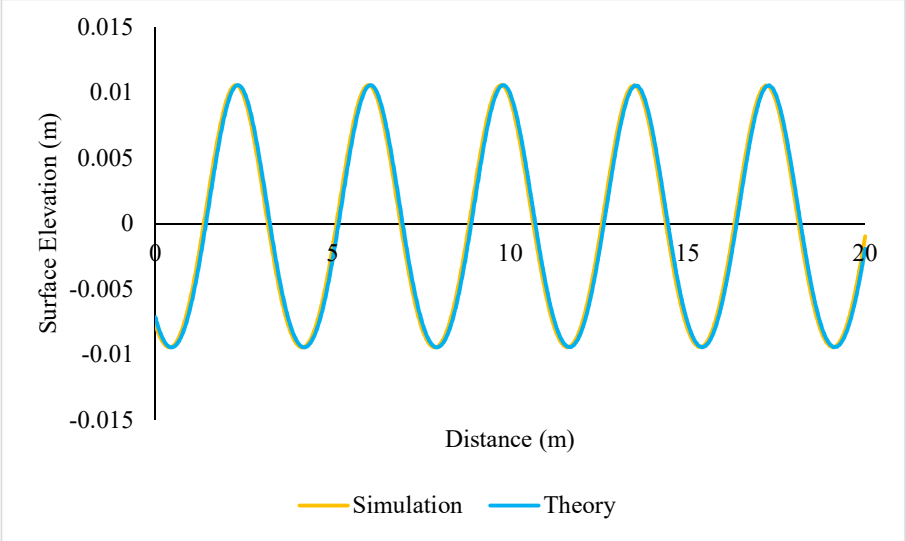

Figure 4.7: Comparison of simulation results with ideal wave profile for a flow time of 40 seconds.

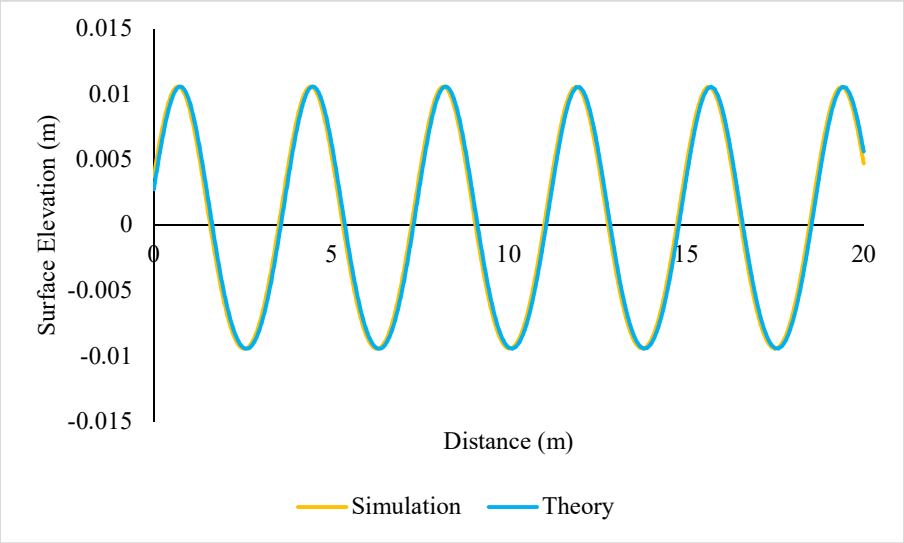

Figure 4.8: Comparison of simulation results with ideal wave profile for a flow time of 45 seconds.

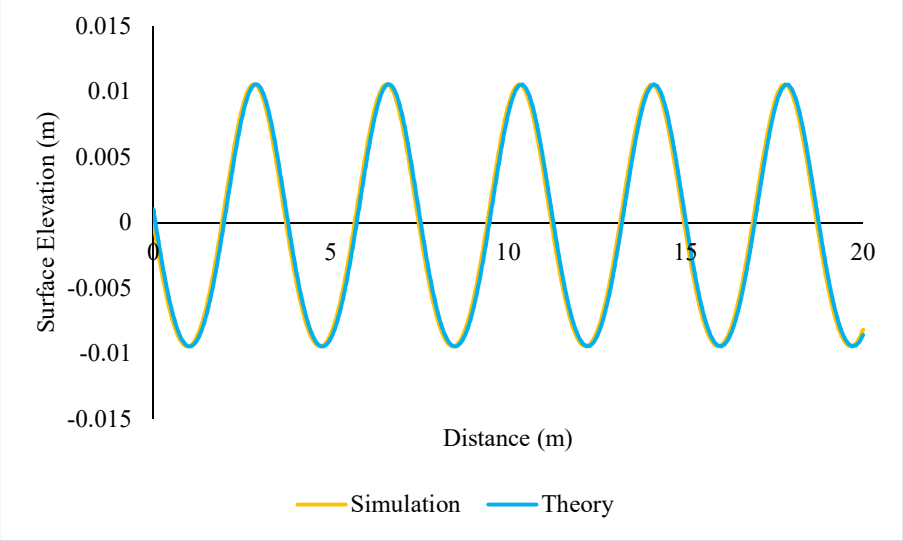

Figure 4.9: Comparison of simulation results with ideal wave profile for a flow time of 50 seconds.

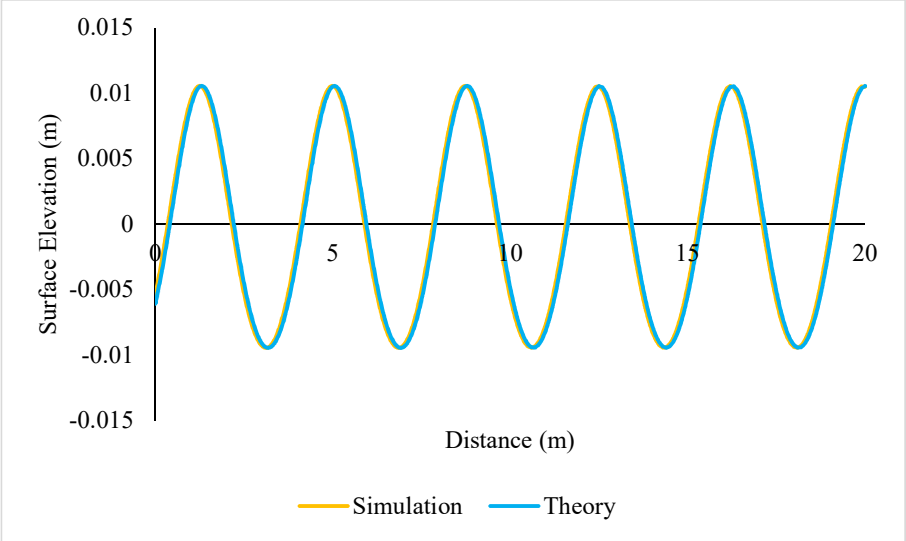

Figure 4.10: Comparison of simulation results with ideal wave profile for a flow time of 55 seconds.

Table 4.1 compares observed/simulation findings to ideal/theoretical results statistically for a horizontal distance of 12 m from the inlet of the wave tank. Errors are calculated for this point because it is in the middle of the tank and represents the tank as whole. The root mean square error (RMSE) is calculated using Eq. 3.7 from section 3.2.2. The Root Mean Square Error (RMSE) is utilised as a comparison index because it calculates the difference in error between two data sets. The closer the predicted and observed values are, the less the root mean square error (RMSE). The RMSE score of 0.5 reflects the model's ability to forecast data effectively. RMSE values above 0.5 reflects weak performance of the model and vice versa. The obtained RMSE values are excellent for selected flow times.

Table 4.1: The Root Mean Square Error (RMSE) calculated at x=12 m in the verification tank

Time (s)	RMSE
35	0.000732
40	0.000711
45	0.000818
55	0.000758

4.2 Flow over a submerged bar

The designer of numerical wave tank rarely conduct the experiments and they mostly rely on the existing data of experimental studies. The experiments of Beji & Battjes (1993), Dingemans (1994) and Ohyama, Kioka & Tada (1995) are most commonly referenced in free surface flow studies. The study of Dingemans (1994) is the most referenced classical set of experimental study. To validate the simulation results, free surface wave profiles obtained using the numerical tank as shown in Figure 4.11 are compared with the experimental work of Dingemans (1994) for verification purpose.

Figure 4.11: Full-scale view of numerical wave tank with submerged bar for comparison of CFD wave profile with the experimental study of Dingemans (1994) **.**

4.2.1 Meshing results

The meshing results for the tank with submerged bar are presented from Figure 4.12 to Figure 4.22. The mesh independent ~~independence~~ result for the first three gauges shows no or a little deviation in the results. The free surface wave elevation profile for gauge 1 to 3 is identical in all the meshes except

mesh A due to its low mesh resolution. For all these three wave gauges mesh ~~Mesh~~ B, C and D show no difference in the wave profile. The wave profile starts to deviate from gauge 4 and onwards due to the presence of the bar at the bottom of the tank. From gauge 5 to gauge 11, this deviation is quite visible. A reduction in the surface elevation of mesh A and B is visible after gauge 5 which is severe for gauge 9 where simulated free surface elevation of the mesh A shows a complete deviation with the simulated results of other meshes.

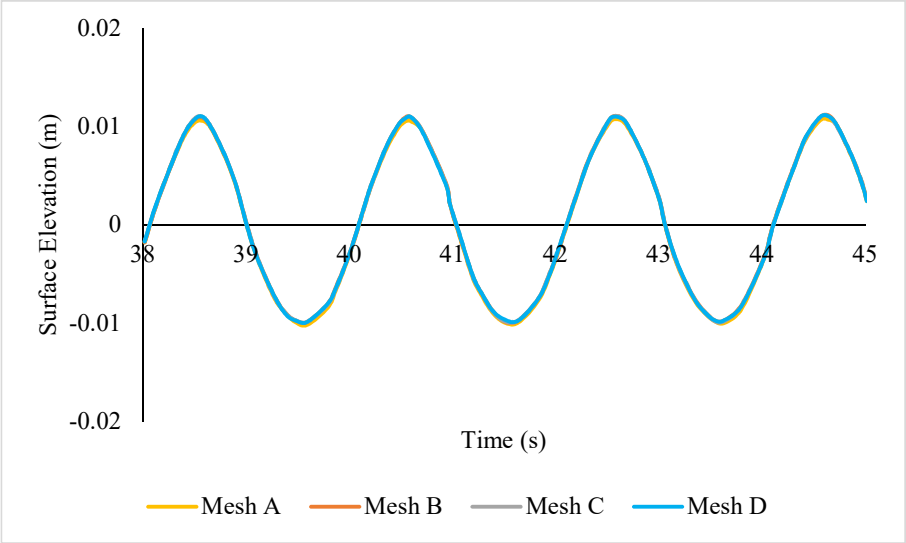

Figure 4.12: Grid dependency test results of the gauge 1 located at 2 m on the horizontal x-axis for wave tank with submerged bar.

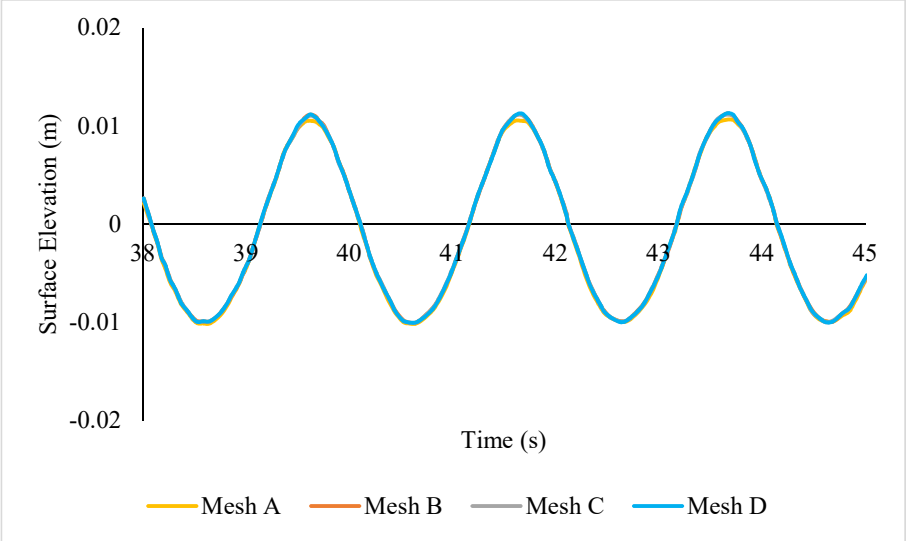

Figure 4.13: Grid dependency test results of the gauge 2 located at 4 m on the horizontal x-axis for wave tank with submerged bar.

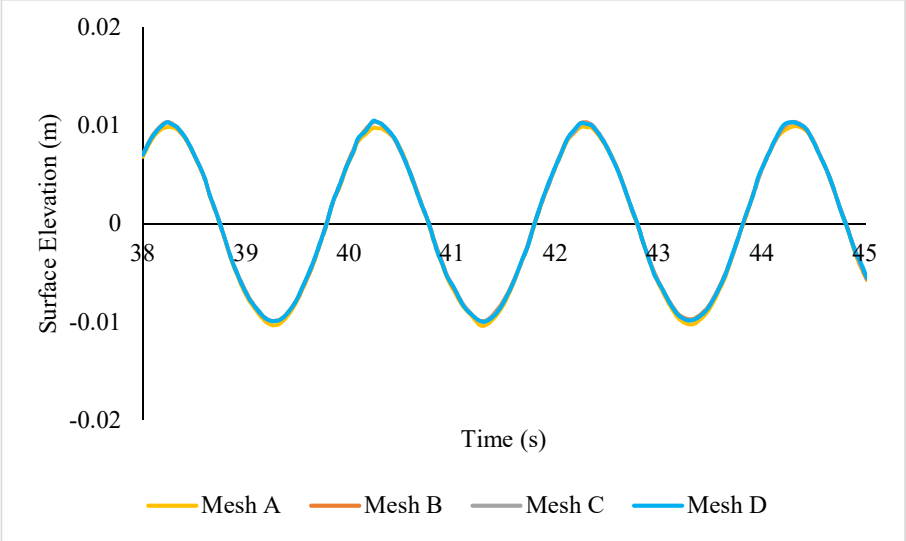

Figure 4.14: Grid dependency test results of the gauge 3 located at 5.7 m on the horizontal x-axis for wave tank with submerged bar.

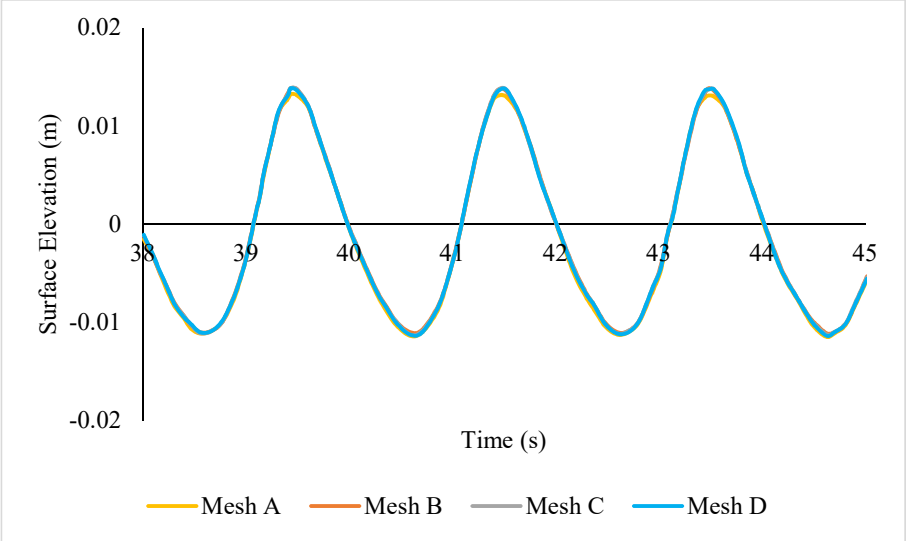

Figure 4.15: Grid dependency test results of the gauge 4 located at 10.5 m on the horizontal x-axis for wave tank with submerged bar.

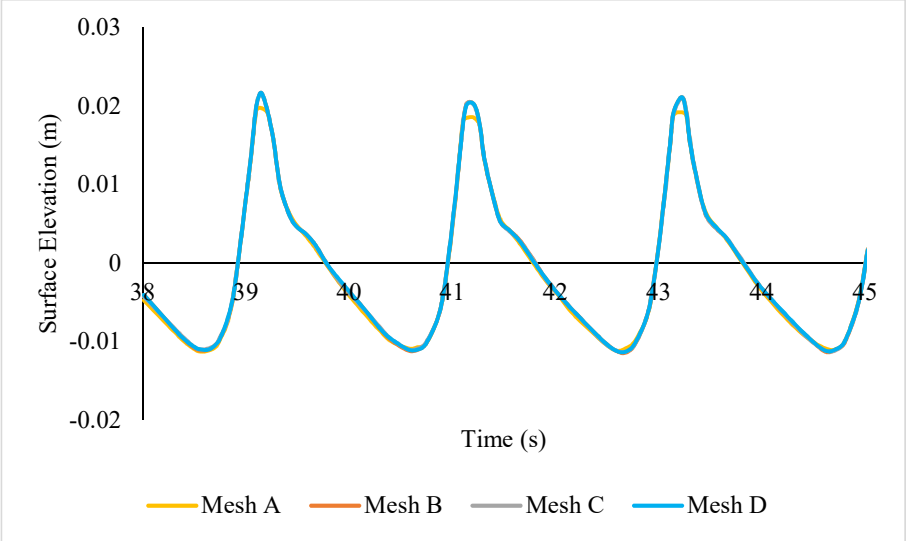

Figure 4.16: Grid dependency test results of the gauge 5 located at 12.5 m on the horizontal x-axis for wave tank with submerged bar.

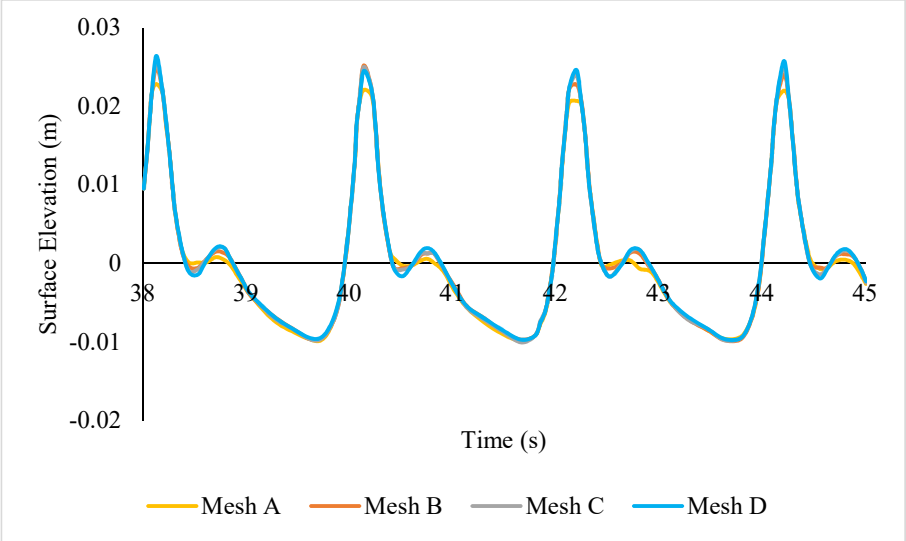

Figure 4.17: Grid dependency test results of the gauge 6 located at 13.5 m on the horizontal x-axis for wave tank with submerged bar.

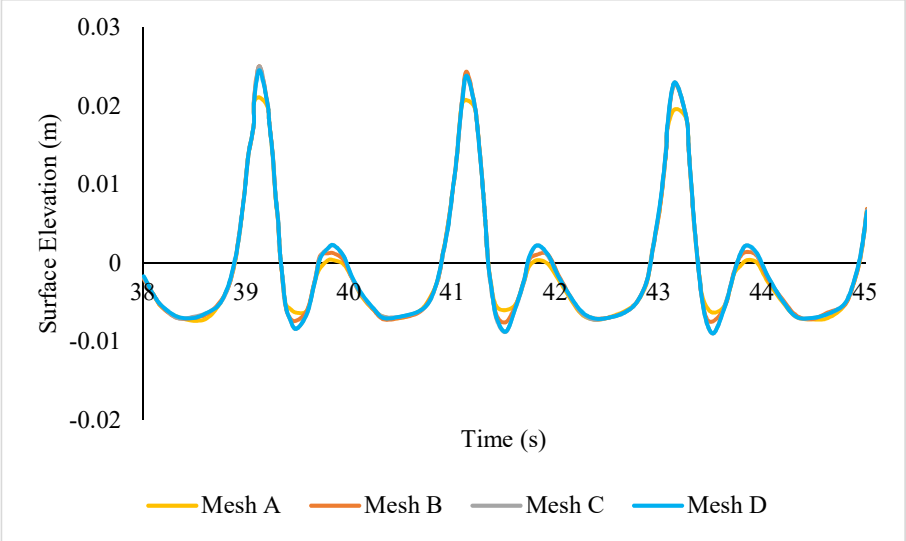

Figure 4.18: Grid dependency test results of the gauge 7 located at 14.5 m on the horizontal x-axis for wave tank with submerged bar.

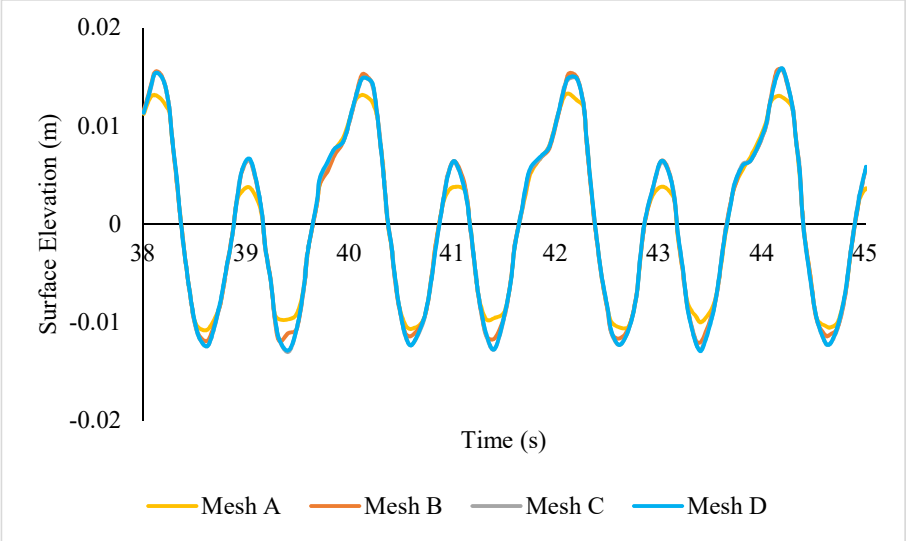

Figure 4.19: Grid dependency test results of the gauge 8 located at 15.7 m on the horizontal x-axis for wave tank with submerged bar.

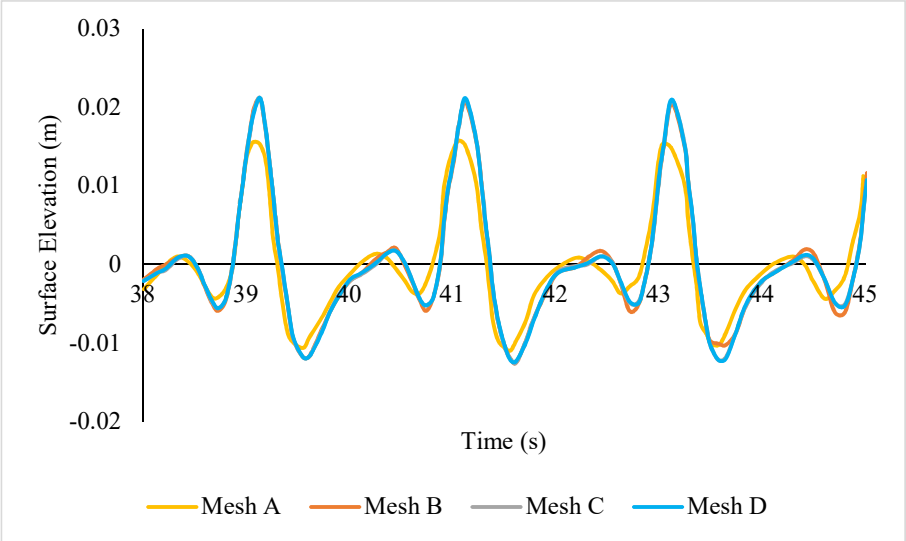

Figure 4.20: Grid dependency test results of the gauge 9 located at 17.3 m on the horizontal x-axis for wave tank with submerged bar.

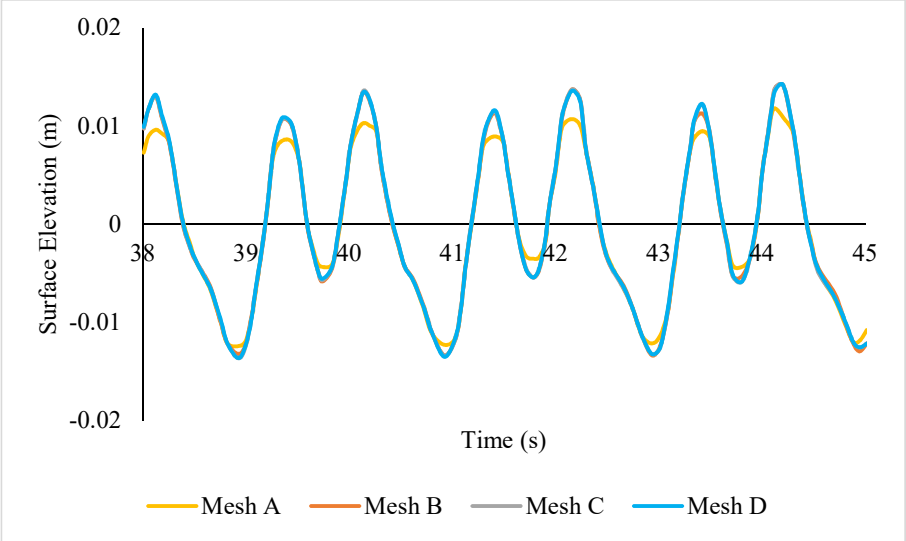

Figure 4.21: Grid dependency test results of the gauge 10 located at 19 m on the horizontal x-axis for wave tank with submerged bar.

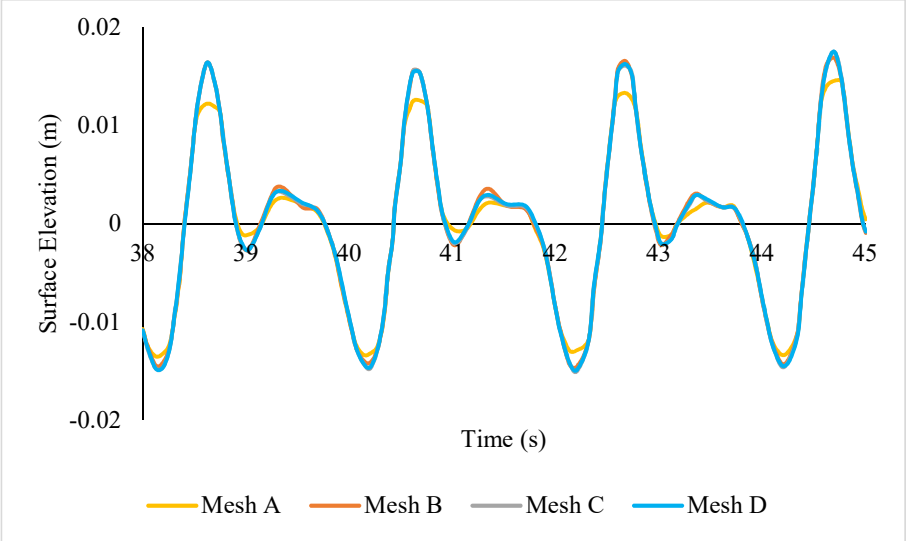

Figure 4.22: Grid dependency test results of the gauge 11 located at 21 m on the horizontal x-axis for wave tank with submerged bar.

It is evident from the meshing results that mesh ~~Mesh~~ C shows no or little deviation as compared to other meshes and it is quicker to generate so it is chosen for the comparison of simulation results with the experimental results.

4.2.2 **Comparison of experimental wave profile with simulations**

The results obtained from the simulations are compared with the experimental results of the Dingemans (1994). The comparison results for all the wave gauges are given from Figure 4.23 to Figure 4.33.

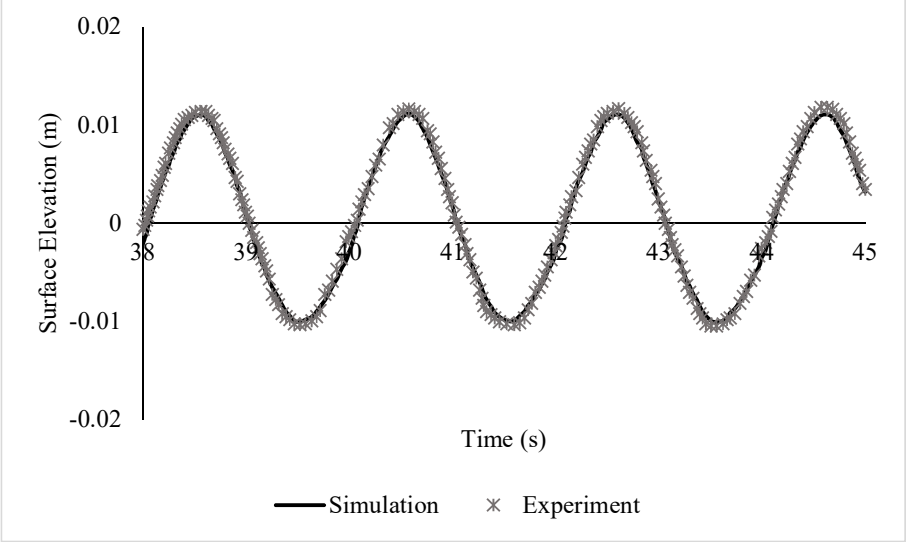

Figure 4.23: Simulation and experimental data comparison for elevation of the waves at gauge 1.

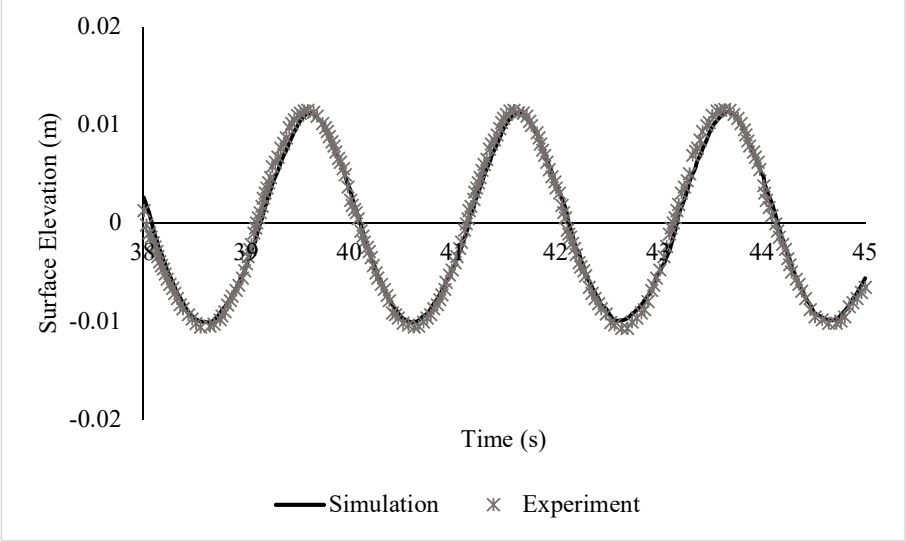

Figure 4.24: Simulation and experimental data comparison for elevation of the waves at gauge 2.

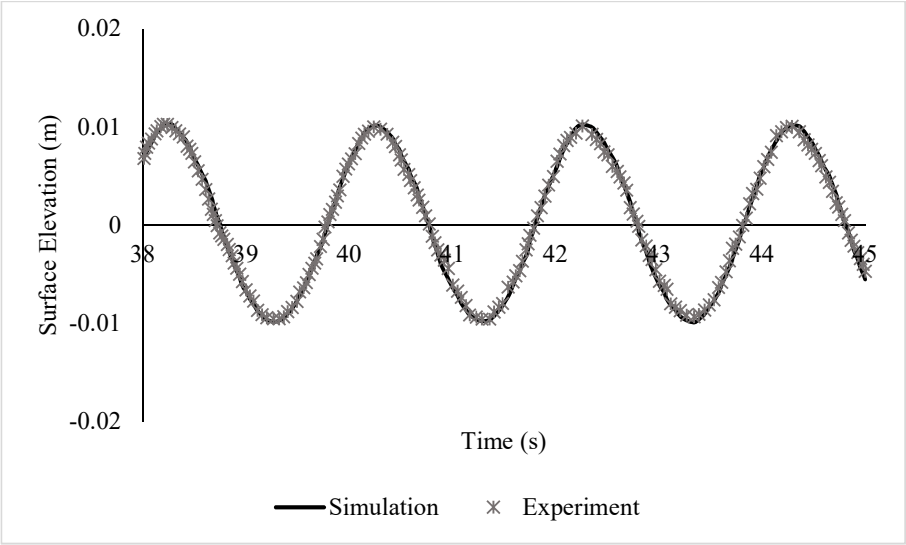

Figure 4.25: Simulation and experimental data comparison for elevation of the waves at gauge 3.

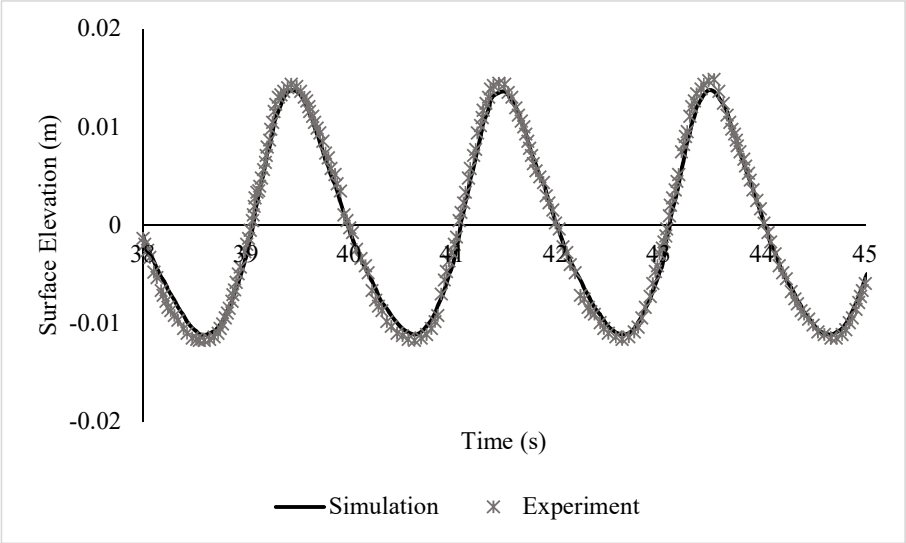

Figure 4.26: Simulation and experimental data comparison for elevation of the waves at gauge 4.

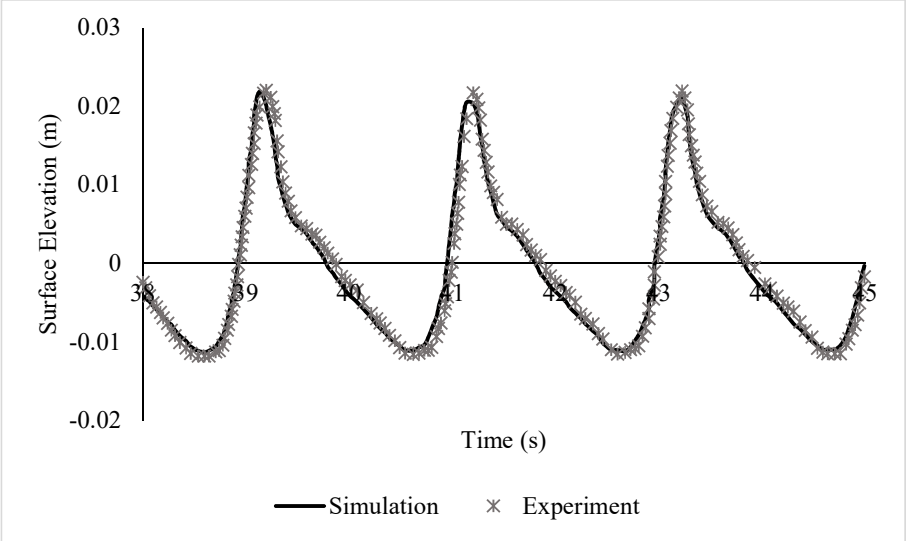

Figure 4.27: Simulation and experimental data comparison for elevation of the waves at gauge 5.

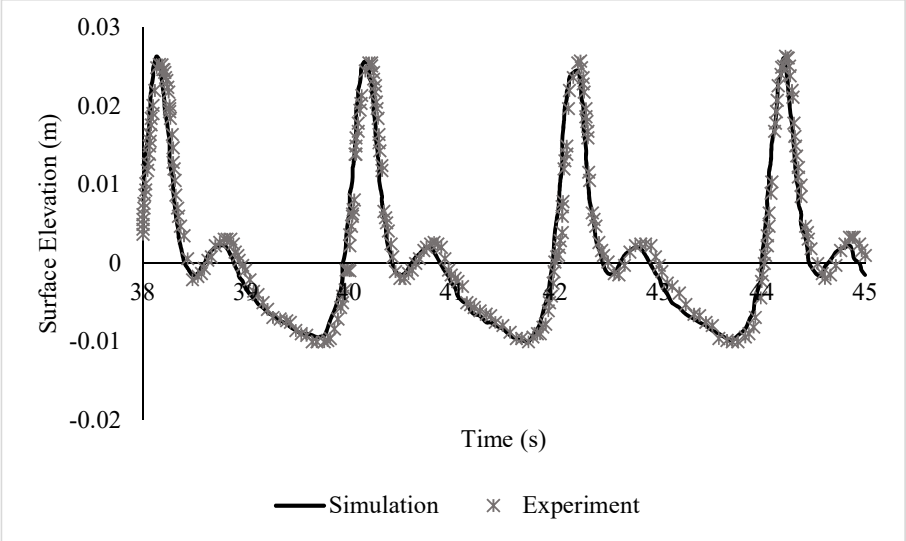

Figure 4.28: Simulation and experimental data comparison for elevation of the waves at gauge 6.

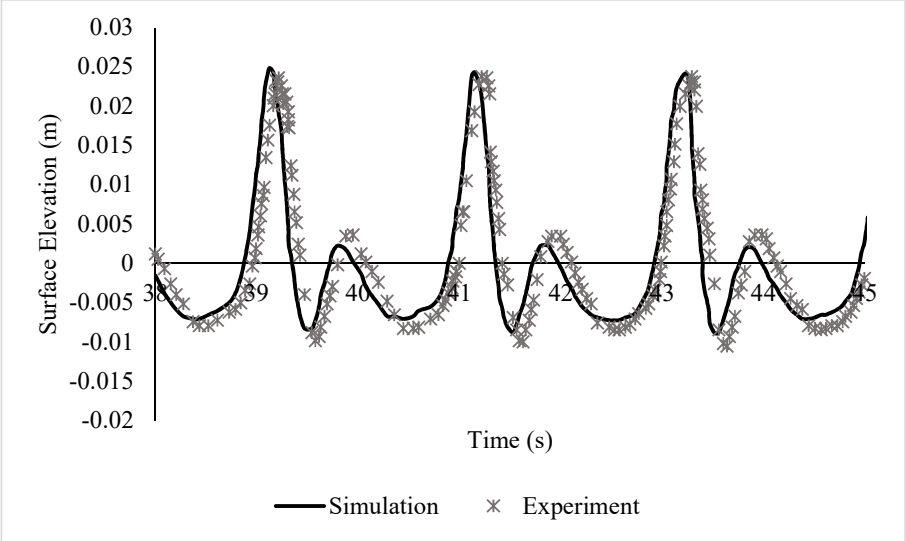

Figure 4.29: Simulation and experimental data comparison for elevation of the waves at gauge 7.

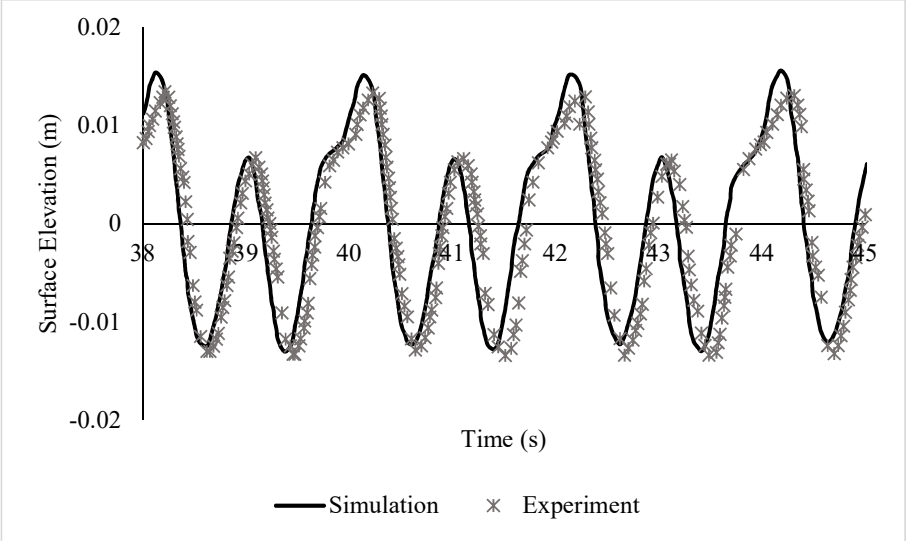

Figure 4.30: Simulation and experimental data comparison for elevation of the waves at gauge 8.

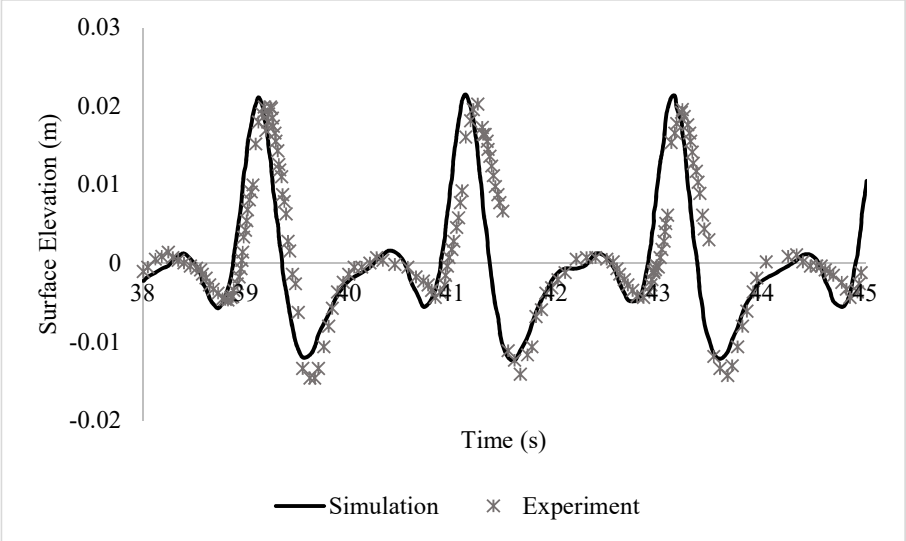

Figure 4.31: Simulation and experimental data comparison for elevation of the waves at gauge 9.

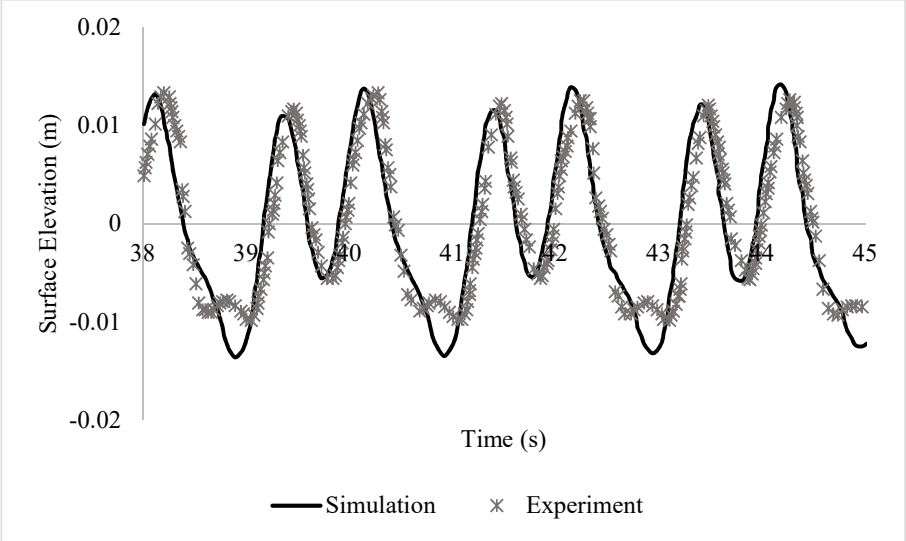

Figure 4.32: Simulation and experimental data comparison for elevation of the waves at gauge 10.

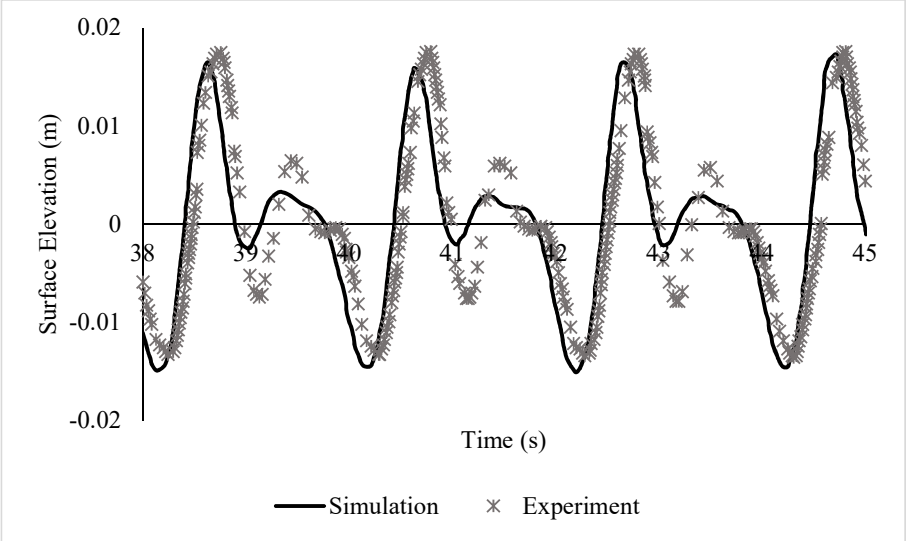

Figure 4.33: Simulation and experimental data comparison for elevation of the waves at gauge 11.

Results of first four gauages (1 to 4) situated before the submerged bar are very close to the experiment. The free surface elevation for these four gauges matches with the free surface elevation obtained by Dingemans (1994). The magnitude of the wave measured at gauge 5 and gauge 6 matches with the experimental results but the secondary crest developing from gauges 5 shows some deviations.

More variations in the result begin to appear for the numerical gauges which are located after the submerged bar (7 to onwards). This change is also reported by authors who used a similar wave tank including Abbasnia & Ghiasi (2014), Kamath et al. (2017), and Gholamipoor & Ghiasi (2021). They further reported that gauges in the similar numerical wave tank after the bar are the most critical gauges in the numerical tank. They also mentioned that the dispersive effect is caused by the submerged bar which become stronger

and stronger by the release of super-harmonics in the tank, so resutls for these specific gauges is hard to regenerate.

Ji et al. (2017) studied the inconsistency between the numerical and experimental results for a numerical wave tank-like Kamath et al. (2017). The point of focus was the location of wave gauges after the bar. They noted that the regular wave profile of the numerical wave tank before the bar is due to the stay of higher harmonics in phase with the primary wave. These higher harmonics generate a free wave when water starts deepen behind the bar. These free wave harmonics are difficult to model in the numerical tank.

A time delay of 0.1 s is observed in the reading of wave gauge 7 which indicates the limitations of the numerical model. This time delay is also noted from gauge 7 to 9 because of inaccurate modelling of the numerical wave speed in the tank. The time delay is observable although, the amplitude of the CFD wave correctly matches to the surface elevation of the experimental result for these wave gauges. Similar behaviour of numerical model is also reported by Kamath et al. (2017) in their studies.

The most significant change of wave profile can be noted in the reading of Gauge number 10 and 11 where difficulty of matching the wave elevation of the numerical and experimental results is observed. This change in matching the wave profile is also due to the time delay.

During the grid convergence test, it was made sure that whether appropriate mesh size improves the results for these wave gauges or not. To determine this, mesh B was additionally refined for the area located after the bar while mesh C was refined overall. The grid convergence test did not indicate any improvement in the results obtained from mesh B. Furthermore, it is evident from the results that changing the dimensions of mesh for a certain region of the numerical wave tank does not guarantee any remarkable improvement of the results so the time delay cannot be attributed to the grid size.

The inconsistency between the experimental and numerical results for the gauges after the submerged bar might be due to the application of the laminar model. A laminar flow was considered due to the assumption that surfaces of the numerical model are smooth. By applying the turbulence model, the roughness can be specified because the turbulence model helps to account for the roughness of the surfaces in the tank.

4.3 Flow in a tank with a cylindrical structure

Flow around a cylindrical structure in a numerical tank was studied for two different Reynolds number (Re). An example of velocity streamlines around a cylinder is shown in Figure 4.34. The study begins with a mesh convergence test to determine the most appropriate mesh size for the numerical model. All the numerical studies mentioned in this section are done for Re=3900 and

Re=1000 under different turbulence models. The obtained data of simulations are compared to available experimental work.

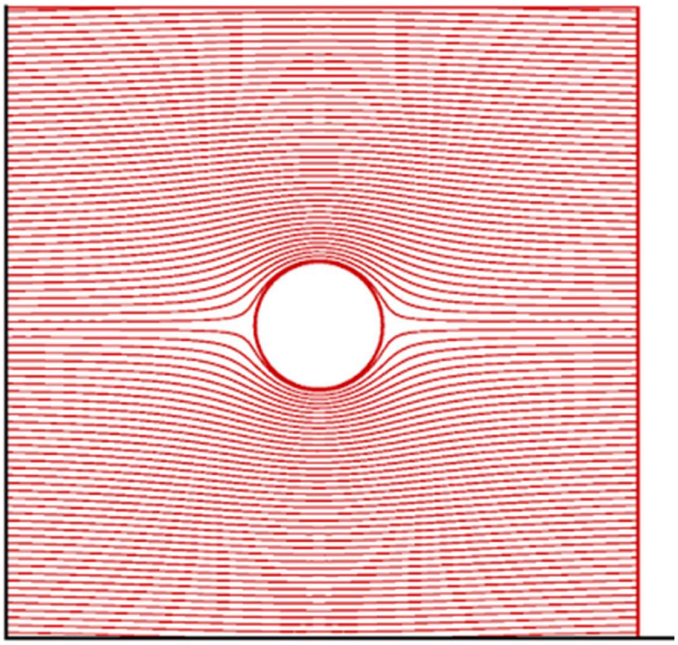

Figure 4.34: Flow around a circular structure in a numerical tank.

4.3.1 Grid convergence results

A gird convergence test is carried out to determine the most appropriate mesh size. This test is also used to check whether simulation results depend on the size of the mesh used during the simulations or not. Four different meshes with the number of elements ranging from 20000 to 560000 are tested for the meshing test. All the simulations are done for two different Reynold number (Re) of 3900 and 10000 with structured mesh. The structured mesh is used due to its simplicity and easy processing. During the grid convergence test, the coefficient values are determined and checked as given in Table 4.2. Under

different grid size, the coefficient of drag (Cd), coefficient of lift (Cl) and coefficient of pressure (Cp) are determined. The turbulence properties were set with Fluent default values and the RKE turbulence model is used for the meshing test.

Table 4.2: Mesh convergence criteria at two Reynolds number using the RKE model.

	Re = 3900			*Re*=10000		
Case	**Mesh Size**	**Cd**	**Cl**	**Mesh size**	**Cd**	**Cl**
A	20300	0.94	0.30	20300	0.87	0.28
B	90800	0.92	0.37	37800	0.86	0.21
C	204800	0.92	0.27	44800	0.86	0.21
D	560010	0.92	0.27	56010	0.86	0.21

Results of drag and lift coefficient at two Reynolds number of 3900 and 10000 for the mesh of four different grid sizes are shown in Figure 4.35. It is evident from the results that the value of these two coefficients changes very slightly when the mesh number exceeds 90000.

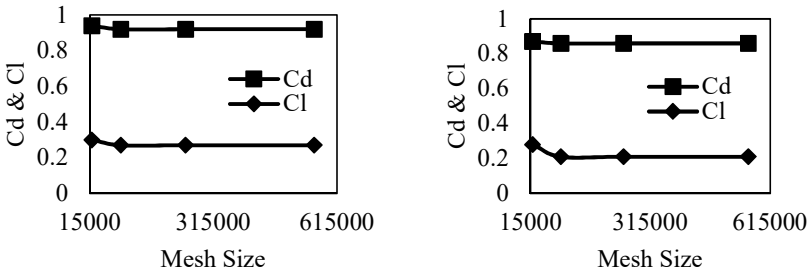

Figure 4.35: Grid convergence test results for value of Drag and lift coefficients at (a) Re= 3900 (b) Re=10000 using RKE model.

The meshing results of the pressure distribution around the circular cylinder as shown in Figure 4.36 also indicates that a small variation of pressure distribution is observed after mesh B. Mesh C is used to carry out future calculations due to its easy generation and quick processing time.

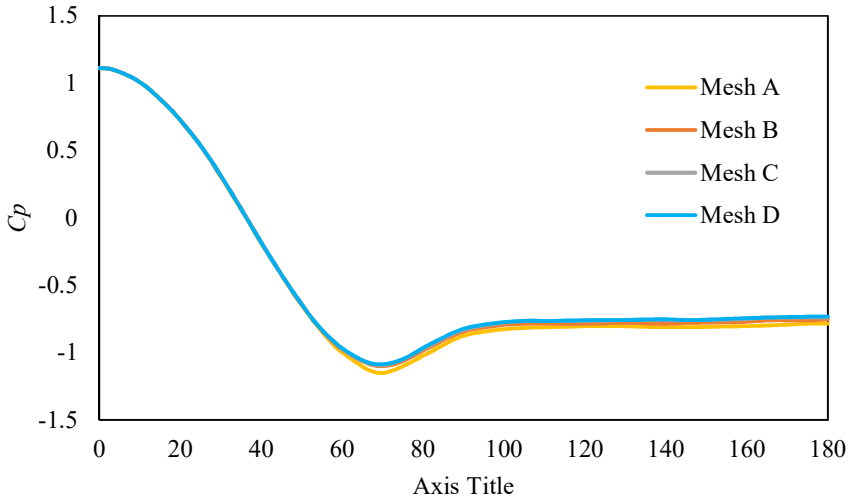

Figure 4.36: Coefficient of Pressure (*Cp*) for different grid resolution at Re=3900 using the RKE model.

4.3.2 Timestep convergence results

A time step convergence test is carried out to determine the most appropriate time step. Courant-Fredrich-Lewy condition is used to determine the most suitable courant number. Four different courant numbers are used to check whether the result of lift and drag coefficient relies on the courant number or not. The simulations are done at Re=3900 and 10000. The obtained result is given in Table 4.2.

Table 4.3: Courant number convergence criteria at two Reynolds number using RKE model

	Re = 3900			*Re*=10000		
Case	**Courant No.**	**Cd**	**Cl**	**Courant No.**	**Cd**	**Cl**
A	32	0.88	0.18	32	0.79	0.12
B	17	0.90	0.21	17	0.81	0.19
C	2	0.92	0.27	2	0.86	0.20
D	0.5	0.92	0.27	0.5	0.86	0.20

Results of drag and lift coefficient at two Reynolds number of 3900 and 10000 for four different courant number is shown in Figure 4.37. The convergence of the solution is determined by using different courant numbers in range of 0.5 to 32 for coeffienct of drag and lift. It is evident from the results that the value of these two coefficients changes very slightly when C ≤ 2. Simulations are done with specific size of time step to keep the value of courant number less than 1.

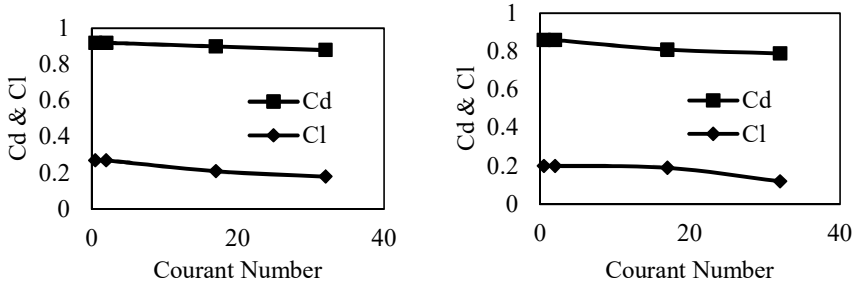

Figure 4.37: Drag and lift coefficients for different courant numbers at (a) Re= 3900 (b) Re=10000 using RKE model.

4.3.3 **Coefficient of drag and lift under turbulence flow**

ANSYS Fluent offers various turbulence models but k-ε (K-E) and k-ω (K-W) are the two most widely used turbulence models for Reynold's Average Navier-Stokes (RANS) equations. Each K-epsilon and K-omega method provides alternative options of stnadrad (SK) and realizable (RK) models. It is recommended by the ANSYS Fluent that SKE and RKE model should be used for flow problems for Re between 3900 and 10000. The calculated drag coefficients (*Cd*) based on SKE and RKE models are compared with available experimental data in Table 4.3.

Table 4.4: Comparison of simulations results for the drag coefficient with available data of experimental study for Re = 3900 & 10000

	Re = 3900	*Re*=10000
	Cd	**Cd**
SKE	0.8	0.7
RKE	0.98	0.92
Experiment (Lourenço, 1993)	0.98	1.01

The comparison of drag coefficients of SKE and RKE at two different Reynolds number is shown in Figure 4.38. The obtained simulation data are compared with the experimental study done by Lourenço (1993). The same value of drag coefficient was also reported by Stephen et al. 2011 in his study of turbulent flow at Reynold number 3900. Drag coefficient results obtained using SKE and RKE model show good agreement with available experimental data having a difference of less than 10%.

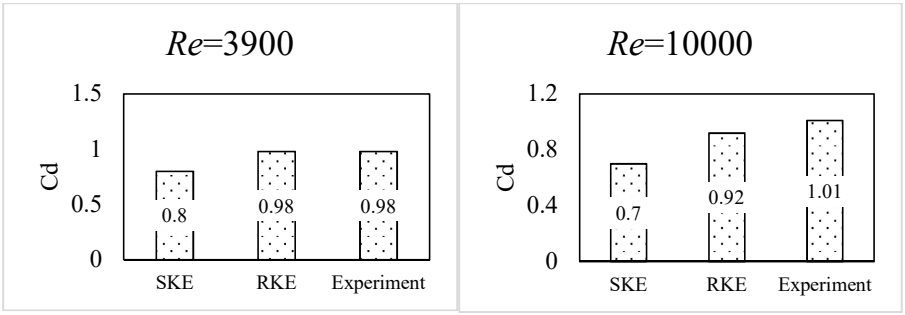

Figure 4.38: Comparison of Drag coefficient obtained by two different turbulence models with experiment for Re = 3900 & 10000

The values of lift coefficients are also calculated using SKE and RKE models for two different Reynolds number of 3900 and 10000. The calculated lift coefficients (*Cl*) based on SKE and RKE models are compared with available experimental data in Table 4.4.

Table 4.5: Comparison of simulations results for lift coefficient with available data of experimental study for Re = 3900 & 10000

	Re = 3900	*Re*=10000
	Cl	**Cl**
SKE	0.05	0.19
RKE	0.4	0.49
Experiment (chen 1971)	0.44	0.58

The comparison of lift coefficients of SKE and RKE at two different Reynolds number is shown in Figure 4.39. The obtained simulation data are compared with the experimental study done by Chen and Ballengee (1971). A similar value of drag coefficient was also reported by Bishop and Hassan in their experimental work conducted in 1964 (Bishop and Hassan, 1964). Comparison of Lift coefficient values obtained using the RKE model also

show good agreement with available experimental data having a difference of less than 10%.

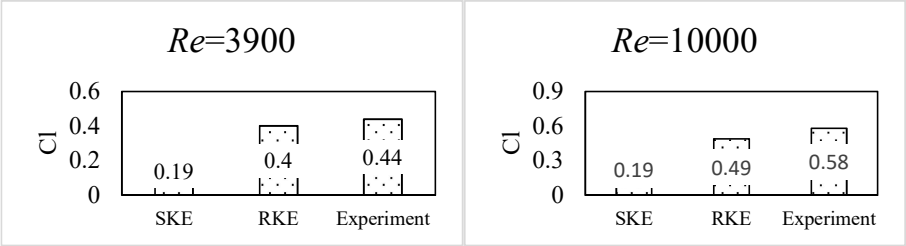

Figure 4.39: Comparison of Lift coefficient obtained by two different turbulence models with experiment for Re = 3900 & 10000

The drag and lift coefficient values of the RKE turbulence model are closer to the values of experiments as compared to the SKE model. The vortex (vorticity) of the turbulence model using RKE is shown in Figure 4.40 at two different Reynolds number. The vertex pattern is in 2S form and resembles the vertex pattern of Wornom et al. (2011) conducted using LES, a computationally intensive method.

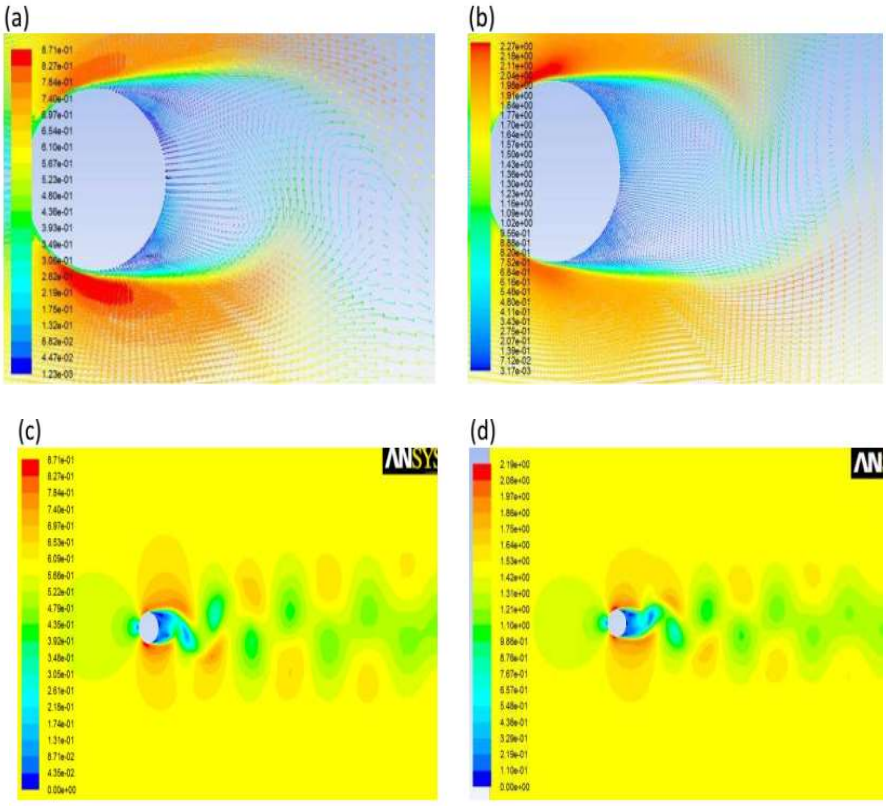

Figure 4.40: Downstream vortex shedding of the smooth circular structure using RKE turbulence model (a) velocity vector at Re=3900, (b) velocity vector at Re=10000, (c) velocity contour at Re=3900, (d) velocity contour at Re=10000

4.3.4 **Pressure distribution**

The distribution of pressure around the circular structure in the numerical tank for two different Reynolds number is calculated using the RKE turbulence model. Values of pressure coefficient with respect to the angle around the circular structure are given in Figure 4.41 for Reynolds number 3900.

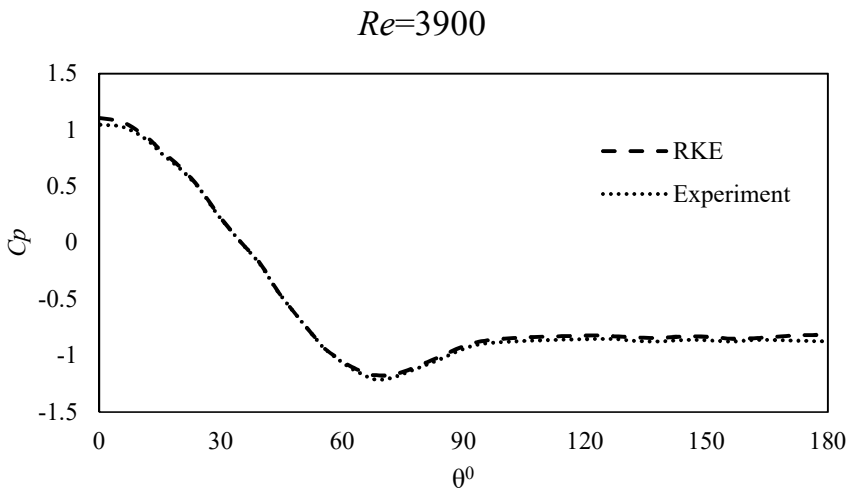

Figure 4.41: Comparison of pressure coefficient around a circular cylinder with experiment for RKE turbulence model at Re = 3900

The pressure distributions near the cylindrical structure for Reynolds number of 10000 have also been calculated using the RKE turbulence model as shown in Figure 4.42.

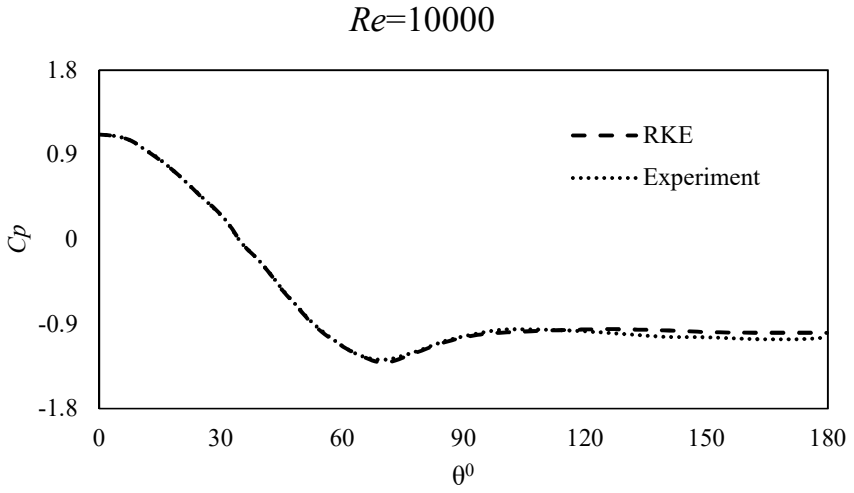

Figure 4.42: Comparison of pressure coefficient around a circular cylinder with experiment for RKE turbulence model at Re = 10000

When simulation results compared with the experimental work of Norberg (2002), resutls matches very well for the above mentioned Reynolds

number and determination of pressure coefficient at stagnation point is very well. Similar results of the RKE turbulence model at Re=10000 were also reported by Wornom et al. (2011) in his LES turbulence model at Re=8000.

4.4 Flow in a Tank with Deck Structure

The grid dependency test result for the FSI Tank with four different mesh resolutions is given in Figure 4.43. Lift forces generated by each mesh with respect to time is compared with the result of other meshes. The size of the mesh grid for all four meshes is approximately the same as used in the other numerical tanks.

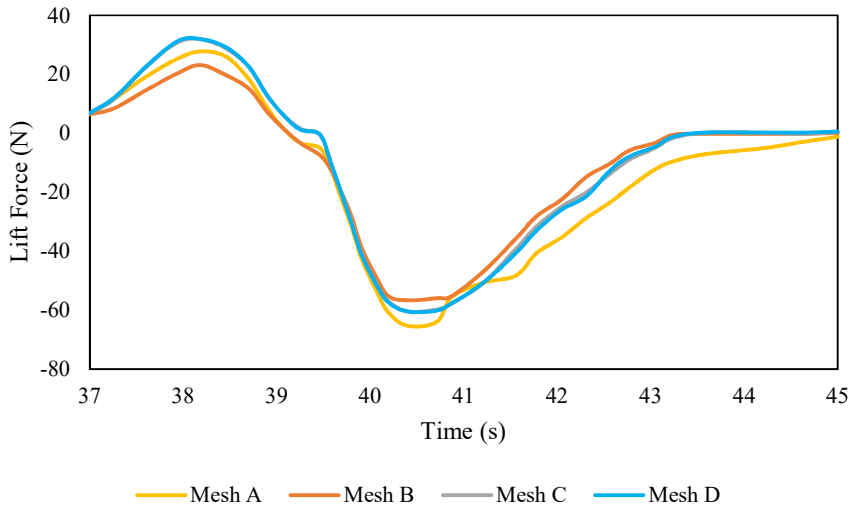

Figure 4.43: The Grid dependency test result for the FSI Tank with four different mesh resolutions.

It is evident from the meshing results that Mesh C shows no or little deviation as compared to other meshes and it is quicker to generate so it is chosen for all the simulations.

To determine the wave-in-deck loads on the lower part of an offshore structure by waves, a two-dimensional FSI tank is constructed as shown in Figure 4.44. The wave parameters for the FSI tank are given in Table 1. Stokes fifth-order waves are generated in the tank to apply deep/intermediate water conditions.

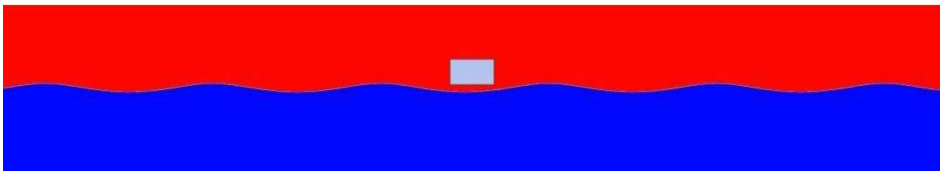

Figure 4.44: Offshore wave environments generation in FSI tank using stokes waves.

Four different wave plots from (Rolf Jarle, 2001) experiment hitting the deck are presented in Figure 4.45. The first sketch of the experimental result Figure 4.45 (a) shows an undisturbed wave hitting the platform deck. The second sketch of Figure 4.45 (b) shows an increase in the wetted area when water starts to rise and pile up below the deck. This water piles up causes the jet formation and water starts moving downstream leaving a gap upstream as shown in Sketch (c) of Figure 4.45. Water leaves the deck completely except a tangential touch at the centre of the deck is visible in the sketch (d) of Figure 4.45. (Rolf Jarle, 2001) observed that water exit has a longer duration as compared to the water entry phase which is also confirmed from the CFD simulations. This longer duration is due to the surface tension of water particles that stick with the deck surface when water meets it.

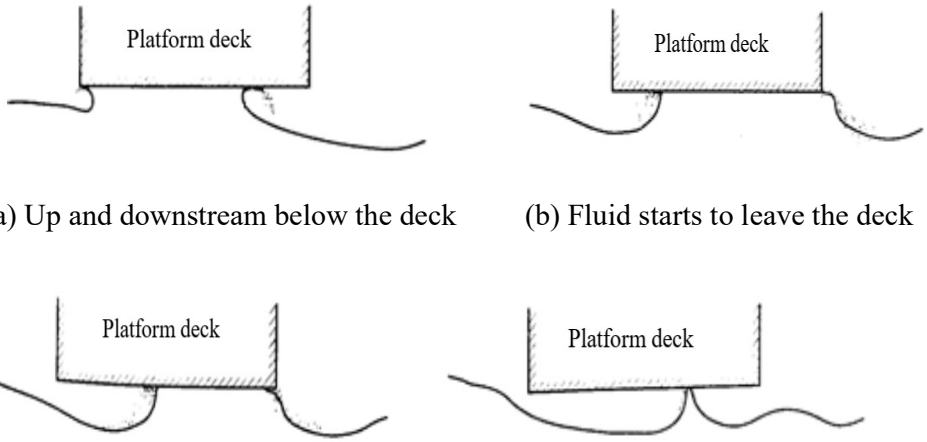

(a) Up and downstream below the deck (b) Fluid starts to leave the deck

(c) Downstream start to move again (d) Water leaving the structure

Figure 4.45: Four different sketches of the wave profiles below the deck of offshore structure at different time instants observed by (Rolf Jarle, 2001).

The volume of fluid (VOF) distribution of current simulations at four different time instants is shown in Figure 4.46. In the first time instant as shown in Figure 4.46 (a), a maximum peak force of 38 N is observed where the slamming pressure is also observed at its peak when a regular wave hits the deck. The slamming forces observed during this time instant contribute local loads due to small, wetted area. During the next two-time instants which start around 43 seconds as shown in Figure 4.46 (b & c), the lifting forces change their sign from positive to negative. This negative force is due to the negative added mass. The only force which acts on the platform is the incident wave force because the slamming forces cease to exist. The magnitude of the lifting force is negative in the second time instant, and it is around -23 N. The third time instant also shows similar properties as the second time instant due to the negative force peak and largest wetted area. Large negative velocities are observed around the upstream corner of the deck which contribute a peak of negative added mass. The observed negative force peak at time 44.44 s is -

78 N. (Rolf Jarle, 2001) also confirmed that peak negative force is observed when the wetted area below the deck is maximum. The fourth time instant as shown in Figure 46 (d) represents the time when the impact load is heading towards zero because the incident wave is leaving the deck. A wave leaving the deck contributes no lifting forces during this time instant and observed lifting force at a time around 48.5 s is -0.5 N. It is also evident from the VOF plot that during this time, the downstream water body has started to move upward, and water is released below the deck.

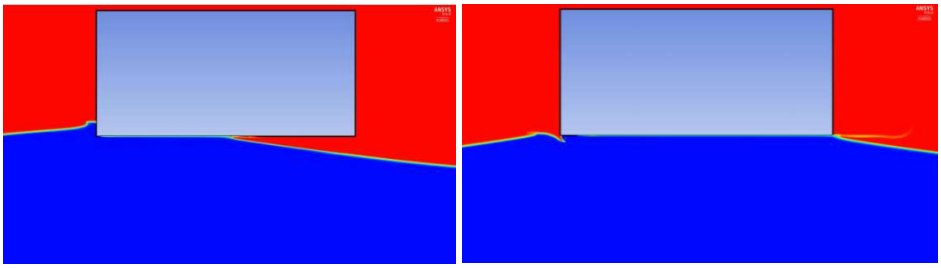

(a) VOF plot at 42.30 second (b) VOF plot at 43.61 second

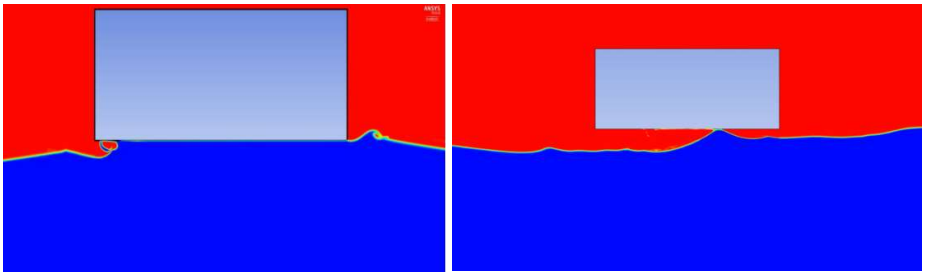

(c) VOF plot at 44.44 second (d) VOF plot at 48.5 second

Figure 4.46: Four different sketches of the volume of fluid (VOF) profiles for waves below the deck of offshore structure at different time instants observed in current CFD simulations.

The velocity plot of the CFD simulation for time 42.30 second is given in Figure 4.47. The vector shows the direction of the flow while colour indicates the magnitude of velocity. During the water entry phase before water

hitting the deck, the velocity plot shows the maximum upward velocity. When water touches the deck of the platform, velocity near the upstream edge of the deck becomes negative and changes direction. For a time of 43.61 seconds, water reaches the downstream corner of the deck and the velocity vector below the deck are parallel to it. A velocity of 0.89 ms^{-1} is observed near upstream and downstream corners of the deck. A constant velocity of 0.3 ms^{-1} is experienced in the tank which increases near the free surface when water moves near the edges.

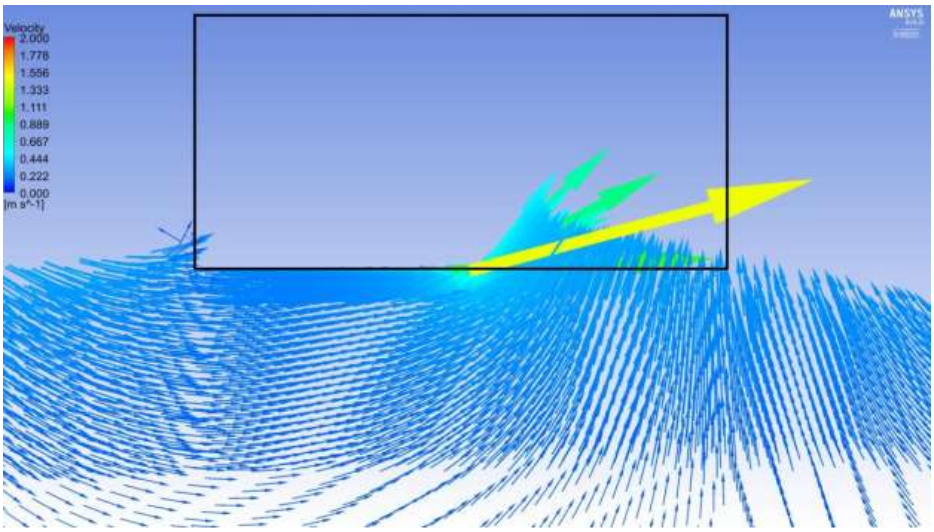

Figure 4.47: The velocity profile in the FSI tank for a flow time of 42.30 s.

Lifting forces generated from wave-in-deck loads of current simulations are compared with the experimental results of (Rolf Jarle, 2001) as given in Figure 4.48. The yellow line indicates the result of the current CFD simulations while the dotted black line is the experimental result performed by (Rolf Jarle, 2001). The CFD results match very well with the experiment during the water entry phase. It deviates a little bit during the water exit phase. This deviation could be due to the influence of turbulence caused by the deck

when water collide with it and no turbulence model was used in this study to account for this effect. It is further revealed from the results that a positive lifting force is captured during the water entry phase which become negative during the exit phase of the water. This negative force can be attributed to the negative added mass. The first event of result deviation occurs during 39 seconds of flow time when the lifting force becomes zero. The impact duration is smaller as compared to other simulation time because the lifting force approaches zero at a faster rate which causes a small force to jump near the horizontal axis. An error of less than 3% is observed during the maximum lifting force while an error of 15% is observed during the minimum lifting force during this comparison.

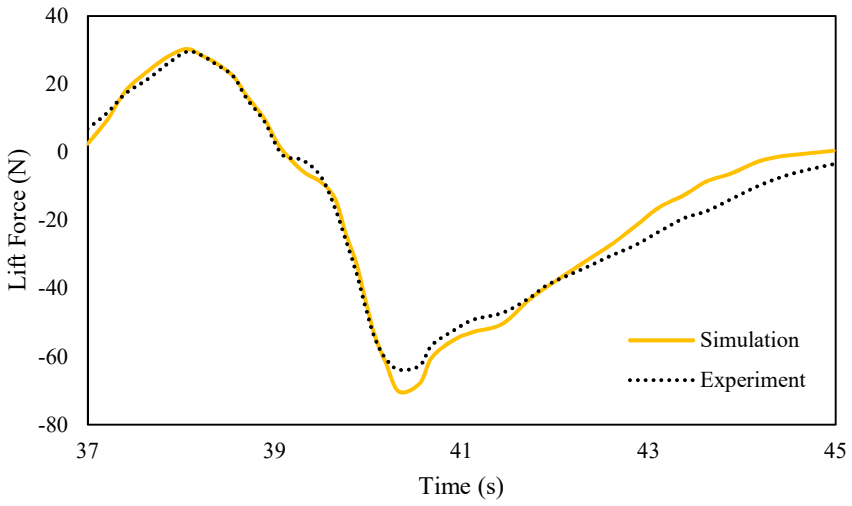

Figure 4.48: Comparison of Lift forces generated in the FSI tank with the experimental results of (Rolf Jarle, 2001)**.**

4.5 Summary

A numerical model with four distinct layouts was created using ANSYS Fluent to explore the behaviour of metocean parameters near the free surface of an offshore structure. The research began with the creation of metocean ecosystems in a numerical tank to simulate their interaction with the structure. The numerical analysis findings were compared to the analytical and experimental solutions as a reference. A grid dependence test was performed to establish the best appropriate mesh size for the simulations before completing the comparison analysis of simulations with analytical or experimental solutions.

The purpose of the first numerical model was to verify the tank by analyzing the wave profiles obtained near the free surface and comparing them with the ideal wave profiles obtained using Stokes ~~stokes~~ second-order wave. The grid convergence test for the first model showed the damping effect of the numerical waves in the tank. This damping effect was observed after gauge 5 located at 10 meters from the inlet of the validation tank. This damping effect was avoided by increasing the length of the tank. Simulated wave profiles from the verification tank when compared with the ideal wave profiles gave satisfactory results.

By comparing the free surface profiles of the waves generated in the tank with the reference experimental results of the Dingemans (1994), the second numerical model was utilised to validate the CFD results of the met ocean environment. For the first three gauges, the meshing results of this

model showed no difference in readings. After gauge 4, the difference was obvious. Mesh C, which had meshing elements around 400000 and was faster to generate, showed little or no variation and was chosen for the comparison analysis. When the CFD findings were compared to the experimental results, the first four gauges positioned before the submerged bar in the tank showed negligible variance. For the number gauges positioned after the submerged bar, more differences in the result begin to occur (7 to onwards). ~~The dispersive effect of the submerged bar is responsible for this difference in the outcome.~~ The reading of wave gauge 7 has a time delay of 0.1 second, indicating the numerical model's limits. Overall, the CFD results match the experimental data of the water waves' free surface elevation quite well.

In a third numerical tank, flow around a circular structure is investigated for two distinct Reynolds numbers (Re). For two different Reynold numbers (Re) of 3900 and 10000 with structured mesh, four different meshes with a number of elements ranging from 20000 to 560000 are examined. The coefficient of drag (Cd), coefficient of lift (Cl), and coefficient of pressure (Cp) are calculated for various grid sizes. Mesh B is used to check the pressure distribution around circular cylinder. ~~After mesh B, the pressure distribution around the circular cylinder meshing results~~. Mesh C is utilised to perform future calculations since it is simple to create and process. For flow issues with Re between 3900 and 10000, the ANSYS Fluent recommends using the SKE and RKE models. The results of the SKE and RKE models for drag and lift coefficients are in good agreement with known experimental data, with a discrepancy of less than 10%. The RKE turbulence model is used to

calculate the pressure distribution around the circular structure in the numerical tank for two distinct Reynolds numbers. When the simulation findings are compared to experimental work, the overall agreement at these two Re numbers is good, and the prediction of Cp at the stagnation point is good.

In the last numerical tank, a rectangular block was introduced to determine wave in deck forces near the free surface of an offshore structure. A meshing test was carried out prior to comparing CFD results with reference experimental data by comparing lift forces at four different grid resolutions. The C mesh findings were judged to be the most reliable, thus they were used for comparative analysis. To simulate deep/intermediate water conditions, Stokes second order waves were generated in the tank. Waves hitting the deck in a CFD simulation looked similar to experimental sketches. When a typical wave hits the deck, a maximum peak force of 38 N is detected, and the slamming pressure is also observed at its highest. In the second time instant, the magnitude of the lifting force was negative, around -23 N. At the third time instant, the observed negative force peak was -78 N. The lifting forces at the fourth time instant are -0.5 N.

CHAPTER 5

CONCLUSION AND RECOMMENDATIONS

Three objectives were set to investigate the behaviour of the metocean interaction model near the free surface with offshore structure. The first objectives of the research was to generate regular waves by verifying and validating the numerical model results against the analytical and experimental results. The second objective of the study was to determine the lift and drag coefficients around a circular cylinder for fluid structure interaction. The third objective of the study was to determine the wave in deck forces near the free surface of an offshore structure. The first two objective of the study is achieved by constructing a flat bottom and submerged bar bottom numerical wave tank where the result of the simulation of the first wave tank are compared with the theory and later with experiment. The second objective is achieved by simulating flow around a circular cylinder under two different Reynolds number. The obtained results for lift, drag and pressure coefficients are compared with the reference experimental work available in the literature. The last objective of the study is achieved by constructing a fixed rectangular deck in the numerical wave tank where the vertical forces obtained from simulations are compared with the experiment.

5.1 Conclusion

The first objective of the study is to validate and verify the numerical wave tank for free surface flow modelling where CFD output are compared with the analytical and experimental results. The verification is done by comparing the simulation results with the experimental work of Dingemans (1994). The waves are generated in the curved bottom wave tank which is similar to the experimental wave tank. The most suitable mesh size is determined by conducting a grid convergence test. Mesh of four different grid size (A to D) is generated. The free surface elevation results generated by all the four meshes with case A wave parameters as given in Table 3.2 are compared with each other at 11 different positions on the horizontal axis in the wave tank. Mesh C is chosen for the comparison of simulation results with the experiment. The experiment by Dingemans (1994) uses three different waves labelled as Case A, Case B and Case C in his experimental study with wave characteristics as given in Table 3.2. In this thesis, the simulation results generated using Case A wave characteristics are compared with the experiment. The free surface elevations of the waves are measured at 11 waves gauges. The first three wave gauges produced identical surface elevation when compared with the experiment which is located before the submerged bar. Wave profile is regular in nature in front of the curved bar. The wave profiles start changing the surface elevation from gauge four onwards due to the construction of irregular wave profile because high harmonics cannot remain in phase to the first wave. This change in surface elevation is due to the disturbance of fluid molecules by the submerged bar. More significant variations are observed from gauge 7 to gauge 9 which are located downstream the upper surface of

the submerged bar where a delay of 0.1 seconds is observed. This time delay may be caused by the speed of the emerging wave. Even the simulation results display a fluctuation in time but the amplitude of the simulated wave nearly matches with the experimental wave amplitude. A similar time delay is also observed for gauges 10 and 11. The grid convergence test also did not indicate any improvement of simulation results with the improvement of the mesh size. The simulation used a laminar flow where turbulence model is avoided. It might be possible that the lack of a turbulence model has contributed to the inconsistency of simulation results with the experimental results.

The second objective is to determine the lift and drag coefficients around a circular cylinder for fluid-structure interaction. This objective is achieved by constructing a numerical tank with a fixed circular cylindrical structure and comparing the simulation results with reference experimental work. A mesh sensitivity study is carried out before performing the targeted simulations for comparison. The convergence is checked through changes of mean drag coefficient Cd and lift coefficient Cl for different mesh sizes. The pressure distribution around the structure indicated that very little or no change in the pressure distribution is observed from mesh B onwards so mesh C is used for all the simulations. Two turbulence model are used for two reference values Reynolds number (Re) 3900 and 10000. The RKE turbulence model generated more accurate results of lift and drag coefficient when compared with the experiment. It showed a good agreement with the available experimental data having a difference of less than 10%.

The third objective of the study is to determine wave forces on the deck of an offshore structure. The simulation is used to determine the vertical forces created by water waves during the wave-structure interaction. The simulated results are then compared with the experimental results of Rolf Jarle (2001). A water entry and exit phase of simulation is studied and compared with the experimental work. During the water entering phase, a positive lifting force is felt, where as a negative force is exerted by water when it leaves the deck. The additional positive and negative fluid particle accelerations create these positive and negative forces. The negative lifting force is larger in magnitude than the positive lifting force. The highest positive slamming force was measured at 38 N, whereas the negative peak force was measured at -78 N. Due to the surface tension of the water particle that stays to the deck surface, the outflow process lasts more than the water inflow process. During the water exit phase, the most deck wetted area is observed with the lowest force peak, whereas the least wetted area is observed during the water entry phase with the highest force peak. Local structural reactions are influenced by water entrance, while global structural responses are influenced by water outflow.

During this comparison, an inaccuracy of less than 3% was observed during the maximum lifting force, whereas an error of 15% was observed during the minimum lifting force. The turbulence effect generated in the fluid following a collision with the deck causes this bigger inaccuracy during the water escape phase. To account for the turbulence effect of the fluid flow during fluid-structure interaction, a turbulence model should be used. The grid

dependency results show that mesh has an impact on the outcomes, hence mesh with the right grid size should be employed in the CFD study.

5.2 Recommendations

Some recommendations for the flow analysis of offshore structures near the free surface using computational fluid dynamics are given as follows:

i. Dimensions of the numerical model do not influence the simulation results, so it is recommended to use dimensions of smaller magnitudes to run the simulations smoothly and save computational power.

ii. Unstructured mesh generates a large number of control volumes, so it is recommended to use structured mesh for accurate results.

iii. Wave spectrum should be preferred instead of wave theory because it represents most actual offshore situations if required data is available.

iv. It is suggested to perform some tests simulations for the generation of offshore environments in the numerical wave tank before performing actual simulations.

REFERENCES

Abbasnia, A., Ghiasi, M., 2014. Simulation of irregular waves over submerged obstacle on a NURBS potential numerical wave tank. Latin American Journal of Solids and Structures 11, 2308–2332. https://doi.org/10.1590/S1679-78252014001300001

AbdelRaheem S.E., 2016. Nonlinear behaviour of steel fixed offshore platform under environmental loads. Ships and Offshore Structures 11, 1–15. https://doi.org/10.1080/17445302.2014.954301

Abrahamsen P.M., Ong, M.C., Pettersen, B., Myrhaug, D., 2014. Large Eddy Simulations of flow around a smooth circular cylinder in a uniform current in the subcritical flow regime. Ocean Engineering 77, 61–73. https://doi.org/10.1016/j.oceaneng.2013.10.018

Anderson, D.A., Tannehill, J.C., Pletcher, R.H., Ramakanth, M., Shankar, V., 2020. Computational Fluid Mechanics and Heat Transfer, 4th ed. CRC Press, Fourth edition. Boca Raton, FL : CRC Press, 2020. Series: Computational and physical processes in mechanics and thermal sciences. https://doi.org/10.1201/9781351124027

Balendra, T., Li, Z., 2008. Seismic hazard of Singapore and Malaysia. Electronic Journal of Structural Engineering 8, 57–63.

Beji, S., Battjes, J.A., 1993. Experimental investigation of wave propagation over a bar. Coastal Engineering 19, 151–162. https://doi.org/10.1016/0378-3839(93)90022-Z

Bishop, R.E.D., Hassan, A.Y., 1964. The lift and drag forces on a circular cylinder oscillating in a flowing fluid. Proceedings of the Royal Society

of London. Series A. Mathematical and Physical Sciences 277, 51–75. https://doi.org/10.1098/rspa.1964.0005

Boiko, A. V., Kirilovskiy, S. V., Maslov, A.A., Poplavskaya, T. V., 2015. Engineering modeling of the laminar–turbulent transition: Achievements and problems (Review). Journal of Applied Mechanics and Technical Physics 56, 761–776. https://doi.org/10.1134/S002189441505003X

Canonsburg, A.D., 2017. ANSYS Fluent Tutorial Guide.

Canonsburg, T.D., 2017. ANSYS Fluent User's Guide.

Castellini, M., Barbanera, M., Scungio, M., Arpino, F., 2020. Numerical and experimental analysis of turbulent fluid flow around latest generation cycling frame. International Journal of Computational Methods and Experimental Measurements 8, 355–366. https://doi.org/10.2495/CMEM-V8-N4-355-366

Catalano, P., Wang, M., Iaccarino, G., Moin, P., 2003. Numerical simulation of the flow around a circular cylinder at high Reynolds numbers. International Journal of Heat and Fluid Flow 24, 463–469. https://doi.org/10.1016/S0142-727X(03)00061-4

Chen, C.F., Ballengee, D.B., 1971. Vortex shedding from circular cylinders in an oscillating freestream. AIAA Journal 9, 340–342. https://doi.org/10.2514/3.6179

Cui, F., Daskiran, C., King, T., Robinson, B., Lee, K., Katz, J., Boufadel, M.C., 2020. Modeling oil dispersion under breaking waves. Part I: Wave hydrodynamics. Environmental Fluid Mechanics 20, 1527–1551. https://doi.org/10.1007/s10652-020-09753-7

Cummings, R.M., Mason, W.H., Morton, S.A., McDaniel, D.R., 2015. Applied Computational Aerodynamics, Applied Computational Aerodynamics. Cambridge University Press. https://doi.org/10.1017/cbo9781107284166

de Ridder, M.P., Smit, P.B., van Dongeren, A.R., McCall, R.T., Nederhoff, K., Reniers, A.J.H.M., 2021. Efficient two-layer non-hydrostatic wave model with accurate dispersive behaviour. Coastal Engineering 164, 103808. https://doi.org/10.1016/j.coastaleng.2020.103808

Dean, R.G., Dalrymple, R.A., 1991. Water Wave Mechanics for Engineers and Scientists, Advanced Series on Ocean Engineering. World Scientific. https://doi.org/10.1142/1232

Dingemans, M.W., 1994. MAST PROJECT 1: WAVES G8-M Comparison of computations with Boussinesq-like models and laboratory measurements, memo in framework of MAST project (G8-M), Delft Hydraulics memo H1684.12. Deltares (WL).

Dong, S., Karniadakis, G.E., 2005. DNS of flow past a stationary and oscillating cylinder at Re = 10000. Journal of Fluids and Structures 20, 519–531. https://doi.org/10.1016/j.jfluidstructs.2005.02.004

Elhanafi, A., Fleming, A., Leong, Z., Macfarlane, G., 2017. Effect of RANS-based turbulence models on nonlinear wave generation in a two-phase numerical wave tank. Progress in Computational Fluid Dynamics 17, 141–158. https://doi.org/10.1504/PCFD.2017.084350

Feng, X., Wu, W., 2019. Generation of Water Waves Using Momentum Source Wave-Maker Applied to a RANS Solver. Mathematical Problems in Engineering 2019. https://doi.org/10.1155/2019/1308960

Gholamipoor, M., Ghiasi, M., 2021. Simulation of fully nonlinear water wave propagation over the flat bottom and uneven bottom by meshless numerical wave tank. Archive of Applied Mechanics 2021 1–13. https://doi.org/10.1007/S00419-021-02010-3

Ji, Q., Dong, S., Luo, X., Guedes Soares, C., 2017. Wave transformation over submerged breakwaters by the constrained interpolation profile method. Ocean Engineering 136, 294–303. https://doi.org/10.1016/J.OCEANENG.2017.03.037

Kamath, A., Chella, M.A., Bihs, H., Arntsen, Ø.A., 2017. Energy transfer due to shoaling and decomposition of breaking and non-breaking waves over a submerged bar. https://doi.org/10.1080/19942060.2017.1310671

Kang, A., Lin, P., Lee, Y.J., Zhu, B., 2015. Numerical simulation of wave interaction with vertical circular cylinders of different submergences using immersed boundary method. Computers and Fluids 106, 41–53. https://doi.org/10.1016/j.compfluid.2014.09.043

Karimirad, M., Michailides, C., Nematbakhsh, A., 2018. Offshore Mechanics, Offshore Mechanics. John Wiley & Sons, Ltd. https://doi.org/10.1002/9781119216674

Kim, J., Pedersen, G.K., Løvholt, F., LeVeque, R.J., 2017. A Boussinesq type extension of the GeoClaw model - a study of wave breaking phenomena applying dispersive long wave models. Coastal Engineering 122, 75–86. https://doi.org/10.1016/j.coastaleng.2017.01.005

Kim, S.Y., Kim, K.M., Park, J.C., Jeon, G.M., Chun, H.H., 2016. Numerical simulation of wave and current interaction with a fixed offshore

substructure. International Journal of Naval Architecture and Ocean Engineering 8, 188–197. https://doi.org/10.1016/j.ijnaoe.2016.02.002

Kulyakhtin, A., Shipilova, O., Muskulus, M., 2014. Numerical simulation of droplet impingement and flow around a cylinder using RANS and LES models. Journal of Fluids and Structures 48, 280–294. https://doi.org/10.1016/j.jfluidstructs.2014.03.007

Kyte, A., 2014. Practical use of computational fluid dynamics (CFD) in improving the efficiency of domestic ventilation waste heat recovery systems. International Journal of Energy and Environmental Engineering 2014 5:2 5, 1–7. https://doi.org/10.1007/S40095-014-0090-8

Lambert, R.J., 2012. Development of a Numerical Wave Tank using OpenFOAM. University of Coimbra.

Lintermann, A., 2021. Computational Meshing for CFD Simulations p.p 85–115. https://doi.org/10.1007/978-981-15-6716-2_6

Liu, Z., Fang, K., 2019. Numerical verification of a two-layer Boussinesq-type model for surface gravity wave evolution. Wave Motion 85, 98–113. https://doi.org/10.1016/j.wavemoti.2018.11.007

Lourenço, L., 1993. Characteristics of the Plane Turbulent Near Wake of a Circular Cylinder.

Mader, C.A., Kenway, G.K.W., Yildirim, A., Martins, J.R.R.A., 2020. ADflow: An Open-Source Computational Fluid Dynamics Solver for Aerodynamic and Multidisciplinary Optimization. https://doi.org/10.2514/1.I010796

Marques F.M., Lopes, A.M., Ferreira, A.D., 2018. Numerical simulation of regular waves: Optimization of a numerical wave tank. Ocean Engineering 170, 89–99. https://doi.org/10.1016/j.oceaneng.2018.10.002

Sundararaj, M.T 2021. CFD Analysis of Golf Ball with Various Turbulence Models. Turkish Journal of Computer and Mathematics Education (TURCOMAT) 12, 491–497. https://doi.org/10.17762/TURCOMAT.V12I1S.1912

Nagata, T., Noguchi, A., Kusama, K., Nonomura, T., Komuro, A., Ando, A., Asai, K., 2020. Experimental investigation on compressible flow over a circular cylinder at Reynolds number of between 1000 and 5000. Journal of Fluid Mechanics 893. https://doi.org/10.1017/JFM.2020.221

Norberg, C., 2002. Pressure distributions around a circular cylinder in cross-flow. Symposium on Bluff-Body Wakes and Vortex-Induced Vibrations (BBVIV3) 1–4.

Ohyama, T., Kioka, W., Tada, A., 1995. Applicability of numerical models to nonlinear dispersive waves. Coastal Engineering 24, 297–313. https://doi.org/10.1016/0378-3839(94)00033-T

Olabarrieta, M., Medina, R., Castanedo, S., 2010. Effects of wave-current interaction on the current profile. Coastal Engineering 57, 643–655. https://doi.org/10.1016/j.coastaleng.2010.02.003

Ong, M.C., 2017. CFD applications in offshore engineering. EPJ Web of Conferences 143. https://doi.org/10.1051/EPJCONF/201714301002

Prasad, D.D., Ahmed, M.R., Lee, Y.H., Sharma, R.N., 2017. Validation of a piston type wave-maker using Numerical Wave Tank. Ocean Engineering 131, 57–67. https://doi.org/10.1016/j.oceaneng.2016.12.031

Rodríguez, I., Lehmkuhl, O., Chiva, J., Borrell, R., Oliva, A., 2015. On the flow past a circular cylinder from critical to super-critical Reynolds numbers: Wake topology and vortex shedding. International Journal of Heat and Fluid Flow 55, 91–103. https://doi.org/10.1016/j.ijheatfluidflow.2015.05.009

Rolf J.B., 2001. Theoretical and Experimental Studies of Wave Impact underneath Decks of Offshore Platforms (Thesis/Dissertation) | ETDEWEB [WWW Document]. Thesis/Dissertation. URL https://www.osti.gov/etdeweb/biblio/20196962 (accessed 4.20.21).

Schloen, J., Stanev, E., Grashorn, S., 2017. Wave-current interactions in the southern North Sea: The impact on salinity. Ocean Modelling 111, 19–37. https://doi.org/10.1016/j.ocemod.2017.01.003

Sharma, A., Ananthan, S., Sitaraman, J., Thomas, S., Sprague, M.A., 2021. Overset meshes for incompressible flows: On preserving accuracy of underlying discretizations. Journal of Computational Physics 428, 109987. https://doi.org/10.1016/J.JCP.2020.109987

Silva, M.C., Vitola, M.A., Esperança, P.T.T., Sphaier, S.H., Levi, C.A., 2016. Numerical simulations of wave–current flow in an ocean basin. Applied Ocean Research 61, 32–41. https://doi.org/10.1016/j.apor.2016.10.005

Silva, W.A., 2018. AEROM: NASA's Unsteady Aerodynamic and Aeroelastic Reduced-Order Modeling Software. Aerospace. Vol. 5, Page 41 5, 41. https://doi.org/10.3390/AEROSPACE5020041

Singh, S.K., Debnath, K., 2016. Combined effects of wave and current in free surface turbulent flow. Ocean Engineering 127, 170–189. https://doi.org/10.1016/j.oceaneng.2016.10.014

Song, H., Robertson, A., Jonkman, J., Sewell, D., 2012. Incorporation of Multi-Member Substructure Capabilities in FAST for Analysis of Offshore Wind Turbines. Society of Petroleum Engineers (SPE). https://doi.org/10.4043/23675-ms

Stokes, G.G., 1880. Mathematical and Physical Papers. Volume I. Cambridge University Press, Cambridge.

Tatlock, B., Briganti, R., Musumeci, R.E., Brocchini, M., 2018. An assessment of the roller approach for wave breaking in a hybrid finite-volume finite-difference Boussinesq-type model for the surf-zone. Applied Ocean Research 73, 160–178. https://doi.org/10.1016/j.apor.2018.01.012

Tran, T.T., Kim, D.H., 2016. A CFD study into the influence of unsteady aerodynamic interference on wind turbine surge motion. Renewable Energy 90, 204–228. https://doi.org/10.1016/j.renene.2015.12.013

Tu, J., Yeoh, G., Liu, C., 2018. Computational fluid dynamics: a practical approach, 3rd ed. Elsevier India.

Tunlid, M., Olsson, A., 2015. CFD simulation of wave-in-deck loads on offshore structures.

Uddin, M.N., Atkinson, M., Opoku, F., 2020. A Computational Fluid Dynamics Investigation of a Numerically Simulated Wave Tank Evaluation of the Thrust of a Scramjet Engine as a Function of Freestream Mach Number. American Journal of Mechanical Engineering 8, 40–49. https://doi.org/10.12691/ajme-8-1-5

Vasarmidis, P., Stratigaki, V., Suzuki, T., Zijlema, M., Troch, P., 2021. On the accuracy of internal wave generation method in a non-hydrostatic wave

model to generate and absorb dispersive and directional waves. Ocean Engineering 219, 108303. https://doi.org/10.1016/j.oceaneng.2020.108303

Windt, C., Davidson, J., Schmitt, P., Ringwood, J. V., 2019. On the assessment of numericalwave makers in CFD simulations. Journal of Marine Science and Engineering 7. https://doi.org/10.3390/JMSE7020047

Wornom, S., Ouvrard, H., Salvetti, M.V., Koobus, B., Dervieux, A., 2011. Variational multiscale large-eddy simulations of the flow past a circular cylinder: Reynolds number effects. Computers and Fluids 47, 44–50. https://doi.org/10.1016/j.compfluid.2011.02.011

Yang, I.J., Lee, Y.G., Jeong, K.L., 2015. Numerical simulation of the free surface around a circular column in regular waves using modified marker-density method. International Journal of Naval Architecture and Ocean Engineering 7, 610–625. https://doi.org/10.1515/ijnaoe-2015-0043

Ye, H., Wan, D., 2017. Benchmark computations for flows around a stationary cylinder with high Reynolds numbers by RANS-overset grid approach. Applied Ocean Research 65, 315–326. https://doi.org/10.1016/J.APOR.2016.10.010

Young, I.R., 1999. Wind Generated Ocean Waves, Elsevier Ocean Engineering Series. Elsevier Ltd. https://doi.org/10.1016/S1571-9952(13)70001-1

Zhang, J.S., Zhang, Y., Jeng, D.S., Liu, P.L.F., Zhang, C., 2014. Numerical simulation of wave-current interaction using a RANS solver. Ocean

Engineering 75, 157–164. https://doi.org/10.1016/j.oceaneng.2013.10.014

Zhang, S. ju, Zhu, L. sheng, Zou, K., 2019. A Comparative Study of Numerical Models for Wave Propagation and Setup on Steep Coral Reefs. China Ocean Engineering 33, 424–435. https://doi.org/10.1007/s13344-019-0040-6

Zhang, X., Simons, R., Buldakov, E., 2016. A numerical study of wave-current interaction in the bottom boundary layer. Proceedings of the Coastal Engineering Conference. American Society of Civil Engineers (ASCE). https://doi.org/10.9753/icce.v35.waves.17

Zhang, Z., Ji, C., Xu, D., 2021. Temporal and spatial evolution of vortex shedding for flow around a cylinder close to a wall. Ocean Engineering 228, 108964. https://doi.org/10.1016/J.OCEANENG.2021.108964

APPENDIX

Appendix A URSELL PARAMETER CALCULATION FOR CASE A

H=0.02 m
L= 3.738 m
h= 0.4 m
The general condition for Ursell Parameter is given as follows.

$$\frac{L^2\ H}{h^3} < \frac{8\ \pi^3}{3}$$

Here all the parameters are known so by inserting their values in the above relation it can be determined whether Case A satisfy the ursel parameter or not.

$$\frac{(3.738)^2 * \ 0.02}{(0.4)^3} < \frac{8 * \ (3.14)^3}{3}$$

$$\frac{13.97 * \ 0.02}{0.064} < \frac{8 * \ 30.959}{3}$$

$$\frac{0.27945}{0.064} < \frac{247.672}{3}$$

$$4.3664 < \ 82.55$$

Hence it is verified that the wave parameters of Case A satisfy the ursel parameter so stokes second-order theory can be used for Case A

Appendix B URSELL PARAMETER CALCULATION FOR CASE B

H=0.029 m
L= 4.791 m
h= 0.4 m
The general condition for Ursell Parameter is given as follows.

$$\frac{L^2\, H}{h^3} < \frac{8\,\pi^3}{3}$$

Here all the parameters are known so by inserting their values in the above relation it can be determined whether Case B satisfy the ursel parameter or not.

$$\frac{(4.791)^2 * \ 0.029}{(0.4)^3} < \frac{8 * \ (3.14)^3}{3}$$

$$\frac{22.95 * \ 0.029}{0.064} < \frac{8 * \ 30.959}{3}$$

$$\frac{0.6656567}{0.064} < \frac{247.672}{3}$$

$$10.4 < \ 82.55$$

Hence it is verified that the wave parameters of Case B satisfy the ursel parameter so stokes second-order theory can be used for Case B.

Appendix C URSELL PARAMETER CALCULATION FOR CASE C

H=0.041 m
L= 1.488 m
h= 0.4 m
The general condition for Ursell Parameter is given as follows.

$$\frac{L^2\,H}{h^3} < \frac{8\,\pi^3}{3}$$

Here all the parameters are known so by inserting their values in the above relation it can be determined whether Case C satisfy the ursel parameter or not.

$$\frac{(1.488)^2 * \ 0.041}{(0.4)^3} < \frac{8 * \ (3.14)^3}{3}$$

$$\frac{2.214 * \ 0.041}{0.064} < \frac{8 * \ 30.959}{3}$$

$$\frac{0.09}{0.064} < \frac{247.672}{3}$$

$$1.41 < \ 82.55$$

Hence it is verified that the wave parameters of Case C satisfy the ursel parameter so stokes second-order theory can be used for Case C.

Appendix D REYNOLDS NUMBER CALCULATION (RE=3900)

$$Re = \frac{V * D * \rho}{\mu}$$

From Table 3.9,
V=0.003908 m/s
D= 1 m
ρ = 998 kg/m^3
μ= 0.001 kg/ms

$$Re = \frac{0.003908 * 1 * 998}{0.001}$$

$$Re = \frac{3.900184}{0.001}$$

$$Re = 3900$$

Appendix E REYNOLDS NUMBER CALCULATION (RE=10000)

$$Re = \frac{V * D * \rho}{\mu}$$

From Table 3.9,
V=0.01 m/s
D= 1 m
ρ = 998 kg/m^3
μ= 0.001 kg/ms

$$Re = \frac{0.01 * 1 * 998}{0.001}$$

$$Re = \frac{9.98}{0.001}$$

$$Re = 10000$$